Studies on Optical Spectroscopy Techniques with Surface Plasmon Resonance

Hayato Ichihashi

Doshisha University

Graduate School of Science and Engineering

November 2019

Doshisha University
Graduate School of Science and Engineering

ABSTRACT

Studies on Optical Spectroscopy Techniques with Surface Plasmon Resonance

Hayato Ichihashi
SUPERVISOR: Professor Mami Matsukawa

Photoacoustic microscopy (PAM) has attracted increasing attention as a non-invasive 3D imaging technique in biomedicine and biomedical studies. A surface plasmon resonance (SPR) sensor is a good candidate for an ultrasonic sensor with high sensitivity and wide bandwidth used in high-resolution PAM. In designing the SPR sensor, it is important to understand the response of optical properties to the elastic and thermal effects in a metal film in Kretschmann configuration considering the surface medium and structure. Brillouin light scattering technique is well-known as an evaluation method of the thermal, elastic and optical properties for films, glasses and liquids. However, this technique cannot measure the dynamic pulse response which is necessary for the design of the SPR sensor used in PAM because this technique is an optical spectroscopy technique in the frequency domain. On the other hand, the sub-nanosecond pump probe technique is an effective method to evaluate the dynamic optical properties because this technique is an optical spectroscopy technique in the time domain. However, there are few studies on the pump probe technique in the sub-nanosecond region necessary for SPR ultrasonic sensor in a high-resolution PAM. In this thesis, the mechanism of this pump probe response based on reflectivity change under SPR condition was experimentally and theoretically investigated as a basic study. First, the pump probe system with a sub-nanosecond pulsed laser was developed to experimentally investigate the transient response in SPR condition. Next, the integrated theoretical model was constructed. Based on the comparisons between the experimental and the theoretical estimations, the change of reflectivity appeared to depend on the shift of the SPR angle and the broadening of the SPR curve. Moreover, it was estimated that the shift of the SPR angle was caused by the thermal expansion of the metal film due to thermoelastic stress and the broadening of the SPR curve was resulted from the increase of electron-phonon scattering rate due to temperature rise. A clear mechanism of the transient response of the sub-nanosecond pump probe under SPR was identified based on the experimental and theoretical approaches.

ACKNOWLEDGEMENTS

All studies I challenged were not able to be attained without many supports. I would like to express my greatest appreciations to the following people supporting my studies.

First, I am especially grateful for the extremely enormous support given by prof. Mami Matsukawa. She taught me not only many techniques of optical system but also basic procedures for my study. Her comments and suggestions supported my study a lot of times. Moreover, her comprehensive support helped my studies always. Also, I wish to express my sincere gratitude to prof. Yoshiaki Watanabe. He provided me with gentle encouragements which were valuable to me.

I would like to thank associate prof. Takahiko Yanagitani at Waseda university. He gave me basic knowledge about material technology focusing on piezoelectric materials. Moreover, he taught me the fun of study. I would like to thank also assistant prof. Shinji Takayanagi. He supported my studies with valuable advice and comments. He especially advised me to manufacture pure metal film samples necessary for surface plasmon resonance excitation.

I am grateful for valueless advices given by prof. Jun Kondoh at Shizuoka university. He advised me many techniques for surface plasmon resonance. Also, I am grateful for many advices given by prof. Hiroyuki Toda. He gave me important advices about optical system necessary for my many studies.

I would like to thank prof. Iwaki Akiyama for his insightful comments. He gave me the expanded perspective for study. Likewise, I would like to thank prof. Daisuke Koyama for his valuable comments regarding different studies.

I am grateful for the technical teaching about optical system given by Dr. Masahiko Kawabe. Moreover, he taught me how to pursue doctoral studies while being a full-time worker. I also wish to acknowledge Mr. Takeshi Sugimoto. He taught me the basic knowledge and techniques on Brillouin light scattering method.

I would like to acknowledge Mr. Hiromichi Hayashi, Mr. Takumi Fukunaga, and Mr. Shoya Ueno for their special assistances. They supported my study by their wide-ranging assistances through experiments. I would also like to acknowledge my colleagues from the Laboratory of Ultrasonic Electronics at Doshisha University, including Mr. Kosuke Imamura, Mr. Ryo Ikoma, Mr. Yoshiaki Kato, Mr. Masanari Yoshida, Mr. Ryosuke Hashimoto, Mr. Ryosuke Shimoya, Ms. Chao Enhui, Mr. Chihiro Takata, Mr. Mineki Oka, Ms. Shoko Hiyama, Mr. Shota Tomita, Mr. Yashuhiro Yokoi, Ms. Yuki Imoto, and Ms. Ayane Kihara.

I would like to thank my parents for their continuously warm encouragements during my research life. And finally, I would like to express gratitude to my wife Kumiko Ichihashi for her well-rounded support and considerable encouragement every day.

CONTENTS

CHAPTER 1.

CHAPTER 2.

CHAPTER 3.

CHAPTER 4.

CHAPTER 5.

TABLE OF SYMBOLS

t	Time
t_r	Transmittivity of electric field
t_0	Irradiation timing of the pump light
τ_0	Pulse duration
τ_s	Stress relaxation time
τ_the	Thermal relaxation time
ω	Angular frequency
ω_p	Plasma frequency
ω_p0	Plasma frequency at room temperature
z	Position of normal direction
x	Position of in-plane direction
L	Physical length
l	Mean free path
d	Film thickness
d_s	Tissue volume
D	Grain diameter
u	Displacement
λ	Wavelength
λ_F	De Broglie wavelength of electrons at the Fermi surface
θ_pm	Phase matching angle
θ_r	Resonance angle of surface plasmon resonance
θ	Incident angle
θ'	Refraction angle
ϕ	Phase
f_rp	Roughness profile
r_rms	Root-mean square roughness
r_spot	Spot diameter
r	Reflectivity of electric field
m^*	Effective electron mass

T	temperature increase
T_e	Electron temperature
T_l	Lattice temperature
T_{D}	Debye temperature
V_t	Input voltage with temporal dimension
V_ω	Input voltage with frequency dimension
V_0	Output voltage
V_{r}	Voltage of reference signal
G	Gain of the light detector
A	Conversion coefficient
P	Dielectric polarization
p	Fraction of elastically scattered electrons
χ	Non-linear optical coefficient
e	Elementary charge
N	Carrier density
S_{SPW}	Electric field of surface plasmon wave
S_{i}	Electric field of incident light
S_{r}	Electric field of reflected light
S_{ext}	External stress
S_T	Thermoelastic stress
q	Absorptance per unit depth
q_{all}	Absorbance
Q	Absorbed energy
E_{F}	Fermi energy
γ	Attenuation constant
γ_{a}	Optical absorption coefficient
I	Light intensity
$\tilde{I}$	Surface energy density of light
μ	Permeability
ε	Permittivity
ε'	Real part of complex permittivity
ε''	Imaginary part of complex permittivity

ε_v	permittivity in vacuum
ε_∞	Sum of intraband contributions for permittivity
n	Refractive index
R	Reflectivity
R_0	Reflectivity at room temperature
ΔR	Reflectivity change
R_e	Reflection coefficient of electron
k_x	Wave number of the in-plane direction
k_z	Wave number of the normal direction
k_{sp}	Wave number of surface plasmon wave
k_{ev}	Wave number of evanescent wave
k_c	Thermal conductivity
k_B	Boltzmann constant
K	Bulk modulus
K_T	Thermal diffusion coefficient
c_w	Acoustic wave velocity
c_{33}	Elastic constant
c_v	Light velocity in vacuum
α'	Linear thermal expansion coefficient
Γ	Damping constant
Σ	Constant giving the average of the scattering probability over the Fermi surface
Δ	Fractional Umklapp scattering
$\hbar$	Planck's constant

1. GENERAL INTRODUCTION

1.1 PURPOSE

In recent years, photoacoustic microscopy (PAM) has attracted increasing attention as a non-invasive imaging technique in biomedicine and biomedical studies [1.1, 1.2, 1.3]. This technique can obtain not only high-resolution 3D images of biological objects but also targeted functional images depending on the optical absorption. Moreover, PAM is also utilized as a multimodal imaging technique for elasticity measurement [1.4, 1.5], viscosity imaging [1.6], temperature monitoring [1.7], and doppler detection of flow speed [1.8, 1.9]. Most PAM systems consist of a pulsed laser to induce thermoelastic stress and a piezoelectric acoustic sensor to detect generated acoustic waves. The PAM systems are mainly categorized into two systems: the acoustic resolution PAM (AR-PAM) with better imaging depth and the optical resolution PAM (OR-PAM) with high radial resolution [1.10, 1.11]. In both systems, the axial resolution depends on the acoustic detection system because the information of the position in the axial direction is determined by the propagation time of the generated acoustic wave. To obtain better axial resolution, it is necessary to detect the acoustic pulsed wave with higher central frequency [1.12], which is induced by a pulsed laser with shorter duration such as sub-nanosecond [1.13, 1.14]. The detectable frequency range of the acoustic pulse is, however, limited by the bandwidth and central frequency of the acoustic sensor in the PAM system [1.12]. Therefore, an acoustic sensor with wide bandwidth is necessary to achieve high-resolution PAM.

The sensor utilizing surface plasmon resonance (SPR) had been studied as an acoustic sensor with wide bandwidth. In 1996, Schilling et al. suggested optical detection techniques of acoustic shock wave using SPR for the first time [1.15]. In 2015, Wang et al. experimentally confirmed that a simple Kretschmann-type SPR acoustic sensor with water had a flat frequency response in a wide frequency range of 0.68–126 MHz [1.16]. They also demonstrated 3D imaging of a melanosome using their optical PAM system with a pulsed laser (with pulse duration of 10 ps), and achieved high resolution imaging with radial and axial resolutions of 2.2 and 16.6 μm, respectively. In addition, several sensor designs had been suggested for improving the sensitivity of the SPR sensor. In 2013, Yakovlev et al. reported a highly sensitive SPR acoustic sensor with a lower pressure detection limit of 500 Pa by attaching a plasmonic nanorod metamaterial to the surface of the glass prism [1.17]. In 2018, Kolomenskii et al. suggested that a Kretschmann-type

SPR sensor with an additional receiving layer enabled highly sensitive and broadband detection of acoustic wave. They estimated that the detection limit of the sensor was 400 kPa in the case of a 1.0 GHz bandwidth, whereas it was 0.002 Pa with that of 10 kHz [1.18]. Thus, SPR sensors have good potential to detect ultrasound over a wide frequency range with high sensitivity by designing the construction, the film material on the glass prism, and the external medium.

The SPR sensor is then known to act as an ultrasound sensor. The SPR condition changes due to irradiated acoustic pulse, which results in changes in optical reflectivity. In order to design the SPR sensor, it is important to understand the response of optical properties to the elastic and thermal changes. Generally, Brillouin light scattering technique is a well-known method used to evaluate the elastic, thermal, and optical properties of film and bulk materials [1.19, 1.20, 1.21, 1.22, 1.23]. However, this technique only provides measurement of static properties but not that of dynamic pulse response which is necessary for the physical properties of the SPR ultrasonic sensor in high-resolution PAM system. This is because the technique is a spectroscopy technique in the frequency domain. Here, pump probe technique is a powerful tool to evaluate the elastic, thermal, and optical properties of film materials via a dynamic pulse response of the optical property because the technique is a spectroscopy technique in the time domain. Therefore, this technique is expected as one of the effective evaluation methods for metal film materials with nanometer thickness used in a Kretschmann-type SPR ultrasonic sensor. The pump probe response with a picosecond or femtosecond pulsed laser system had been applied to SPR [1.24, 1.25, 1.26, 1.27]. However, there are only few studies on the pump probe response under SPR with a sub-nanosecond pulsed laser system even though the response in the sub-nanosecond region is important for an SPR ultrasonic sensor in high-resolution PAM system.

In this thesis, the basic study on the pump probe response under SPR by a system with sub-nanosecond pulsed laser is reported. This study aims to reveal the mechanism of the sub-nanosecond pump probe response under SPR by comparisons of the experimental and theoretical investigations using a simple Kretschmann-type SPR sensor with Ag metal film. In addition, the application possibility of the sub-nanosecond pump probe method as a technique for the evaluation of SPR sensors is discussed considering the mechanism of the transient response.

1.2 OUTLINE

In this thesis, the mechanism of the sub-nanosecond pump probe response under SPR was investigated by two approaches: first, the experimental investigation using the developed sub-nanosecond pump probe system, and second, the theoretical investigation using the integrated theory on the transient pump probe response. The objective of this thesis is to elucidate the mechanism of the sub-nanosecond pump probe under SPR and to discuss the application possibility as an evaluation method for SPR sensors.

In the second chapter, Brillouin light scattering method is simply explained as one of the conventional spectroscopy techniques of thermal, elastic, and optical properties. In addition, the thermal dependence of elasticity in GaN single crystal and silica glass plate samples measured by the Brillouin light scattering method is introduced as a possible actual experiment using this technique.

In the third chapter, general information on fundamental principle of photoacoustic microscopy (PAM), surface plasmon resonance (SPR), and pump probe method are provided to supplement the general introduction in Chapter 1. In addition, reports on SPR acoustic sensors and femtosecond pump probe under SPR are introduced.

In the fourth chapter, the developed sub-nanosecond pump probe system, especially, the functions and configurations of each part in the system are explained in detail. Moreover, the transient response of an Au/Cr bimetal film sample, which was demonstrated by the developed system, is shown.

In the fifth chapter, the prepared SPR sample and the experimental investigations on the transient response under SPR by the improved sub-nanosecond pump probe system are described. First, the manufactured SPR sample with Kretschmann configuration is explained focusing on the optical properties and the morphology of the deposited metal film. Second, the preliminary measurement by the system with focusing probe light is explained. The system purposed to simply investigate the responses in the incident angle region where SPR occurs. The measured responses are also described. Finally, the detailed investigation by the improved system with straightforward probe light is explained. The system purposed to experimentally investigate the excited response under SPR in detail. The observation results are also shown in this chapter.

In the sixth chapter, the constructed theory on the pump probe response under SPR by a sub-nanosecond pump probe system is described. This theory aims to understand the mechanism of the optical reflectivity change under SPR due to the pump light irradiation. The proposed theory consists of six steps: preparation of the laser profile, temperature increase at the irradiated area of the pump light, generation of the thermoelastic stress, estimation of the permittivity change in the metal film, estimation of the reflectivity change, and final convolution process. Finally, a theoretical estimated result of the transient response under SPR is shown in this chapter.

In the seventh chapter, the mechanism of the pump probe response under SPR is discussed based on the comparison between the experimental results and the theoretical estimations. First, the validation of the proposed theory by comparisons with the experimental results is discussed. Second, the mechanism of the transient response under SPR is discussed in detail. Moreover, the application possibility as an evaluation method for SPR sensors is discussed.

Finally, Chapter 8 summarizes this study on the sub-nanosecond pump probe under SPR.

REFERENCES

[1.1] P. Beard, "Biomedical photoacoustic imaging", Interface Focus, vol. 1, pp. 602–631, May 2011.

[1.2] M. Xu and L. V. Wang, "Photoacoustic imaging in biomedicine", Rev. Sci. Instrum., vol. 77, no. 041101, Feb. 2006.

[1.3] C. Li and L. V. Wang, "Photoacoustic tomography and sensing in biomedicine", Phys. Med. Biol., Vol. 54, pp. R59–R97, Sep. 2009.

[1.4] F. Gao, X. Feng, and Y. Zheng, "Photoacoustic elastic oscillation and characterization", Opto. Express, vol. 23, no. 16, pp. 20617–20628, 2015.

[1.5] J. Li, Z. Tang, Y. Xia, Y. Lou, and G. Li, "Cell viscoelastic characterization using photoacoustic measurement ", J. Appl. Phys., vol. 104, no. 034702, Apr. 2008.

[1.6] F. Gao, X. Feng, and Y. Zheng, "Advanced photoacoustic and thermoacoustic sensing and imaging beyond pulsed absorption contrast" J. Opt., vol. 18, no. 074006, Mar. 2016.

[1.7] L. Gao C. Zhang, C. Lia, and L. V. Wang, "Intracellular temperature mapping with fluorescence-assisted photoacoustic-thermometry", Appl. Phys. Lett., vol. 102, no. 193705, May 2013.

[1.8] W. Song, W. Liu, and H. F. Zhang, "Laser-scanning Doppler photoacoustic microscopy based on temporal correlation", Appl. Phys. Lett., vol. 102, no. 203501, May 2013.

[1.9] H. Fang, K. Maslov, and L. V. Wang, "Photoacoustic doppler effect from flowing small light-absorbing particles", Phys. Rev. Lett., vol. 99, no. 184501, Oct. 2007.

[1.10] K. Maslov, G. Stoica, and L. V. Wang, "In vivo dark-field reflection-mode photoacoustic microscopy", Opt. Lett., vol. 30, no.6, pp. 625–627, Mar. 2005.

[1.11] K. Maslov, H. F. Zhang, S. Hu, and L. V. Wang, "Optical-resolution photoacoustic microscopy for in vivo imaging of single capillaries", Opt. Lett., vol. 33, no. 9, pp. 929–931, May 2008.

[1.12] B. Dong, C. Sun, and H. F. Zhang, “Optical detection of ultrasound in photoacoustic imaging”, IEEE Trans. Biomed. Eng. 2017, vol. 64, no. 1, pp. 4–15, Jan. 2018.

[1.13] E. M. Strohm, E. S. L. Berndl, and M. C. Kolios, “High frequency label-free photoacoustic microscopy of single cells”, Photoacoustics, vol. 1, pp. 49–53, Aug. 2013.

[1.14] E. M. Strohm, M. J. Moore, and M. C. Kolios, “Single cell photoacoustic microscopy: A review”, IEEE J. Sel. Top. Quantum Electron., no. 6801215, June 2016.

[1.15] A. Schilling, O. Yavas, J. Bischof, J. Boneberg, and P. Leiderer, “Absolute pressure measurements on a nanosecond time scale using surface plasmons," Appl. Phys. Lett., vol. 69, no. 27, pp. 4159–4161, Oct. 1996.

[1.16] T. Wang, R. Cao, B. Ning, A. J. Dixon, J. A. Hossack, A. L. Klibanov, Q. Zhou, A. Wang, and S. Hu, "All-optical photoacoustic microscopy based on plasmonic detection of broadband ultrasound" Appl. Phys. Lett., vol. 107, no. 153702, Oct. 2015

[1.17] V. V. Yakovlev, W. Dickson, A. Murphy, J. Mcphillips, R. J. Pollard, V. A. Podolskiy, and A. V. Zayats, "Ultrasensitive non-resonant detection of ultrasound with plasmonic metamaterials", Adv. Mater., vol. 25, pp. 2351–2356, Mar. 2013.

[1.18] A. A. Kolomenskii, E. Surovic, and H. A. Schuessler, "Optical detection of acoustic waves with surface plasmons", Appl. Opt., vol. 57, no. 20, pp. 5604–5613, June 2018.

[1.19] Y. Takagi, M. Ahart, T. Azuhata, T. Sota, K. Suzuki, and S. Nakamura, "Brillouin scattering study in the GaN epitaxial layer", Physica B, vol. 219 & 220, pp. 547–549, 1996.

[1.20] H. Ichihashi, T. Yanagitani, M. Suzuki, S. Takayanagi, M. Kawabe, S. Tomita, and M. Matsukawa, "Acoustic -wave velocities and refractive indices in an m-plane GaN single-crystal plate and c-axis oriented ScAlN films measured by Brillouin scattering techniques", Ultrason. Ferroelectr. Freq. Control, vol. 63, no. 5, pp. 117–125, May 2016.

[1.21] H. Ichihashi, T. Yanagitani, S. Takayanagi, M. Kawabe, and M. Matsukawa, "Gigahertz acoustic wave velocity measurement in GaN single crystals considering acousto-electric effect," IEEE Trans. Ultrason. Ferroelectr. Freq. Control, vol. 61, no. 8, pp. 1307–1313, Aug. 2014.

[1.22] S. Tomita, T. Yanagitani, S. Takayanagi, H. Ichihashi, Y. Shibagaki, H. Hayashi, and M. Matsukawa, "Evaluation of the acoustoelectric effect in the thickness direction of c -plane ZnO single crystals by Brillouin scattering", J. Appl. Phys., vol. 121, no. 23, June 2017.

[1.23] T. Yanagitani, H. Sano, and M. Matsukawa, "A method for measuring in-plane unidirectional electrical properties in a wide band-gap semiconductor using a Brillouin scattering method", J. Appl. Phys., vol. 108, no. 024910, July 2010.

[1.24] K. Katayama, T. Sawada, Q. Shen, and A. Harata, "Detection of photoinduced electronic, thermal, and acoustic dynamics of gold film using a transient reflecting grating method under three types of surface plasmon resonance conditions", Phys. Rev. B, vol. 58, no. 13, Apr. 1998.

[1.25] V. V. Temnov, K. A. Nelson, G. Armelles, A. Cebollada, T. Thomay, A. Leitenstorfer, and

R. Bratschitsch, "Femtosecond surface plasmon interferometer", Opt. Express, vol. 17, no. 10, Apr. 2009.

[1.26] V. V. Temnov, C. Klieber, K. A. Nelson, T. Thomay, V. Knittel, A. Leitenstorfer, D. Makarov, M. Albrecht, and R. Bratschitsch, "Femtosecond nonlinear ultrasonics in gold probed with ultrashort surface plasmons", Nat. Commun., vol. 4, no. 1468, Jan. 2013.

[1.27] J. Wang, J. Wu, and C. Guo, "Resolving dynamics of acoustic phonons by surface plasmons", Opt. Lett., vol. 32, no. 6, pp. 719–721, Dec. 2006.

2. CONVENTIONAL TECHNIQUE

Elastic, thermal, and optical properties are important for designing SPR ultrasonic sensor. Here, Brillouin light scattering (BLS) technique is well-known as a frequency-domain spectroscopy technique with non-contact and non-destructive for film and bulk materials [2.1, 2.2, 2.3, 2.4]. BLS is often applied to measurements of temperature and pressure dependence of samples [2.5, 2.6, 2.7]. The objective of this chapter is to explain the BLS method as a conventional spectroscopy technique to evaluate the thermal and elastic properties. In Section 2.1, general information on the BLS method is provided. Finally, actual experiments on thermal properties using the BLS method are introduced in Section 2.2.

2.1 BRILLOUIN LIGHT SCATTERING TECHNIQUE

BLS method is an optical spectroscopy technique in frequency domain with non-contact and nondestructive. When laser is irradiated to the sample, it causes inelastic light scattering due to the thermal phonons in the sample. This light scattering is called Brillouin light scattering (BLS). The energy and momentum of the scattering light change because of the inelastic interaction between the phonon in the material and the photon of the laser. In other words, the frequency and the wave vector of the BLS change. BLS method enables measurement of the acoustic wave velocity by evaluating the frequency shifts of the laser due to this light scattering.

Due to the inelastic interaction between the phonon in the material and the photon of the laser, the wave vector of the measured acoustic wave is defined by the optical scattering geometry. The frequency of the wave is obtained from the frequency shifts of the scattered light. Acoustic wave velocity is determined by the wave vector (wavelength) defined by the selected optical scattering geometry and the measured frequency. Thus, to select the proper optical light geometry is important in the BLS method. 90A and reflection-induced ΘA (RIΘA) scattering geometries are well-known because they enable simultaneous measurements of the longitudinal and shear wave velocities propagating in the in-plane direction of a plate sample [2.8, 2.9, 2.10, 2.11, 2.12, 2.13, 2.14, 2.15]. Conversely, 90R and 180° scattering geometries are used to measure longitudinal and shear wave velocities propagating in the normal direction of a plate sample, though the refractive index of the sample is necessary to obtain the velocities [2.12, 2.13, 2.14, 2.15, 2.16].

Fabry-Pérot interferometer (FPI) is often used to measure the frequency shift in BLS. The Sandercock-type Tandem Fabry-Pérot interferometer (TFPI) in particular is commonly used. FPI consists of a pair of two mirror plates (etalon) with the accuracy of $\lambda/100$. When the distance between the two etalons is integral multiple of half the wavelength ($\lambda/2$) of an incident light to the mirrors, the mirrors become transparent to the light. Therefore, the FPI acts as a tunable band pass filter by continuously sweeping the distance between the etalons. TFPI is consisted of two FPI in series which provides high contrast and wide tunable frequency range. Thus, the frequency shift in BLS is easily obtained by using the TFPI.

2.2 THERMAL AND ELASTIC PROPERTIES MEASURED BY BRILLOUIN LIGHT SCATTERING

In this Section, experiments on temperature dependence of acoustic wave velocity in GaN single crystal and quartz glass plate are introduced as actual measurements of thermal and elastic properties by BLS method [2.17].

2.2.1 MEASUREMENT SYSTEM

First, the samples used are explained. One of the samples used was an m-plane wurtzite GaN single crystal with *c*-axis along the in-plane direction (Mitsubishi Chemical Co.). The resistivity was 2×10^{-4} Ω·m. This sample was grown by hydride vapor-phase epitaxy method. Another sample used was a silica glass plate (Tosoh, ED-B). The front and reverse surfaces of the plate samples were optically polished.

Next, the BLS measurement system is explained. The BLS system used is shown in Fig. 2.1. The system consists of six-pass TFPI (JRS Scientific Instruments), continuous wave Ar ion laser (Coherent, Innova-304) with wavelength of 514.5 nm, and photomultiplier (Hamamatsu Photonics, R464S). The laser power near the samples was 43 mW and the diameter of the laser light focused on the sample was approximately 50 μm. The temperature of the samples was changed using a temperature control stage (Linkum, LK-600PM) during the experiment.

In this experiment, the RIΘA scattering geometry was adopted, which is shown in Fig. 2.2. A typical observed spectrum is shown in Fig. 2.3. The peaks around 14 and 7 GHz correspond to longitudinal and shear wave phonons, respectively. The acoustic wave velocity $v^{\Theta A}$ was determined by the frequency shifts of these peaks:

$$v^{\Theta A} = f^{\Theta A}\frac{\lambda}{2\sin\left(\theta'/2\right)}, \tag{2.1}$$

where $f_{\Theta A}$ is the shift frequency, λ is the wavelength of the incident laser light, and θ' is the scattering angle determined by the angle of the incident light and the reflected light. The shift frequencies were determined by fitting a Voigt function to the measured spectra.

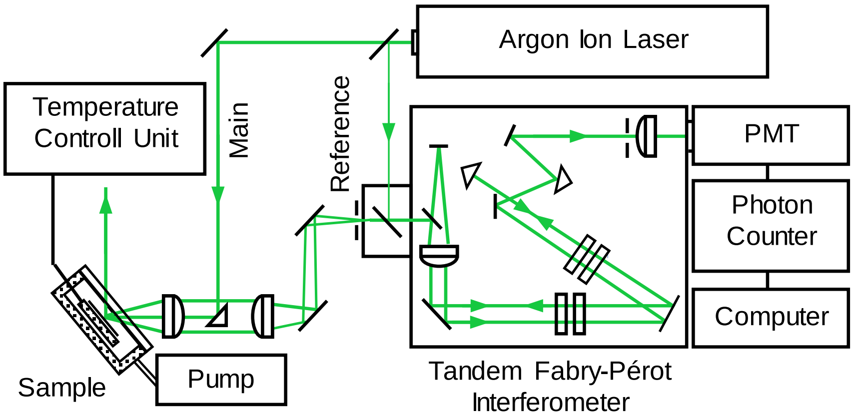

Fig. 2.1 BLS measurement system. An argon ion laser (514.5 nm) was used. Scattered light was measured using a TFPI. Recorded spectra were additionally averaged and stored on a computer.

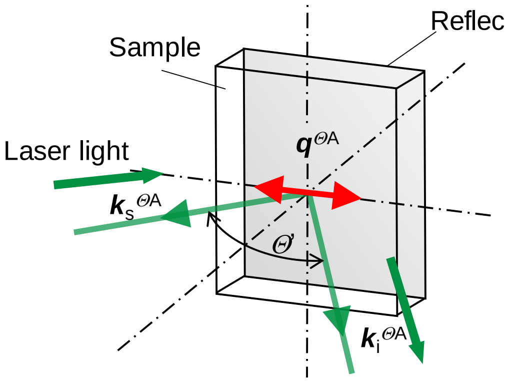

Fig. 2.2 Reflection induced ΘA (RIΘA) scattering geometry. $ki^{\Theta A}$ is the wave vector of incident light, $ks^{\Theta A}$ is the wave vector of scattered light, $q^{\Theta A}$ is the wave vector of the measured acoustic wave, and Θ' is the scattering angle. In this geometry, the sample is placed on an optical reflector.

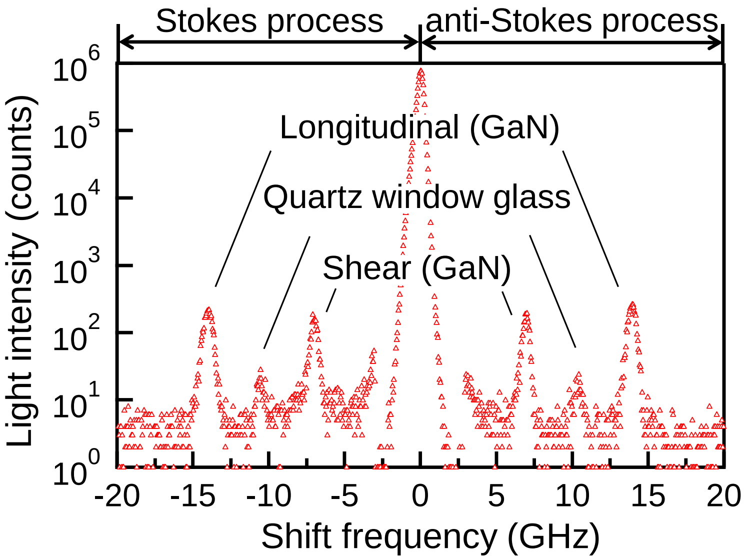

Fig. 2.3 Observed spectrum for a GaN single crystal at 293 K. Acoustic waves propagating parallel to the *c*-axis were observed. The small peaks between longitudinal and shear wave peaks of GaN resulted from the quartz window glass in front of the sample. The central peak was an elastic peak of incident reference light.

2.2.2 MEASURED THERMAL DEPENDENCE OF ELASTICITY

The thermal properties of acoustic waves in a GaN single crystal and silica glass were investigated. In the GaN single crystal, the velocities of longitudinal wave propagating parallel to the *c*-axis were measured. The measurement results for the GaN single crystal and silica glass plate samples are shown in Figs. 2.4 and 2.5, respectively. Both measured thermal dependences of the longitudinal wave velocity showed linear characteristics. Therefore, these velocity changes can be regarded as the thermal dependence of the elasticity. From Figs. 2.4 and 2.5, the normalized temperature coefficients of the longitudinal wave velocities in the GaN single crystal and silica glass plate were determined as –12.6 ppm/K and 110 ppm/K, respectively.

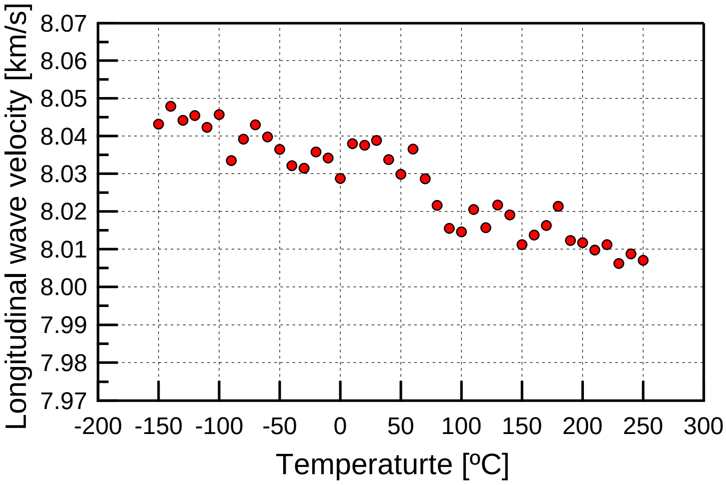

Fig. 2.4 Thermal dependence of longitudinal wave velocity in a GaN single crystal. Acoustic waves propagating parallel to the c-axis were measured [2.17].

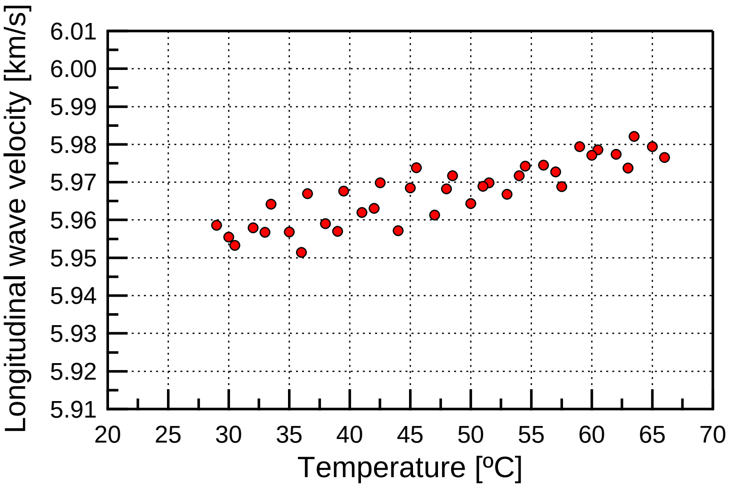

Fig. 2.5 Thermal dependence of longitudinal wave velocity in a silica glass plate.

In this way, BLS method enables measurement of elasticity and thermal properties. However, this technique enables only the measurement of static thermal dependence and resonant elastic property but not of the dynamic pulse response because of frequency-domain spectroscopy technique. For designing SPR acoustic sensors used in PAM, it is important to understand the physical properties as a pulse response. Therefore, pump probe technique is more suitable for evaluating elastic and thermal properties of film materials on a Kretschmann-type SPR sensor because this technique is a time-domain spectroscopy technique.

REFERENCES

[2.1] Y. Takagi, M. Ahart, T. Azuhata, T. Sota, K. Suzuki, and S. Nakamura, “Brillouin scattering study in the GaN epitaxial layer,” Physica B, vol. 219/220, pp. 547–549, Apr. 1996.

[2.2] G. Garlotti, F. S. Hickernell, H. M. Liaw, L. Palmieri, G. Socino, and E. Verona, “The elastic constants of sputtered aluminum nitride films,” Proc. IEEE Ultrason. Symp., vol. 1, pp. 353–356, Nov. 1995.

[2.3] M. Grimsditch, E. S. Zouboulis, and A. Polian, “Elastic constants of boron nitride,” J. Appl. Phys., vol. 76, no. 2, pp. 832–834, July 1994.

[2.4] C. S. Zha, R. J. Hemley, H. K. Mao, T. S. Duffy, and C. Meade, “Acoustic velocities and refractive index of SiO2 glass to 57.5 GPa by Brillouin scattering,” Phys. Rev. B, vol. 50, no. 18, pp. 13105–13112, Nov. 1994.

[2.5] D. Tielbürger, R. Merz, R. Ehrenfels, and S. Hunklinger, “Thermally activated relaxation processes in vitreous silica: An investigation by Brillouin scattering at high pressures,” Phys. Rev. B, vol. 45, no. 6, pp. 2751–2760, Feb. 1992.

[2.6] J. K. Krüger, K. P. Bohn, and M. Matsukawa, “The glass transition beyond the time trap: Opto-acoustic dispersion,” Phase Trans., vol. 65, issue 1–4, pp. 279–289, Mar. 1997.

[2.7] H. Yamura, M. Matsukawa, T. Otani, and N. Ohtori, “Brillouin scattering study on the elastic properties of epoxy adhesive layer,” Jpn. J. Appl. Phys., vol. 38, part 1, no. 5B, pp. 3175–3178, Jan. 1999.

[2.8] J. K. Krüger, J. Embs, J. Brierley, and R Jiménez, “A new Brillouin scattering technique for the investigation of acoustic and opto-acoustic properties: application to polymers,” J. Phys. D: Appl. Phys., vol. 31, pp. 1913–1917, Nov. 1998.

[2.9] M. Sakamoto, M. Kawabe, M. Matsukawa, N. Koizumi, and N. Ohtori, “Measurement of wave velocity in bovine bone tissue by micro-Brillouin scattering,” Jpn. J. Appl. Phys., vol. 47, no. 5, pp. 4205–4208, Feb. 2008.

[2.10] R. J. Jiménez-Riobóo, E. Rodriguez-Cañas, M. Vila, C. Prieto, F. Calle, T. Palacios, M. A. Sánchez-Garcia, F. Omnès, O. Ambacher, B. Assouar, and O. Elmazria, “Hypersonic characterization of sound propagation velocity in AlxGa1-xN thin films” J. Appl. Phys., vol. 92, no. 11, pp. 6868–6874, Sep. 2002.

[2.11] T. Azuhata, M. Takesada, T. Yagi, A. Shikanai, SF. Chichibu, K. Torii, A. Nakamura, T. Sota, G. Cantwell, D. B. Eason, and C. W. Litton, “Brillouin scattering study of ZnO,” J.

Appl. Phys., vol. 94, no. 2, pp. 968–972, Jul. 2003.

[2.12] M. Kazan, E. Moussaed, R. Nader, and P. Masri, “Elastic constants of aluminum nitride,” Phys. Stat. Sol., vol. 4, no. 1, pp. 204–207, July 2006.

[2.13] M. Yamaguchi, T. Yagi, T. Azuhata, T. Sota, K. Suzuki, S. Chichibu, and S. Nakamura, “Brillouin scattering study of gallium nitride: elastic stiffness constants,” J. Phys.: Condens. Matter, vol. 9, pp. 241–248, Jan. 2007.

[2.14] M. Yamaguchi, T. Yagi, T. Sota, T. Deguchi, K. Shimada, and S. Nakamura, “Brillouin scattering study of Bulk GaN,” J. Appl. Phys., vol. 85, no. 12, pp. 8502–8504, Mar. 1999.

[2.15] A. Polian, M. Grimsditch, and I. Grzegory, “Elastic constants of gallium nitride,” J. Appl. Phys., vol. 79, no. 6, pp. 3343–3344, Dec. 1995.

[2.16] S.-I. Tomohiro, M. Matsukawa, T. Otani, and N. Ohtori, “Brillouin scattering study on the opto-acoustic properties of thin piezoelectric polymer films,” Jpn. J. Appl. Phys., vol. 43, no. 5B, pp. 2916–2919, Feb. 2004.

[2.17] H. Ichihashi, T. Yanagitani, S. Takayanagi, M. Kawabe, and M. Matsukawa, “Gigahertz acoustic wave velocity measurement in GaN single crystals considering acousto-electric effect,” IEEE Trans. Ultrason. Ferroelectr. Freq. Control, vol. 61, no. 8, pp. 1307–1313, Aug. 2014.

3. FUNDAMENTAL PRINCIPLE

The objective of this chapter is to provide fundamental principle in order to supplement the general introduction in Chapter 1. In Section 3.1, general information on photoacoustic microscopy (PAM) are described. In Section 3.2, fundamental principle of surface plasmon resonance (SPR) and the existing application of the SPR acoustic sensor are introduced. Finally, general information on pump probe method are described in Section 3.3.

3.1 PHOTOACOUSTIC IMAGING

In this Section, fundamental information on PAM is supplied. Overall explanation about photoacoustic imaging technique is described in Subsection 3.1.1. In Subsection 3.1.2, detailed explanation of PAM is described. Finally, fundamental law determining the resolution of PAM is explained in Subsection 3.1.3.

3.1.1 PHOTOACOUSTIC TECHNIQUE

Acoustic waves are generated due to the thermal expansion excited by the optical absorption when light is irradiated to samples such as solids, liquids, gases, and biological materials. This effect is called photoacoustic (PA) effect. First, the PA effect in solid samples was discovered by Bell in 1880 [3.1]. Tyndall [3.2] and Rontgen [3.3] also discovered this effect in gases. After those decades, PA effect was widely applied to analyze gas materials with the advancement of laser technology [3.4]. In 1973, Robin et al. [3.5] and Rosencwaig [3.6] substantiated availability of spectroscopic analysis for solid materials such as sol-gel materials, powder materials, and biological objects by applying the PA effect. This analysis technique was named photoacoustic spectroscopy (PAS) by Rosencwaig.

Since the 1990s, application using the PA effect attracted attention for imaging technique of biological materials and clinical diagnosis because the optical technique enables non-invasive, non-contact, and functional analysis, which is called photoacoustic tomography (PAT) [3.7]. PAT has imaging resolution better than that of ultrasound imaging; moreover, the imaging depth in PAT is better than that of optical coherence tomography (OCT). This is because PAT makes use of the following advantages: lower wavelength of light than that of ultrasound and acoustic wave with low attenuation [3.8]. Generally, infrared (IR) or near-infrared (NIR) lasers are used for PAT applications [3.9]. This is because the optical transmissivity of water, which living matter is mostly composed of, is high in the region lower than the wavelength of around 1350 nm, and those of oxygenated hemoglobin (HbO_2) and deoxygenated hemoglobin (Hb) are high in the region higher than the wavelength of around 650 nm. This region of 650−1350 nm is called NIR window in biological tissue [3.10]. Therefore, PAT enables observations of not only surface of biological materials but also through organs by using IR or NIR lasers. PAT is categorized into photoacoustic computed tomography (PACT) and photoacoustic microscopy (PAM) according to the system structure. In PACT, macroscopic images can be obtained from information of acoustic waves excited by light irradiation with wide area. In this system, acoustic waves are detected by an array of ultrasonic sensors. PACT enables the obtainment of 3D images with resolution of around 400 μm and imaging depth of around 4.5 cm [3.11]. Specifically, systems with linearly and circularly arranged sensors are widely used, and they are called linear-array PACT [3.7, 3.11] and circular-array PACT [3.12, 3.13], respectively. The schematic images of these systems are shown in Figs 3.1 (a) and (b). In PAM, microscopic images can be obtained from information acoustic waves excited by irradiation of focused laser light on a targeted small area. In this system, acoustic waves are detected by a single acoustic sensor. PAM enables obtainment of 3D images with resolution of around 5−45 μm and imaging depth of around 1−3 mm [3.14, 3.15, 3.16]. Therefore, PACT is suitable for macroscopic imaging such as for vascular networks of brain and hand, while PAM is suitable for microscopic imaging such as for capillary and small biological tissue. More detailed explanation about PAM is described in the following Subsection 3.1.2.

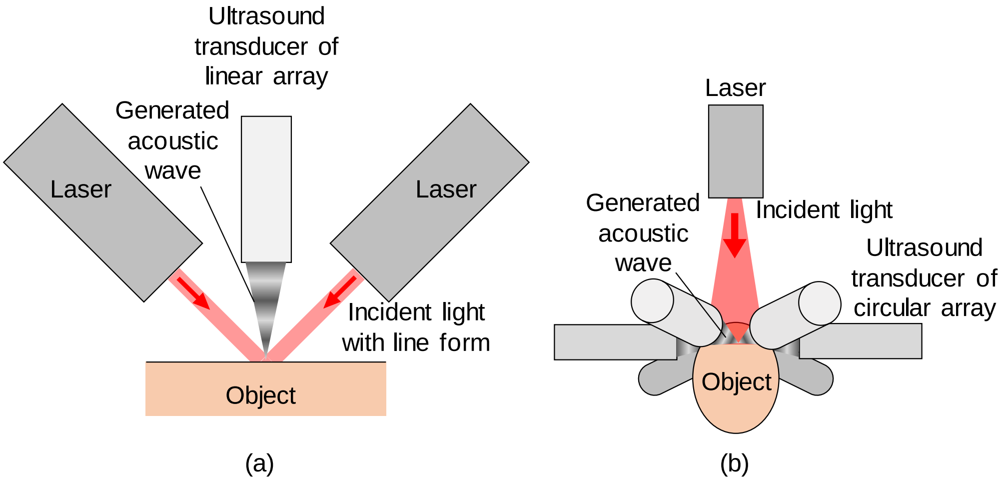

Fig. 3.1 (a) Linear array PACT system. (b) Circular array PACT system. In both techniques, the ultrasound is generated by laser irradiation and is detected by ultrasound transducers.

3.1.2 PHOTOACOUSTIC MICROSCOPY

PAM is a non-contact and non-invasive technique used to obtain microscopic images of biological materials. Most PAM systems consist of a pulsed laser and a piezoelectric acoustic sensor. When a focused laser with a specific wavelength is irradiated to a targeted area of a biological sample, thermal expansion is generated by optical absorption depending on the absorption coefficient of the wavelength. The acoustic wave generated in the biological sample propagates from the sample to the external water medium. The optical information of the sample is obtained by detecting the acoustic signals using an acoustic sensor. In addition, 3D imaging is attained by mechanical sweep of the irradiation position of the laser. To obtain high contrast 3D images, photoacoustic waves should be generated efficiently. For that reason, the pulse duration of the laser being utilized must meet two conditions of stress and thermal confinements [3.17, 3.18], which are written as:

$$\tau_0 \ll \tau_s = \frac{d_s}{c_w} \tag{3.1}$$

$$\tau_0 \ll \tau_{th} = \frac{d_s^2}{4K_T} \tag{3.2}$$

where, τ_0 is the pulse duration of the laser, τ_s is the stress relaxation time, τ_{th} is the thermal relaxation time, d_s is the characteristic linear dimension of the tissue volume being heated, K_T is the thermal diffusion coefficient, and c_w is the acoustic wave velocity of soft tissues. Generally, typical values of thermal diffusion coefficient and acoustic wave velocity of soft tissues are around 1.4×10^{-7} m^2/s and around 1500 m/s, respectively [3.19]. If the diameter of the observation area d_s is 30 μm, the thermal confinement condition in Equation (3.2) is met when the laser duration is shorter than 1.6 ms. In addition, the stress confinement condition in Equation (3.1) is met when the laser duration is shorter than 20 ns.

PAM can obtain not only high-resolution 3D images but also targeted functional images depending on the optical absorption of the sample [3.18, 3.20, 3.21]. To analyze detected acoustic waves, time-domain PA systems are widely used. In addition to that, frequency-domain [3.22] and phase-domain [3.23] PA systems were also studied. Moreover, PAM is also considered as a multimodal imaging technique [3.24]. For instance, feasibility studies of estimations of mechanical properties such as viscosity and elasticity had been conducted in time-domain systems [3.25, 3.26], frequency-domain systems [3.27, 3.28], and phase-domain systems [3.29, 3.30] using a continuous wave (CW) laser modulated with an acoustic optical modulator (AOM). The mechanical properties were estimated by applying the mass-spring oscillator model. Temperature monitoring using a PAM system had also been studied [3.31]. In addition, flow velocity measurement based on doppler shift had been studied using a frequency-domain PAM system [3.32, 3.33].

PAM systems are mainly categorized into two systems: the acoustic resolution PAM (AR-PAM) [3.14, 3.15] and the optical resolution PAM (OR-PAM) [3.16]. The schematic images of these systems are shown in Figs 3.2 (a) and (b). AR-PAM system consists of a conical lens, an annular mirror, a focus lens and a focused ultrasonic transducer. The laser light is expanded by the conical lens and then passes through the annular mirror. The annular light is focused by the focus lens. The optical focal region overlaps with the focal spot of the ultrasonic transducer, which forms a confocal optical dark-field illumination and ultrasonic detection configuration. As can be seen in Fig 3.2 (b), OR-PAM system consists of an objective lens, a collecting lens, an isosceles prism, a rhomboid prism, silicon oil, an acoustic lens and an acoustic transducer. The laser light is focused at the observation point through the two prisms and the acoustic lens. The optical focal region overlaps with the focal spot of the ultrasonic transducer. Generated acoustic waves pass through the acoustic lens and are then detected by the acoustic transducer after reflections in the rhomboid prism. AR-PAM system has an advantage of better imaging depth by taking advantage of the much lower acoustic scattering due to the coaxial structure. On the other hand, OR-PAM system has an advantage of high radial resolution by making use of the optical focus of the objective lens. In 2010, for the first time, Micro Photo Acoustic Inc. produced a PAM system with both modes: acoustic resolution and optical resolution, for commercial use [3.34]. In the AR-PAM mode, the imaging depth of the system is 3.0 mm, and the resolutions of radial and axial directions are 45 μm and 30 μm, respectively. In the OR-PAM mode, the imaging depth is 1.0 mm, and the resolutions of radial and axial directions are 5.0 μm and 30 μm, respectively.

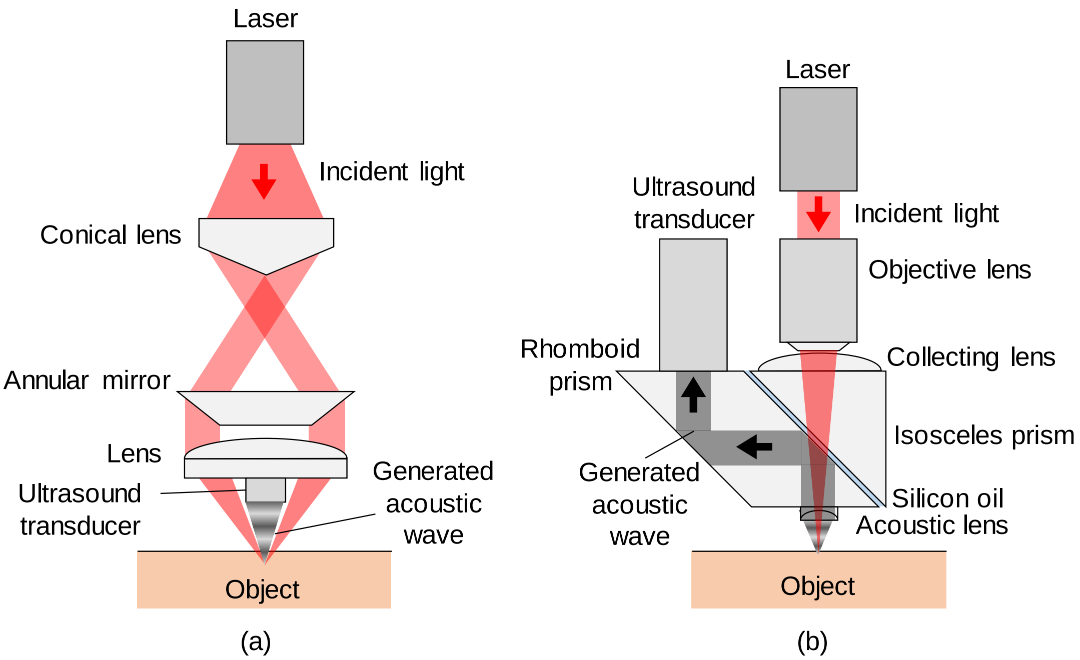

Fig. 3.2 (a) AR-PAM system. (b) OR-PAM system. In both systems, the ultrasound is generated by irradiation of focused laser and is detected by an ultrasound transducer.

3.1.3 RESOLUTION OF PHOTOACOUSTIC MICROSCOPY

When a 3D image is obtained by PAM, the irradiation position of the focused laser is swept. The position data in the in-plane direction depends on the irradiation position of the focused laser. On the other hand, the position data in the depth direction depends on the propagation time of the generated acoustic wave. Therefore, if stress and thermal confinement conditions are met, the radial resolution almost depends on the optical spot size while the axial resolution depends on the acoustic detection system. Because of it, the axial resolutions of AR-PAM and OR-PAM systems are the same. If high-resolution 3D images are demanded, the pulse acoustic wave with high frequency generated by the laser with shorter pulse duration must be detected clearly [3.35, 3.36]. The detectable frequency range of the acoustic pulse is, however, limited by the bandwidth and central frequency of the acoustic sensor in the PAM system. Therefore, an acoustic sensor with wide bandwidth is necessary to achieve high-resolution PAM. In 2015, Wang et al. developed the PAM system with high-resolution utilizing a pulsed laser with short pulse duration of 10 ps and an SPR acoustic sensor with wideband [3.37]. They also achieved 3D imaging of a melanosome with high resolution with radial and axial resolutions of 2.2 and 16.6 μm, respectively.

3.2 SURFACE PLASMON RESONANCE

In this Section, fundamental information on SPR are provided. In Subsection 3.2.1, fundamental principle on surface plasmon wave (SPW) is described. In Subsection 3.2.2, the method to excite SPR is explained. In Subsection 3.2.3, the surface plasmon resonance (SPR) curve of reflectivity is described. Finally, applications of SPR focusing on the aspect of its utilization as acoustic sensors are explained in Subsection 3.2.4.

3.2.1 SURFACE PLASMON WAVE

Plasma is one of the four fundamental states, which was explained for the first time by Langmuir in 1920 [3.38]. It consists of a freely mobile gas of ions and/or free electrons. Thus, metals with many free electrons meet the condition of plasma. Collective oscillation of ions or free electrons is called plasmon, which was proposed for the first time by Pines and Bohm in 1951 [3.39, 3.40, 3.41]. The collective oscillation of free electrons in metals is also plasmon. Schematic images of plasmon are shown in Figs. 3.3 (a). As can be seen in Fig. 3.3 (a), plasmon in metal exists as a longitudinal wave, which is called bulk plasmon wave (BPW). An external electromagnetic wave is excited by the BPW at the surface of the metal. As can be seen in Fig. 3.3 (b), the excited electromagnetic wave behaves as an apparent transverse wave, which is called surface plasmon polariton wave. Generally, it is called surface plasmon wave (SPW). Ritchie predicted the behavers of SPW for the first time in 1957 by theoretical estimation of the dispersion relation for metal film [3.42]. Teng and Stern experimentally measured the dispersion relation of SPW in 1967 [3.43].

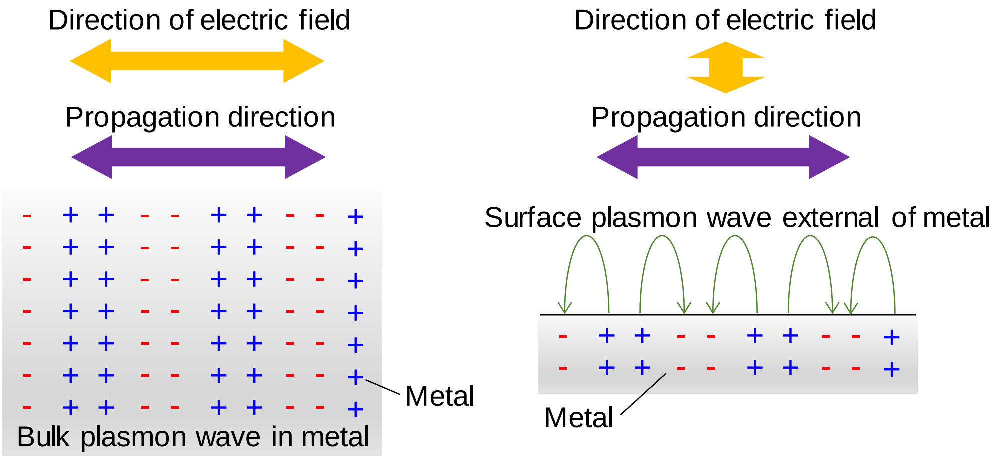

Fig. 3.3 Schematic images of (a) BPW in metal and (b) SPW external of metal surface.

Here, existence condition of SPW is described. First, the contact state of two different media: A and B, is displayed as the interface in Fig. 3.4. The electromagnetic wave, which is assumed to be SPW, propagates along the interface and attenuates in the normal direction. Then, the electromagnetic wave in each medium is given below:

$$S_{\mathrm{SPWA}} = S_{\mathrm{SPW0}} \exp[i(k_{\mathrm{A}x}x - \omega t)] \exp(-\gamma_{\mathrm{A}} z) \qquad (z \geq 0) \tag{3.3}$$

$$S_{\mathrm{SPWB}} = S_{\mathrm{SPW0}} \exp[i(k_{\mathrm{B}x}x - \omega t)] \exp(\gamma_{\mathrm{B}} z) \qquad (z \leq 0) \tag{3.4}$$

where, S_{SPWA} and S_{SPWB} are the electromagnetic waves in media A and B, respectively. S_{SPW0} is the intensity of the electromagnetic wave, $k_{\mathrm{A}x}$ and $k_{\mathrm{B}x}$ are the wave numbers in the in-plane direction, ω is the angular frequency, and γ_{A} and γ_{B} are the attenuation constants. If S_{SPWA} and S_{SPWB} are transverse electric (TE) waves, they should be electric fields. On the other hand, if S_{SPWA} and S_{SPWB} are transverse magnetic (TM) waves, they should be magnetic fields. Here, normal components of the electric flux density and the magnetic flux density must be continuous like below:

$$\frac{1}{\varepsilon_{\mathrm{A}}} \frac{\partial S_{\mathrm{SPWA}}}{\partial z}\bigg|_{z=0} = \frac{1}{\varepsilon_{\mathrm{B}}} \frac{\partial S_{\mathrm{SPWB}}}{\partial z}\bigg|_{z=0} \qquad \text{(TM wave)} \tag{3.5}$$

$$\frac{1}{\mu_{\mathrm{A}}} \frac{\partial S_{\mathrm{SPWA}}}{\partial z}\bigg|_{z=0} = \frac{1}{\mu_{\mathrm{B}}} \frac{\partial S_{\mathrm{SPWB}}}{\partial z}\bigg|_{z=0} \qquad \text{(TE wave)} \tag{3.6}$$

where, ε_A and ε_B are the permittivity of each medium. μ_A and μ_B are the permeability of each medium. Therefore, conditions below must be met.

$$\frac{\varepsilon_\mathrm{A}}{\varepsilon_\mathrm{B}} = -\frac{\gamma_\mathrm{A}}{\gamma_\mathrm{B}} \qquad \text{(TM wave)} \tag{3.7}$$

$$\frac{\mu_\mathrm{A}}{\mu_\mathrm{B}} = -\frac{\gamma_\mathrm{A}}{\gamma_\mathrm{B}}. \qquad \text{(TE wave)} \tag{3.8}$$

In optical region, permeability is generally constant to 1. Therefore, the electromagnetic wave must be TM wave for the existence of SPW. In addition, permittivity of either medium must be negative. For instance, noble metals such as gold, silver and copper have negative permittivity. From Equations (3.3) and (3.4), the wave number of the SPW is expressed below:

$$k^2 = k_{\mathrm{A}x}^2 + k_{\mathrm{A}z}^2 = k_{\mathrm{A}x}^2 - \gamma_\mathrm{A}^2 = \varepsilon_\mathrm{A}\left(\frac{\omega}{c_\mathrm{v}}\right)^2 \qquad (z \geq 0) \tag{3.9}$$

$$k^2 = k_{\mathrm{B}x}^2 + k_{\mathrm{B}z}^2 = k_{\mathrm{B}x}^2 - \gamma_\mathrm{B}^2 = \varepsilon_\mathrm{B}\left(\frac{\omega}{c_\mathrm{v}}\right)^2 \qquad (z \leq 0) \tag{3.10}$$

where, $k_{\mathrm{A}z}$ and $k_{\mathrm{B}z}$ are the wave numbers in the normal direction. c_v is the light velocity in vacuum. Next, the dispersion relation of the SPW is obtained by substituting Equation (3.9) and (3.10) in the existence of the condition in Equation (3.7), which is written like below:

$$k_x = \left(\frac{\omega}{c_\mathrm{v}}\right)\left(\frac{\varepsilon_\mathrm{A}\varepsilon_\mathrm{B}}{\varepsilon_\mathrm{A}+\varepsilon_\mathrm{B}}\right)^{\frac{1}{2}}. \tag{3.11}$$

In Equation (3.11), in-plane components of wave number in media A and B are assumed to be same ($k_x = k_{\mathrm{A}x} = k_{\mathrm{B}x}$) because the in-plane components of the electric and magnetic fields must be continuous at the interface. When medium A is metal, permittivity ε_A is complex permittivity of $\varepsilon_\mathrm{A} = \varepsilon_\mathrm{A}' + i\varepsilon_\mathrm{A}''$. The dispersion relation of the SPW is also described below:

$$k_x = \left(\frac{\omega}{c_\mathrm{v}}\right)\left[\frac{(\varepsilon_\mathrm{A}'+i\varepsilon_\mathrm{A}'')\varepsilon_\mathrm{B}}{(\varepsilon_\mathrm{A}'+i\varepsilon_\mathrm{A}'')+\varepsilon_\mathrm{B}}\right]^{\frac{1}{2}} \tag{3.12}$$

$$\mathrm{Re}(k_x) = \left(\frac{\omega}{c_\mathrm{v}}\right)\left(\frac{\varepsilon_\mathrm{A}'\varepsilon_\mathrm{B}}{\varepsilon_\mathrm{A}'+\varepsilon_\mathrm{B}}\right)^{\frac{1}{2}} \tag{3.13}$$

$$\mathrm{Im}(k_x) = \left(\frac{\omega}{c_\mathrm{v}}\right)\left(\frac{\varepsilon_\mathrm{A}'\varepsilon_\mathrm{B}}{\varepsilon_\mathrm{A}'+\varepsilon_\mathrm{B}}\right)^{\frac{3}{2}}\left[\frac{\varepsilon_\mathrm{A}''}{2(\varepsilon_\mathrm{A}')^2}\right]. \tag{3.14}$$

The real part of the dispersion relation of Equation (3.13) decides the wavelength of the SPW. While, the imaginary part of the dispersion relation of Equation (3.14) involves the attenuation.

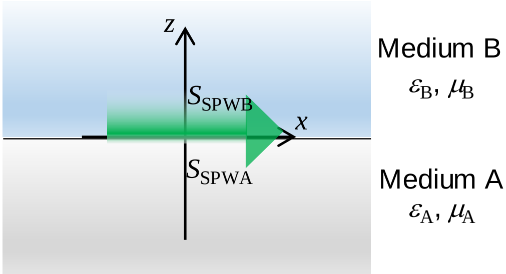

Fig. 3.4 A conceptual image of electromagnetic wave propagating along the interface and attenuating in the normal direction. S_{SPWA} and S_{SPWB} are the electromagnetic waves in media A and B. ε_{A} and ε_{B} are the permittivity of each medium. μ_{A} and μ_{B} are the permeability of each medium.

3.2.2 EXCITATION METHODS OF SURFACE PLASMON RESONANCE

To obtain the resonant condition between the SPW and the propagation light in free space, both waves must exist in the same area and their polarizations must be the same. Moreover, their energies and momentums must be the same like below:

$$\hbar k = \hbar k_{\mathrm{sp}} \tag{3.15}$$

$$\hbar \omega = \hbar \omega_{\mathrm{sp}} \tag{3.16}$$

where, k_{sp} and ω_{sp} are the wave number and the angular frequency of SPW, respectively. $\hbar$ is the Planck's constant. However, it is impossible that the SPW and the propagation light in free space couple because both dispersion relations do not overlap. Typical dispersion relation between the SPW and the propagation light in free space is shown in Fig. 3.5.

In 1968, Otto proposed the excitation method of SPW using total reflection configuration consisting of a prism and a metal placed adjacent to the prism with a small gap [3.44]. This is called Otto configuration. At nearly the same time, Kretschmann and Raether also proposed another excitation method using total reflection configuration with a prism of which metal thin film is deposited on its surface [3.45]. This is called Kretschmann configuration. Both configurations are shown in Figs 3.6 (a) and (b).

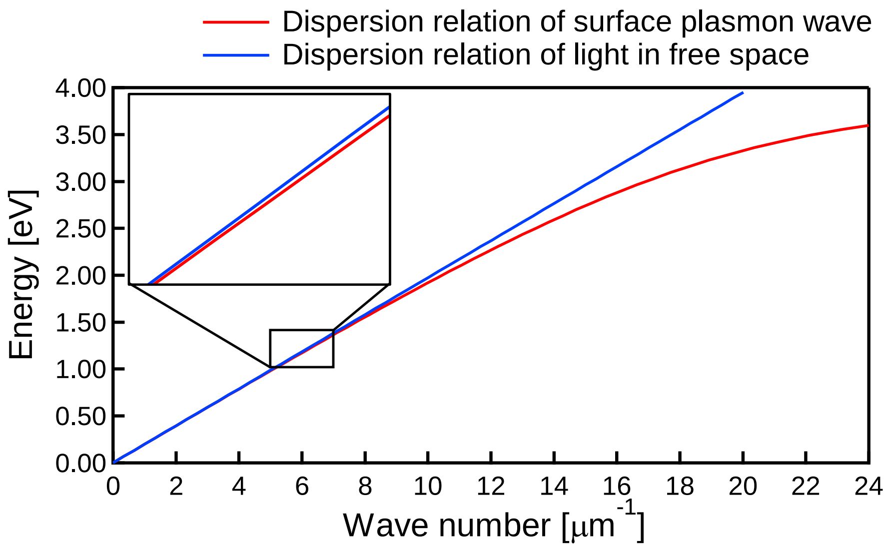

Fig. 3.5 Typical dispersion relation between surface plasmon wave and light in free space. The dispersion relation was estimated assuming that the Krestchmann configuration is consisted of Ag metal film and BK7 glass prism.

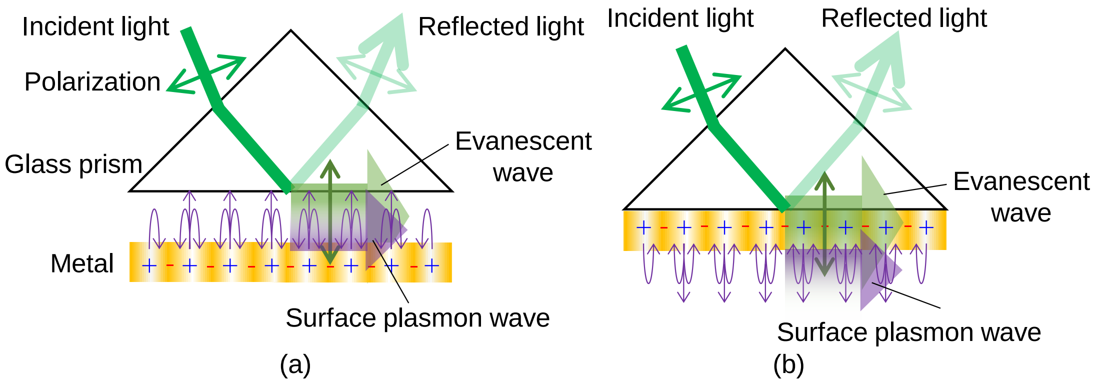

Fig. 3.6 (a) Otto configuration. (b) Kretschmann configuration.

Both configurations make use of the excited evanescent wave (EVW) to obtain SPR. In Otto configuration, the EVW and the SPW overlap in the gap between the metal and the glass prism, and then SPR occurs. In Kretschmann configuration, the EVW and the SPW overlap at the external area of the metal film, and then SPR occurs. Here, the excitation method of SPR is explained focusing on Kretschmann configuration. When the incident light passes through the glass prism, it reflects on the interface between the surface of the glass prism and the metal film. If the incident angle is larger than the critical angle, the total reflection occurs and EVW is excited. The EVW also propagates toward the external of the glass prism with drastic attenuation. Because the component of the in-plane direction of the incident light is preserved at the interface, the dispersion relation of the excited EVW is written below:

$$k_{\mathrm{ev}} = k_x = \sqrt{\varepsilon_{\mathrm{g}}}\frac{\omega}{c_{\mathrm{v}}}\sin\theta_{\mathrm{i}} \tag{3.17}$$

where, k_{ev} is the wave number of the EVW, k_{x} is the component of the in-plane direction of wave number in the glass prism, ε_{g} is the permittivity of the glass prism, and θ_{i} is the incident angle in the glass prism. As can be seen in Equation (3.17), the wave number is variable by adjusting the incident angle. Therefore, SPR occurs by adjusting the incident angle such that the momenta of the SPW and the EVW match. From Equations (3.13) and (3.17), the resonant condition is described below:

$$\mathrm{Re}(k_{\mathrm{sp}})\left[= \left(\frac{\omega}{c_0}\right)\left(\frac{\varepsilon'_{\mathrm{m}}\varepsilon_{\mathrm{g}}}{\varepsilon'_{\mathrm{m}}+\varepsilon_{\mathrm{g}}}\right)^{\frac{1}{2}}\right] = k_{\mathrm{ev}}\left[= \sqrt{\varepsilon_{\mathrm{g}}}\frac{\omega}{c_0}\sin\theta_{\mathrm{i}}\right] \tag{3.18}$$

where, ε_{m}' is the real part of the permittivity of metal film. Typical dispersion relations are shown in Fig. 3.7. The SPW in Ag metal film and the EVW excited by Kretschmann configuration consisting of a BK7 glass prism and an Ag metal film were assumed in the estimations of Fig. 3.7. The incident angle was assumed to be 43.8°. The SPW then occurs at the wavelength of 532 nm.

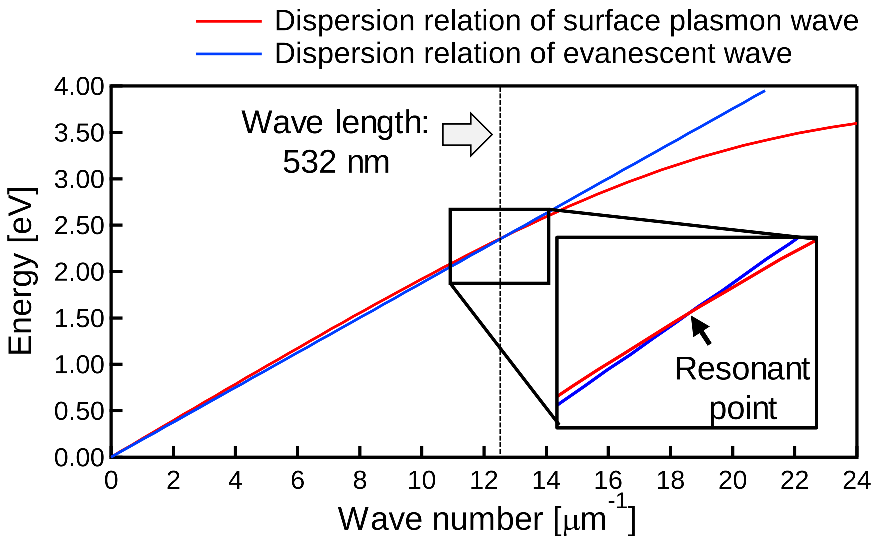

Fig. 3.7 Typical dispersion relations of EVW and SPW.

3.2.3 SPR CURVE

When SPR occurs, the reflectivity decreases drastically. It means that the energy of the incident light transfers to the SPW and is then converted to thermal energy. Therefore, SPR is easily observed by measuring the incident angle dependence of the reflectivity, which is called surface plasmon resonance (SPR) curve. Here, SPR curve is explained focusing on Kretschmann configuration.

Here, multiple reflection model is used to assume SPR curve. A schematic image is shown in Fig. 3.8. Then, the incident light with p-polarization irradiates to the surface of the metal film from the glass prism. The incident light separates into reflected light and transmitted light. The transmitted light enters toward the interface between the metal film and the air. This light also separates into reflected light and transmitted light. The light reflected at the interface between the metal film and the air enters toward the interface between the metal film and the glass prism. This light separates into light transmitting to the glass prism and light returning to the interface between the metal film and the air. In this model, the total light returning to the glass prism is defined as the reflected light. Likewise, the total light passing toward the air is defined as the transmitted light.

Here, the reflectivity and the transmittivity of the intensity of electric field at each interface are expressed in following Fresnel equations. The reflectivity $r_{\text{g-m}}$ at the interface between the glass prism and the metal film is described as below when the light enters toward the metal film from the glass prism:

$$r_{\mathrm{g-m}} = \frac{\sqrt{\varepsilon_{\mathrm{g}}}\cos\theta'_{\mathrm{m}} - \sqrt{\varepsilon_{\mathrm{m}}}\cos\theta_{\mathrm{g}}}{\sqrt{\varepsilon_{\mathrm{g}}}\cos\theta'_{\mathrm{m}} + \sqrt{\varepsilon_{\mathrm{m}}}\cos\theta_{\mathrm{g}}} \tag{3.19}$$

where, ε_{g} and ε_{m} are the permittivities of the glass prism and the metal film, respectively. θ_{g} is the incident angle in the glass prism and θ'_{m} is the refractive angle in the metal film. The reflectivity $r_{\text{m-g}}$ at the interface between the metal film and the glass prism is described as below when the light enters toward the glass prism from the metal film:

$$r_{\mathrm{m-g}} = -r_{\mathrm{g-m}}. \tag{3.20}$$

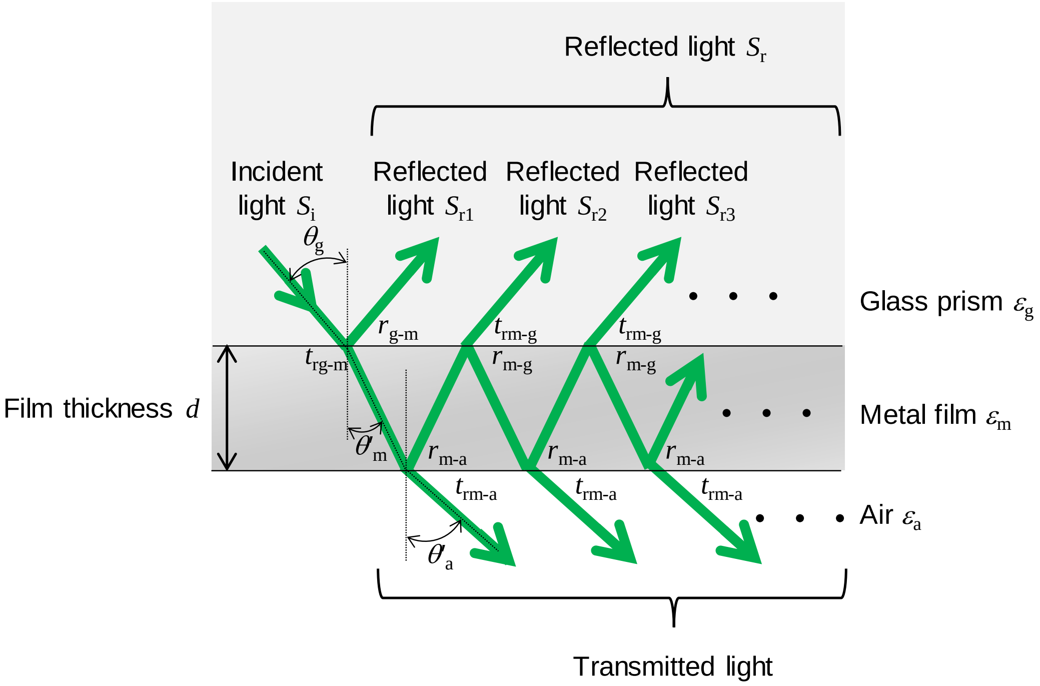

Fig. 3.8 Schematic image of multiple reflection model. S_i is the incident light. S_r is the reflected light. r and t_r are the reflectivity and transmittivity, respectively. θ_g is the incident angle in the glass prism. θ'_m and θ'_a are the refractive angles in the metal film and the air. ε_g, ε_m and ε_a are the permittivities of the glass prism, the metal film and the air, respectively. d is the film thickness.

Similarly, when the light enters toward the air from the metal film, the reflectivity $r_{m\text{-}a}$ at the interface between the metal film and the air is described as below:

$$r_{m-a} = \frac{\sqrt{\varepsilon_m}\cos\theta'_a - \sqrt{\varepsilon_a}\cos\theta'_m}{\sqrt{\varepsilon_m}\cos\theta'_a + \sqrt{\varepsilon_a}\cos\theta'_m} \tag{3.21}$$

where, ε_a is the permittivity of the air and θ_a is the refractive angle in the air. The transmittivity $t_{rg\text{-}m}$ at the interface between the glass prism and the metal film is described as below when the light enters toward the metal film from the glass prism:

$$t_{rg-m} = 1 + r_{g-m}. \tag{3.22}$$

When the light enters toward the glass prism from the metal film, the transmittivity $t_{rm\text{-}g}$ is also described as below:

$$t_{rm-g} = 1 + r_{m-g}. \tag{3.23}$$

Similarly, when the light enters toward the air from the metal film, the transmittivity $t_{\mathrm{rm\text{-}a}}$ at the interface between the metal film and the air is described as below:

$$t_{\mathrm{rm-a}} = 1 + r_{\mathrm{rm-a}}. \tag{3.24}$$

Following Snell's law, the refractive angles in the metal film and the air are then described in the following equations:

$$\theta'_{\mathrm{m}} = \cos^{-1}\sqrt{1 - \frac{\varepsilon_{\mathrm{g}}}{\varepsilon_{\mathrm{m}}}\sin^2\theta_{\mathrm{g}}} \tag{3.25}$$

$$\theta'_{\mathrm{a}} = \cos^{-1}\sqrt{1 - \frac{\varepsilon_{\mathrm{g}}}{\varepsilon_{\mathrm{a}}}\sin^2\theta_{\mathrm{g}}}. \tag{3.26}$$

Next, each intensity of electric field component of the reflected lights shown in Fig. 3.8 is expressed using Equations (3.19) – (3.26), which is written below:

$$S_{\mathrm{r}l} = S_{\mathrm{i}}\left(r_{\mathrm{g-m}}\right) \quad (l = 1) \tag{3.27}$$

$$S_{\mathrm{r}l} = S_{\mathrm{i}}\frac{t_{\mathrm{rg-m}}t_{\mathrm{rm-g}}}{r_{\mathrm{m-g}}}\left[r_{\mathrm{m-a}}r_{\mathrm{m-g}}\exp(2ik_{\mathrm{m}z}d)\right]^{l} \quad (l > 1) \tag{3.28}$$

where, S_{i} is the intensity of electric field component of the incident light, $k_{\mathrm{m}z}$ is the wave number of the thickness direction in the metal film, d is the thickness of the metal film and l is an integer. Considering the wave number of EVW written in Equation (3.17), $k_{\mathrm{m}z}$ is described as below:

$$k_{\mathrm{m}z} = \sqrt{(k_{\mathrm{m}})^2 - (k_{\mathrm{ev}})^2} = \sqrt{\varepsilon_{\mathrm{m}}\left(\frac{\omega}{c_{\mathrm{v}}}\right)^2 - k_{\mathrm{ev}}^2} \tag{3.29}$$

$$k_{\mathrm{ev}} = k_{\mathrm{m}x} = \frac{\omega}{c_{\mathrm{v}}}\sqrt{\varepsilon_{\mathrm{m}} - \varepsilon_{\mathrm{m}}\cos^2\theta_{\mathrm{m}}}. \tag{3.30}$$

Here, the sum of intensities of electric field component of the reflected lights is written below:

$$S_{\mathrm{r}} = \sum_{l=1}^{\infty} S_{\mathrm{r}l} = S_{\mathrm{i}}\left(r_{\mathrm{g-m}}\right) + \sum_{l=2}^{\infty} S_{\mathrm{i}}\frac{t_{\mathrm{rg-m}}t_{\mathrm{rm-g}}}{r_{\mathrm{m-g}}}\left[r_{\mathrm{m-a}}r_{\mathrm{m-g}}\exp(2ik_{\mathrm{m}z}d)\right]^{l}. \tag{3.31}$$

A formula of series expansion, shown below, is then used to simplify the Equation (3.31).

$$\sum_{l=0}^{\infty} x^{l} = \frac{1}{1-x} \tag{3.32}$$

Therefore, the reflectivity of electric field component r is described below:

$$r = \frac{S_{\mathrm{r}}}{S_{\mathrm{i}}} = \frac{r_{\mathrm{g-m}} + r_{\mathrm{m-a}} \exp\left(2ik_{\mathrm{m}z}d\right)}{1 + r_{\mathrm{g-m}} r_{\mathrm{m-a}} \exp\left(2ik_{\mathrm{m}z}d\right)}. \tag{3.33}$$

Finally, the reflectivity of light intensity R is written by the following equation:

$$R = |r|^2. \tag{3.34}$$

Here, R is a function of incident angle θ_{g}. It implies that the SPR curve is based on the incident angle dependence of the reflectivity of light intensity $R(\theta_{\mathrm{g}})$. The estimated SPR curves are shown in Fig. 3.9. These estimations are assumed to be in Kretschmann configuration with a BK7 glass prism and each noble metal film of Ag, Au, Cu or Al. A schematic image of the assumed model is shown in Fig. 3.10. The parameters used for the estimations of Fig. 3.9 are listed in Table .3.1. Here, SPR curves were estimated at the wavelength higher than the optical absorption wavelengths of the metal films. Ag, Au, Cu and Al then have an absorption wavelength at 326, 539, 590 and 879 nm, respectively [3.46, 3.47, 3.48, 3.49, 3.50, 3.51]. For this reason, the SPR curve with Ag metal film was estimated at the wavelength of 532 nm which is the wavelength of the second harmonic of Yttrium Aluminum Garnet (YAG) laser. Similarly, the SPR curves with Au and Cu metal films were estimated at the wavelength of 790 nm which is the wavelength of a Titanium Sapphire (Ti-Sapphire) laser. The SPR curve with Al metal film was also estimated at the wavelength of 1064 nm which is the wavelength of a YAG laser. The permittivity of the Ag metal film used was estimated by the modulated Drude model, which is described in Chapter 6. The SPR curve near the minimum reflectivity is called dip, and the angle at the peak of the dip is called SPR angle. As can be seen in Fig. 3.9, SPR occurs at the angle higher than the critical angle which depends on the permittivities of the glass prism used and the external medium. The SPR curves of Fig. 3.9 were estimated with the film thicknesses as the reflectivities at the dips became minimum. These estimations resulted from the assumptions that the film thicknesses of Ag, Au, Cu and Al were approximately 51, 32, 32 and 8.5 nm, respectively, to excite the SPR.

As supplemental materials, the estimation results of SPR curve for different film thickness of Ag metal film are shown in Fig. 3.11. Reflectivity at the SPR angle became minimum when the film thickness was approximately 50 nm. The width of the dip sharpened with increasing film thickness, while it broadened with decreasing film thickness. Therefore, the film thickness must be appropriate to excite SPR efficiently.

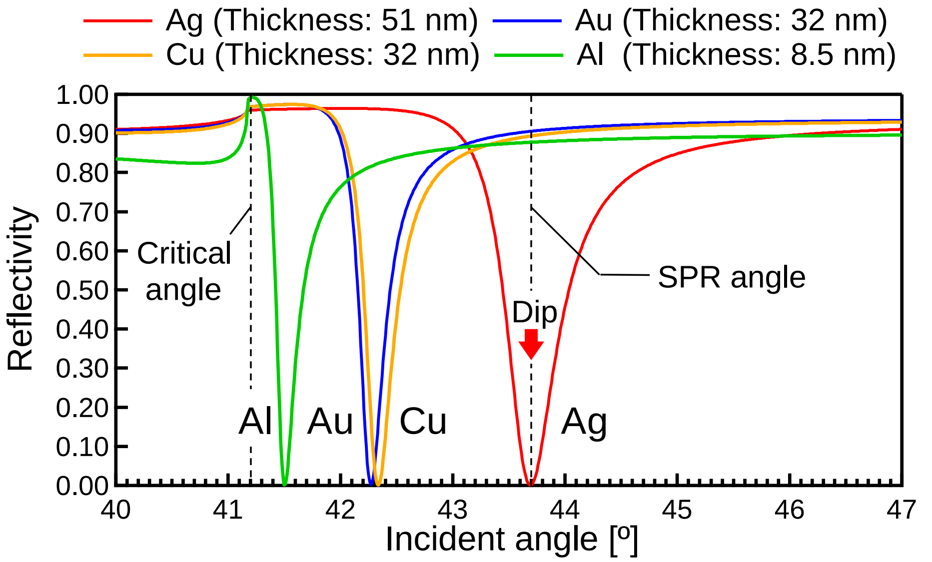

Fig. 3.9 Estimation results of SPR curves assuming that the Kretschmann configuration is consisted of BK7 glass prism and Ag, Au, Cu or Al metal film. The parameters used in these estimations are listed in Table 3.1.

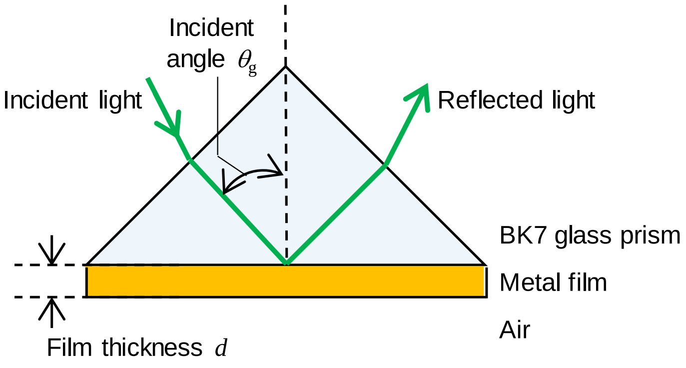

Fig. 3.10 A schematic image of the model used for the estimations of Fig. 3.9.

Table. 3.1 Parameters used in the estimations of Fig. 3.9.

Film	**λ [nm]**	**Absorption λ [nm]**	**Re (ε_m)**	**Im (ε_m)**	**Thickness [nm]**	**Ref.**
Ag	532 (SH of YAG laser)	326	−11.18	0.55	51	Chapter 6
Au	790 (Ti-Sapphire laser)	539	−25.25	1.43	32	[3.34], [3.47] [3.51], [3.52]
Cu	790 (Ti-Sapphire laser)	590	−24.02	1.37	32	[3.46], [3.47] [3.48], [3.52]
Al	1064 (YAG laser)	879	−118.1	13.25	8.5	[3.49], [3.50] [3.51], [3.52]

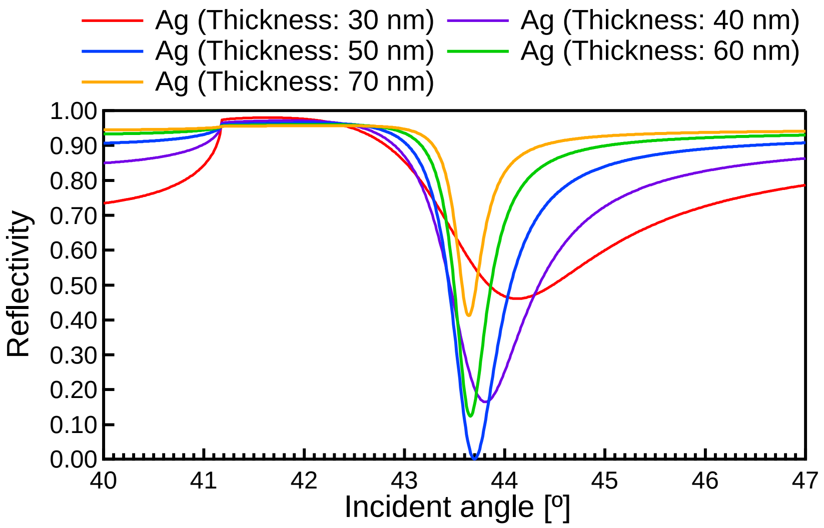

Fig. 3.11 SPR curves estimated with different film thickness of Ag metal film. The wavelength of the light was assumed to be 532 nm.

3.2.4 SPR SENSORS

Since proposals of excitation methods of SPR by Otto [3.44], Kretschmann and Raether [3.45], an application for gas detection was reported for the first time by Nylander et al. in 1983 [3.53]. In addition, Liedberg et al. reported an application of SPR as a biosensor in 1984 [3.54]. In 1990, Pharmacia Biosensor inc. produced an SPR affinity sensor system based on antigen-antibody reaction for commercial use for the first time. Since then, SPR had an attractive attention in the chemical and biological studies such as gas concentration monitoring [3.55] and selective affinity sensor utilizing antigen-antibody reaction [3.56]. SPR applications for detecting mechanical characteristics were also studied. Focusing on the applications for detection of mechanical characteristics, SPR sensors are explained below.

In 1996, Schilling et al. suggested that a simple Kretschmann-type SPR sensor with external medium of water has a potential for absolute measurement of amplitude of acoustic shock wave for the first time [3.57]. The reported measurement system to estimate the detection capacity of the SPR sensor is shown in Fig. 3.12 (a-1). The detection capacity of the SPR sensor and the measured wave form are shown in Figs. 3.12 (a-2) and (a-3), respectively. In their studies, shock acoustic waves were generated by irradiating a pulsed laser on a glass plate with Ag metal film. The generated shock waves were measured as changes of the SPR angle. A He-Ne CW probe laser was used in their detection system. Their system had a time resolution of a nanosecond. In 1999, Boneberg et al. attained 2D measurements of acoustic shock wave by a SPR sensor [3.58]. In their studies, essential capability of the local measurement of SPR sensor was utilized. This is because SPR sensor enables measurements in the spot area of the laser irradiation. In 2007, Nuster et al. also suggested optical detection techniques of ultrasound using SPR with Otto and Kretschmann configurations [3.59]. According to their studies, SPR sensor with Otto configuration has a potential to measure the displacement of an acoustic wave, while that of with Kretschmann configuration has a potential to measure the stress. In 2015, Wang et al. experimentally confirmed that a simple Kretschmann-type SPR acoustic sensor with water had a flat frequency response in a wide frequency range of 0.68–126 MHz [3.37]. They also developed an all-optical PAM system with a simple Kretschmann-type SPR acoustic sensor. The system is shown in Fig. 3.12 (b-1). An enlarged view of the SPR sensor used is also shown in Fig. 3.12 (b-2). They also demonstrated imaging of a melanosome by their system with a pulsed laser (pulse duration of 10 ps), utilizing the wideband characteristics of the SPR acoustic sensor. They achieved high resolution 3D imaging with radial and axial resolutions of 2.2 and 16.6 μm, respectively. The reported image is shown in Fig. 3.12 (b-3).

Several sensor designs have been suggested in order to improve capability of sensitivity for SPR sensor. In 2013, Yakovlev et al. reported a high-sensitive SPR acoustic sensor with a lower pressure detection limit of 500 Pa by attaching a plasmonic nanorod metamaterial to the surface of the glass prism [3.60]. The reported SPR sensor is shown in Fig. 3.12 (c). In 2018, Kolomenskii et al. suggested that a Kretschmann-type SPR sensor with an additional receiving layer enabled the highly sensitive and broadband detection of the acoustic wave. The reported SPR sensor is shown in Fig. 3.12 (d). They estimated that the detection limit of the sensor was 400 kPa in the case of a 1.0 GHz bandwidth, whereas it was 0.002 Pa with that of 10 kHz [3.61].

SPR sensors enable detections of acoustic wave in non-resonance by measuring the changes of the reflectivity or the SPR angle. SPR sensors also enable con-contact and local measurements because they can only detect the spot area irradiated by the probe light. Therefore, SPR sensors have good potential to detect ultrasound over a wide frequency range with high sensitivity and are suitable for imaging of 3D acoustic pressure distribution. The capability of SPR sensor depends on the construction, the film metal material and the external medium. Especially, the dynamic responses of optical properties to the elastic and thermal changes in the materials used in the SPR sensor are important for designing the structure and selecting the part materials.

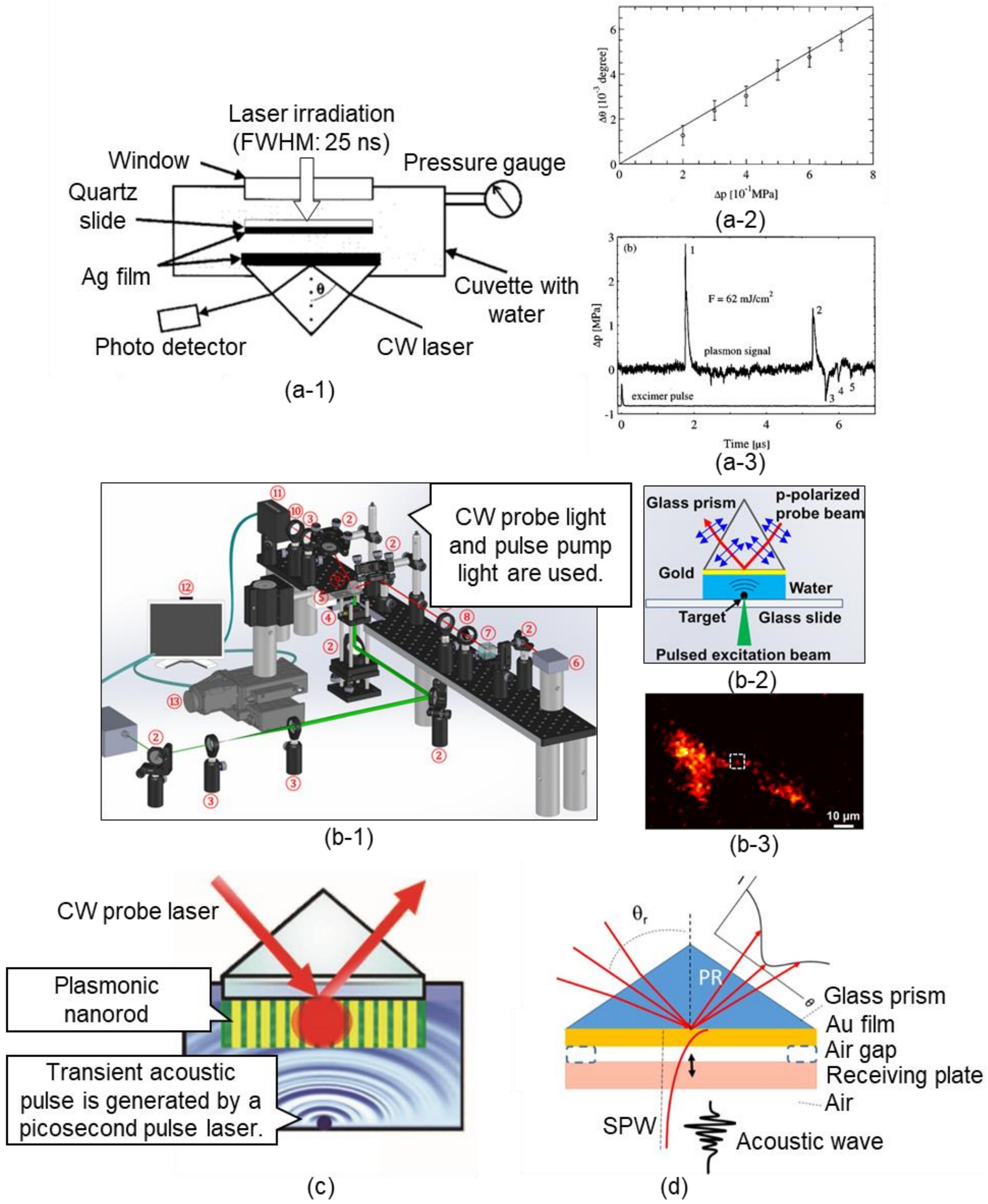

Fig. 3.12 Supplemental images of the reported SPR acoustic sensors.
(a-1) The measurement system reported by Schilling et al [3.57].
(a-2) The detection capacity of the reported SPR acoustic sensor [3.57].
(a-3) The wave form measured by the SPR sensor [3.57].
(b-1) The PAM system with SPR acoustic sensor reported by Wang et al. [3.58].
(b-2) An enlarged view of the reported SPR sensor [3.58].
(b-3) A melanosome image obtained by the PAM with the SPR sensor [3.58].
(c) The SPR sensor with plasmonic nanorods reported by Yakovlev et al. [3.60].
(d) The SPR sensor with an additional receiver reported by Kolomenskii et al. [3.61].

3.3 PUMP PROBE METHOD

In this Section, fundamental information on pump probe method are supplied. In Subsection 3.3.1, pump probe method is explained with a broad sense. In Subsection 3.3.2, pump probe method is explained focusing on pulse probe method. Finally, previous reports of pump probe method with SPR are introduced in Subsection 3.3.3.

3.3.1 PUMP CW/PULSE PROBE METHODS

The time-domain spectroscopy technique for measurements of optical response in irradiating a pulse light are widely used for study in fields such as photochemistry, photobiology, and photophysics since the study of flash photolysis by Porter et al. in 1949 [3.62]. This measurement method is called pump probe measurement or transient absorption spectroscopy (TAS). Over the years, many techniques have been proposed to obtain transient responses using various experimental systems, which are classified into two categories based on the form of probe light: CW probe method and pulse probe method [3.63]. First, the technique using a CW laser in probe light is pump CW probe method, which is generally called flash photolysis [3.64]. A schematic image of the typical system is shown in Fig. 3.13 (a). In this technique, transient responses by a pulsed laser are probed as the reflectivity or transmittivity changes by CW laser where the signal is analyzed by an oscilloscope. Therefore, this technique has an advantage of continuous measurements for irreversible phenomena such as ablation process and chemical reaction. The time resolution depends on the rise time of used photodetector or the resolution of used oscilloscope. As a result, the resolution is longer than few nanoseconds, and the technique does not enable observations of fast phenomena in the time scale shorter than a nanosecond. Second, the technique using a pulsed laser in probe light is pump pulse probe method, which is generally called pump probe method [3.65]. A schematic image of the typical system is also shown in Fig. 3.13 (b). In this technique, two pulsed light separated from one pulsed light irradiated by a pulsed laser with duration of picosecond or femtosecond are used as pump light to generate transient perturbation and as probe light to detect the transient response. An optical delay line is arranged in the light path of one pulse light and operates the arrival timing of the pump or probe light to the sample. Transient responses generated by the pulse light are probed as reflectivity or transmittivity change by convolution processing of the probe pulse light and the transient response.

The optical delay line, a lock-in amplifier, and a modulator such as mechanical chopper and acousto-optical modulator (AOM) are used to obtain the convolution signal. This technique has an advantage of observing fast phenomena in picosecond and femtosecond time scale. This is because the time resolution depends on the duration of the pulsed laser used. However, the technique does not enable measurements of phenomena with time length longer than few nanoseconds because the measurable time length is limited by the mechanical length of the optical delay line. In addition, the technique enables only measurements of reversible phenomena such as excited coherent phonon and transient thermoelastic stress because of duplicate measurements for obtaining the convolution signals.

The advantages and disadvantages of pump CW and pulse probe methods are summarized in Table 3.2. The representative applications are also written.

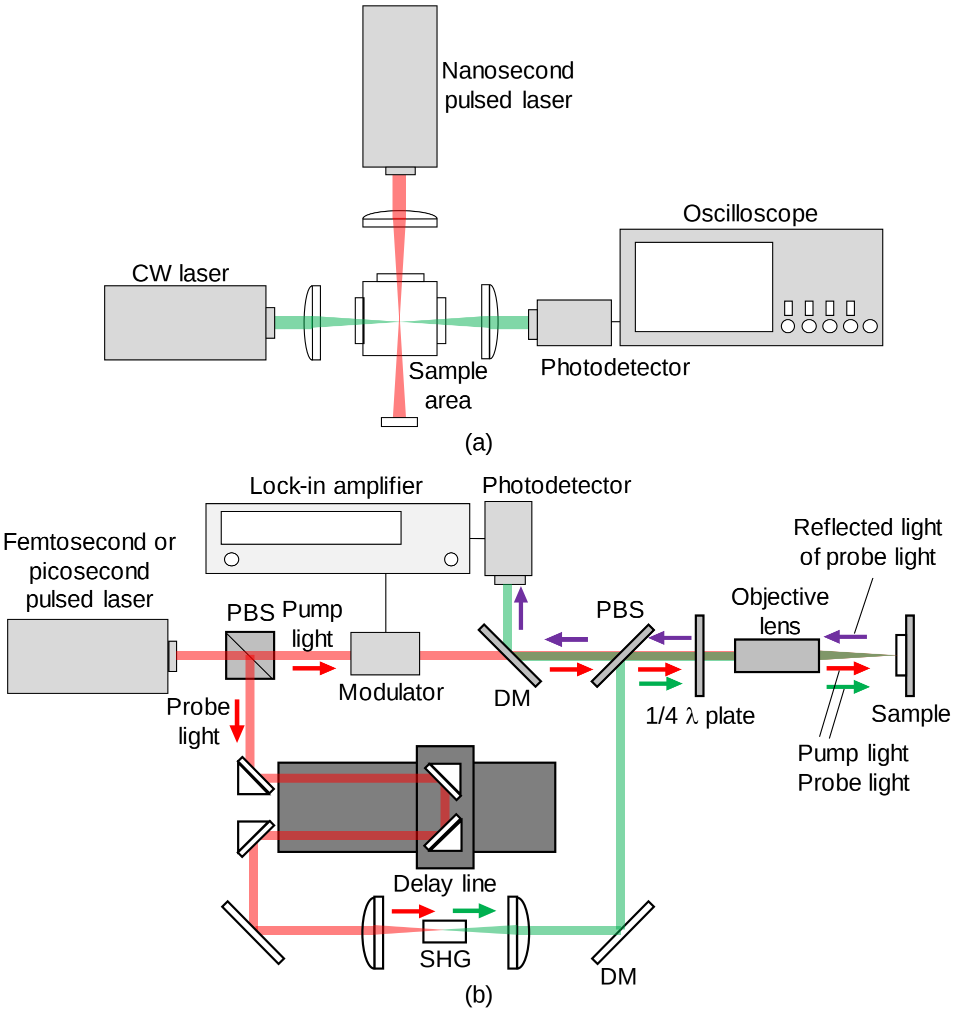

Fig. 3.13 Schematic images of typical (a) pump CW probe system (flash photolysis system) and (b) pump pulse probe system. SHG, DM, and PBS are second harmonic generator, dichroic mirror, and polarized beam splitter, respectively.

Table.3.2 Advantages and disadvantages of pump CW/pulse probe methods and their applications

Method	**Advantages**	**Disadvantages**	**Applications** [Ref.]
Pump pulse probe method	-High time resolution (A few fs) -High sensitivity -Observation of fast phenomena	-Short time measurement (Shorter than a few ns) -Limited in observation of reversible phenomena	Estimations of -thermal property [3.66, 3.67, 3.68] -Elastic property [3.69, 3.70, 3.71]
Pump CW probe method	-Actual time measurement -Long time measurement -Observation of irreversible phenomena	-Low time resolution (A few ns) -Low sensitivity	-Crack testing [3.72, 3.73] -Biological imaging [3.74]

3.3.2 PUMP PULSE PROBE METHOD

The pump pulse probe method is a spectroscopy technique which enables non-contact and non-destructive measurements of fast dynamic phenomena in time domain. This method is simply called pump probe method in this Subsection. In 1984, Thomsen et al. proposed that this method enables measurements of coherent phonons in film materials for the first time [3.69]. They demonstrated the observations of coherent phonons in As_2Te_3 amorphous film as transmittivity change of probe light. Moreover, they also reported measurements of surface acoustic waves generated by the irradiation of picosecond pulsed laser on the sample surface [3.75]. In 1986, by Paddock and Eesley, a pump probe measurement system with picosecond pulsed laser was first applied to measure the time scales of the electron cooling and electron–phonon coupling to study the thermal property of film materials [3.76]. After these studies, applications of this spectroscopy technique were extended into wide studies of elastic and thermal properties such as bulk acoustic velocity [3.65, 3.70], surface acoustic velocity [3.77], bulk modulus [3.71], acoustic attenuation [3.78], thermal diffusion coefficient [3.79], thermal conductivity [3.80, 3.81], interfacial thermal resistance [3.82, 3.68], and temperature characteristics of optical properties [3.83].

In pump probe method, the proper fitting model must be used to obtain the desired physical properties. For instance, a theoretical model based on elasticity formula and equation of motion is generally used to obtain elastic properties such as acoustic wave velocity and attenuation. In addition, theoretical model based on thermal conduction equation is generally used to obtain thermal properties such as thermal conductivity and thermal diffusion coefficient. Therefore, the combination of the measurement system and the fitting model based on proper theory is important for pump probe method.

3.3.3 PUMP PROBE MEASUREMENTS UNDER SPR

Few studies of pump probe measurements in SPR condition have been reported. Exter and Lagendijk fist demonstrated the observation of transient responses by pump probe method with a picosecond pulsed laser in SPR condition in 1988 [3.83]. They observed large transient responses due to temperature increase caused by the pump light irradiation. They also reported that the momentum lifetime of SPW is 48 fs and the propagation length is 13 μm in Ag metal film. In 1998, Katayama and Sawada observed large signals of surface acoustic wave by pump probe in

SPR condition [3.85]. In this report, surface acoustic waves were caused by the irradiation of two pump lights overlapping at the same area on Au film. The technique is especially called transient reflecting grating (TRG) method. The intensity of transient response was observed to be 100 times compared with the pump probe measurements without SPR. The observation of coherent phonons by pump probe method with a femtosecond pulsed laser under SPR condition was reported for the first time by Wang et al. [3.86]. In their studies, coherent phonons were observed by detecting the diffracted light due to the coherent phonons. This technique is especially called Brillouin oscillation method. They succeeded in the detection of coherent phonons with 11 times sensitivity by coupling with SPR. Moreover, Yamaguchi et al. attained the observations of not only the fundamental vibration but also the second, third, and fourth overtones of coherent phonons assigned to standing waves of longitudinal acoustic phonons in thin gold film [3.87].

As just described, high sensitivity observations of thermoelastic stress, surface acoustic wave, and coherent phonon by pump probe under SPR experimentally had been reported. However, the theoretical model for pump probe under SPR has not been reported yet. Therefore, pump probe under SPR were not yet applied for measurement of physical properties even though transient response can be obtained with high sensitivity. Pump probe technique under SPR has a potential to enable obtainment of optical, elastic, and thermal properties of metal film used in typical Kretschmann-type SPR sensor as a local, non-contact, and non-destructive method. Therefore, it is important to construct proper theoretical model of pump probe under SPR for its application as a measurement tool for SPR sensors.

REFERENCES

[3.1] AG. Bell, "On the production and reproduction of sound by light", Am. J. Sci. vol. 20, no. 3, pp. 305–324, Aug. 1880.

[3.2] J. Tyndall, "Action of an intermittent beam of radiant heat upon gaseous matter", Proc. R. Soc. Lond., vol. 31, pp. 307–317, 1881.

[3.3] W. C. Röntgen, "On tones produced by the intermittent irradiation of a gas", Phil. Mag., vol. 11, no. 5, pp. 308–311, 1881.

[3.4] K.F. Luft, "A new recording method of gas analysis by means of infrared absorption without spectral splitting", Z. Tech. Phys., vol. 24, pp. 97–104, 1943.

[3.5] W. R. Harshbarger and M. B. Robin, "The opto-acoustic effect: revival of an old technique for molecular spectroscopy", Acc. Chem. Res., vol. 6, pp. 329–334, 1973.

[3.6] A. Rosencwaig, "Photoacoustic spectroscopy of solids", Opt. Commun., vol. 7, pp. 305-308, 1973.

[3.7] L. V. Wang and S. Hu, "Photoacoustic tomography; In vivo imaging from organelles to organs", Science, vol. 335, no. 6075, pp. 1458–1462, Mar. 2012.

[3.8] H. F. Zhang, K. Maslov, L. V. Wang, "In vivo imaging of subcutaneous structures using functional photoacoustic microscopy", Nat. Protocols., vol. 2, no. 4, pp. 797–804, 2007.

[3.9] Y. Pu, R. Tang, J. Xue, W. B. Wang, B. Xu, and S. Achilefu, "Synthesis of dye conjugates to visualize the cancer cells using fluorescence microscopy", Appl. Opt., vol. 53, no. 11, pp. 2345–2351, Apr. 2014.

[3.10] A. M. Smith, M. C. Mancini, S. Nie, "Bioimaging: Second window for in vivo imaging", Nat. Nanotechnol., vol. 4 no. 11, pp.710–711, Nov. 2009.

[3.11] C. Kim, T. N. Erpelding, L. Jankovic, M. D. Pashley, L. V. Wang, "Deeply penetrating in vivo photoacoustic imaging using a clinical ultrasound array system", Biomed. Opt. Express, vol. 1, no. 1, pp. 278–284, July 2010.

[3.12] M. R. Chatni, J. Xia, R. Sohn, K. Guo, Y. Zhang, K. Wang, Y. Xia, M. Anastasio, J. Arbeit, and L. V. Wang, "Tumor glucose metabolism imaged in vivo in small animals with whole-body photoacoustic computed tomography", J. Biomed. Opt., vol. 17, no. 7, July 2012.

[3.13] L. Lin, J. Xia, T. T. W. Wong, L. Li, and L. V. Wang, "In vivo brain imaging of rats using oral-cavity illuminated photoacoustic computed tomography", J. Biomed. Opt., vol. 20, no. 1, Jan. 2015.

[3.14] K. Maslov, G. Stoica, and L. V. Wang, "In vivo dark-field reflection-mode photoacoustic microscopy", Opt. Lett., vol. 30, no.6, pp. 625–627, Mar. 2005.

[3.15] H. Zhang, K. Maslov, G. Stoica, and L. V. Wang, “Functional photoacoustic microscopy for high-resolution and noninvasive in vivo imaging”, Nat. Biotechnol., vol. 24, pp. 848–851, June 2006.

[3.16] K. Maslov, H. F. Zhang, S. Hu, and L. V. Wang, "Optical-resolution photoacoustic microscopy for in vivo imaging of single capillaries", Opt. Lett., vol. 33, no. 9, pp. 929–931, May 2008.

[3.17] V.E. Gusev and A.A. Karabutov, Laser optoacoustics (AIP Press, New York, 1993).

[3.18] M. Xu and L. V. Wang, "Photoacoustic imaging in biomedicine", Rev. Sci. Instrum., vol. 77, no. 041101, Feb. 2006.

[3.19] F. A. Duck, Physical Properties of Tissue (Academic, London, 1990)

[3.20] P. Beard, "Biomedical photoacoustic imaging", Interface Focus, vol. 1, pp. 602–631, May 2011.

[3.21] C. Li and L. V. Wang, "Photoacoustic tomography and sensing in biomedicine", Phys. Med. Biol., Vol. 54, pp. R59–R97, Sep. 2009.

[3.22] B. Lashkari and A. Mandelis, "Comparison between pulsed laser and frequency-domain photoacoustic modalities: Signal-to-noise ratio, contrast, resolution, and maximum depth detectivity", Rev. Sci. Instrum., vol. 82, no. 094903, Sep. 2011.

[3.23] F. Gao, R. Zhang, X. Feng, S. Liu, R. Ding, R. Kishor, L. Qiu, and Y. Zheng, "Phase-domain photoacoustic sensing", Appl. Phys. Lett., Vol. 110, no. 033701, Jan. 2017.

[3.24] F. Gao, X. Feng, and Y. Zheng, "Advanced photoacoustic and thermoacoustic sensing and imaging beyond pulsed absorption contrast" J. Opt., vol. 18, no. 074006, Mar. 2016.

[3.25] F. Gao, X. Feng, and Y. Zheng, "Photoacoustic elastic oscillation and characterization", Opto. Express, vol. 23, no. 16, pp. 20617–20628, 2015.

[3.26] J. Li, Z. Tang, Y. Xia, Y. Lou, and G. Li, "Cell viscoelastic characterization using photoacoustic measurement ", J. Appl. Phys., vol. 104, no. 034702, Apr. 2008.

[3.27] F. Gao, X. Feng, Y. Zheng, and C-D. Ohl, "Photoacoustic resonance spectroscopy for biological tissue characterization", J. Biomed. Opt., vol. 19, no. 067006, June 2014.

[3.28] C. Lou and D. Xing, "Photoacoustic measurement of liquid viscosity", Appl. Phys. Lett., vol. 96, no. 211102, Apr. 2010.

[3.29] Y. Zhao, S. Yang, C. Chen, and D. Xing,"Simultaneous optical absorption and viscoelasticity imaging based on photoacoustic lock-in measurement ", Opt. Lett., vol. 39, no. 9, pp. 2565–2568, Mar. 2014.

[3.30] G. Gao, S. Yang, and D. Xing, "Viscoelasticity imaging of biological tissues with phase-resolved photoacoustic measurement", Opt. Lett., vol. 36, no. 17, pp. 3341–3343, July 2011.

[3.31] L. Gao C. Zhang, C. Lia, and L. V. Wang, "Intracellular temperature mapping with fluorescence-assisted photoacoustic-thermometry", Appl. Phys. Lett., vol. 102, no. 193705, May 2013.

[3.32] W. Song, W. Liu, and H. F. Zhang, "Laser-scanning Doppler photoacoustic microscopy based on temporal correlation", Appl. Phys. Lett., vol. 102, no. 203501, May 2013.

[3.33] H. Fang, K. Maslov, and L. V. Wang, "Photoacoustic doppler effect from flowing small light-absorbing particles", Phys. Rev. Lett., vol. 99, no. 184501, Oct. 2007.

[3.34] Spec sheets of photoacoustic microscopy system produced by Micro Photo Acoustic inc.

[3.35] A. Danielli, K. Maslov, A. Garcia-Uribe, A. M. Winkler, C. Li, L. Wang, Y. Chen, G. W. Dorn II, and L. V. Wang, “Label-free photoacoustic nanoscopy”, J. Biomed. Opt., vol. 19, no. 8, Aug. 2014.

[3.36] L. Wang, C. Zhang, and L. V. Wang, “Grueneisen relaxation photoacoustic microscopy”, Phys. Rev. Lett., vol. 113, no. 17, Oct. 2014.

[3.37] T. Wang, R. Cao, B. Ning, A. J. Dixon, J. A. Hossack, A. L. Klibanov, Q. Zhou, A. Wang, and S. Hu, "All-optical photoacoustic microscopy based on plasmonic detection of broadband ultrasound" Appl. Phys. Lett., vol. 107, no. 153702, Oct. 2015.

[3.38] A. I. Morozov, Introduction to Plasma Dynamics (CRC Press, 2012).

[3.39] D. Bohm and D. Pines, " A collective description of electron interactions: I. Magnetic interactions", Phys. Rev., vol. 82, no. 5, pp. 625–634, June 1951.

[3.40] D. Pines and D. Bohm, " A collective description of electron interactions: II. Collective vs individual particle aspects of the interactions", Phys. Rev., vol. 85, no. 2, pp. 338–353, Jan. 1952.

[3.41] D. Bohm and D. Pines, " A collective description of electron interactions: III. Coulomb interactions in a degenerate electron gas", Phys. Rev., vol. 92, no. 2, pp. 609–625, Nov. 1953.

[3.42] R. H. Ritchie, “Plasma losses by fast electrons in thin films”, Phys. Rev., vol. 106, no. 5 pp. 874–881, June 1957.

[3.43] Y. Y. Teng and E. A. Stern, "Plasma radiation from metal grating surfaces", Phys. Rev. Lett., vol. 19, no. 9, pp. 511–514, Aug. 1967.

[3.44] A. Otto, "Excitation of nonradiative surface plasma waves in silver by the method of frustrated total reflection", Z. Physik., vol. 216, pp. 398–410, July 1968.

[3.45] W. H. Weber and G. W. Ford, "Optical electric-field enhancement at a metal surface arising from surface -plasmon excitation", Opt. Lett., vol. 6, no. 3, pp. 122–124, Dec. 1980.

[3.46] P. B. Johnson and R. W. Christy, “Optical constants of the noble metals”, Phys. Rev. B, vol. 6, no. 12, pp. 4370–4379, July 1972.

[3.47] H. Ehrenreich and H. R. Philipp, "Optical properties of Ag and Cu", Phys. Rev., vol. 128, no. 4, pp. 1622–1629, Nov. 1962.

[3.48] B. R. Cooper, H. Ehrenreich, and H. R. Philipp, "Optical properties of noble metals. II", Phys. Rev., Vol. 138, no. 2A, pp. 494–507, Apr. 1965.

[3.49] H. Ehrenreich, H. Philipp, and B. Segall, “Optical properties of aluminum”, Phys. Rev., vol. 132, nol. 5, pp. 1918–1928, Dec. 1963.

[3.50] R. LaVilla and H. Mendlowitz, "Optical constants of aluminum in vacuum ultraviolet", Phys. Rev. Lett., vol. 9, no. 4, pp. 149–150, Aug. 1962.

[3.51] K. M. McPeak, S. V. Jayanti, J. P. Kress, S. Meyer, S. Iotti, A. Rossinelli, and D. J. Norris, “Plasmonic films can easily be better; rules and recipes”, ACS Photonics, vol. 2, pp. 326–333, 2015.

[3.52] P. R. West, S. Ishii, G.V. Naik, N.K. Emani V.M. Shalaev, and A. Boltasseva, "Searching for better plasmonic materials", Laser Photonics Rev., vol. 4, no. 6, pp. 795–808, Jan. 2010.

[3.53] C. Nylander, B. Liedberg, and T. Lind, "Gas detection by means of surface plasmon resonance", Sensors and Actuators, vol. 3, pp. 79–88, 1982/83.

[3.54] B. Liedberg, C. Nylander, and I. Lunström, "Surface plasmon resonance for gas detection and biosensing", Sensors and Actuators, vol. 4, pp. 299–304, 1983.

[3.55] M. Niggemann, A. Katerkamp, M. Pellmann, P. Bolsmann, J. Reinbold, and K. Cammann, “Remote sensing of tetrachloroethene with a micro-fibre optical gas sensor based on surface plasmon resonance spectroscopy”, Sensors and Actuators vol. B34, pp.328–333, Mar. 1996.

[3.56] L. G. Fägerstam, Å. Frostell, R. Karlsson, M. Kullman, A. Larsson, M. Malmqvist, and H. Butt, “Detection of antigen—antibody interactions by surface plasmon resonance. Application to epitope mapping”, J. Molecular Recognition, vol. 3, pp. 208–218, Oct. 1990.

[3.57] A. Schilling, O. Yavas, J. Bischof, J. Boneberg, and P. Leiderer, “Absolute pressure measurements on a nanosecond time scale using surface plasmons,” Appl. Phys. Lett., vol. 69, no. 27, pp. 4159–4161, Oct. 1996.

[3.58] J. Boneberg, S. Briaudeau, Z. Demirplak, V. Dobler, and P. Leiderer, “Two-dimensional pressure measurements with nanosecond time resolution”, Appl. Phys. A, vol. 69, pp. S557–S560, Sep. 1999.

[3.59] R. Nuster, G. Paltauf, and P. Burgholzer, "Comparison of surface plasmon resonance devices for acoustic wave detection in liquid", Opt. Express, vol. 15, no. 10, Apr. 2007.

[3.60] V. V. Yakovlev, W. Dickson, A. Murphy, J. Mcphillips, R. J. Pollard, V. A. Podolskiy, and A. V. Zayats, "Ultrasensitive non-resonant detection of ultrasound with plasmonic metamaterials", Adv. Mater., vol. 25, pp. 2351–2356, Mar. 2013.

[3.61] A. A. Kolomenskii, E. Surovic, and H. A. Schuessler, "Optical detection of acoustic waves with surface plasmons", Appl. Opt., vol. 57, no. 20, pp. 5604–5613, June 2018.

[3.62] R. G. W. Norrish and G. Porter, "Chemical reactions produced by very high light intensities" Nature, vol. 164, no. 658, 1949.

[3.63] T. Nakagawa, K. Okamoto, H. Hanada, and R. Katoh, "Probing with randomly interleaved pulse train bridges the gap between ultrafast pump-probe and nanosecond flash photolysis", Opt. Lett., vol. 41, no. 7, pp. 1498–1501, Mar. 2016.

[3.64] G. Porter and M. R. Topp, "Nanosecond flash photolysis and the absorption spectra of excited singlet", Nature, vol. 220, pp. 1228–1229, 1968.

[3.65] P. Ruello and V. E. Gusev, “Physical mechanisms of coherent acoustic phonons generation by ultrafast laser action”, Ultrasonics, vol. 56, pp. 21–35, June 2014.

[3.66] P. M. Norris, A. P. Caffrey, R. J. Stevens, J. M. Klopf, J. T. McLeskey, and A. N. Smith, “Femtosecond pump–probe nondestructive examination of materials (invited)”, Rev. Sci. Instrum., vol. 74, no. 1, pp. 400–406, Jan. 2003.

[3.67] A. J. Schmidt, X. Chen, and G. Chen, “Pulse accumulation, radial heat conduction, and anisotropic thermal conductivity in pump-probe transient thermoreflectance”, Rev. Sci. Instrum., vol. 79, no. 114902, Oct. 2008.

[3.68] A. N. Smith, J. L. Hostetler, and P. M. Norris, “Thermal boundary resistance measurements using a transient thermoreflectance technique”, Micro. Thermophys. Eng., vol. 4, pp. 51–60, Nov. 1999.

[3.69] C. Thomsen, J. Strait, Z. Vardeny, H. J. Maris, and J. Tauc, "Coherent phonon generation and detection by picosecond light pulses", Phys. Rev. Lett., vol. 53, no. 10, pp. 989–992, Sep. 1984.

[3.70] B. C. Daly, T. B. Norris, J. Chen, and J. B. Khurgin, “Picosecond acoustic phonon pulse propagation in silicon”, Phys. Rev. B, vol. 70, no. 214307, Dec. 2004.

[3.71] H. Ogi, T. Shagawa, N. Nakamura, and M. Hirao, H. Odaka, and N. Kihara, “Elastic constant and Brillouin oscillations in sputtered vitreous SiO_2 thin films”, Phys. Rev. B, vol. 78, no. 134204, Oct. 2008.

[3.72] A. Moura, A. M. Lomonosov, and P. Hess, “Depth evaluation of surface-breaking cracks using laser-generated transmitted Rayleigh waves”, J. Appl. Phys., vol. 103, no. 084911, Mar. 2008.

[3.73] J. Li, L. Dong, C. Ni, Z. Shen, and H. Zhang, “Application of ultrasonic surface waves in the detection of microcracks using the scanning heating laser source technique”, C. Opt. Lett., vol. 10, no. 11, Nov. 2012.

[3.74] B. Dong, C. Sun, and H. Zhang, “Optical detection of ultrasound in photoacoustic imaging”, IEEE Trans. Biomed. Eng., vol. 64, no. 1, Jan. 2017.

[3.75] C. Thomsen, H. T. Grahn, H. J. Maris, and J. Tauc, “Surface generation and detection of phonons by picosecond light pulses”, Phys. Rev. B, vol. 34, no. 6, Sep. 1986.

[3.76] C.A. Paddock and G.L. Eesley, "Transient thermoreflectance from thin metal-films", J. Appl. Phys., Vol. 60, No. 1, pp. 285–290, Mar. 1986.

[3.77] O. B. Wright and K. Kawashima, “Coherent phonon detection from ultrafast surface vibrations”, Phys. Rev. Lett., vol. 69, no. 11, pp. 1668–1671, Sep. 1992.

[3.78] T. C. Zhu, H. J.Maris, and J.Tauc, “Attenuation of longitudinal-acoustic phonons in amorphous Si02 at frequencies up to 440 GHz”, Phys. Rev. B, vol. 44, no. 9, Sep. 1991.

[3.79] S. Wu, S-Y. Zhang, H-X. Sun, “Thermal diffusivities of bilayer films deposited on substrates characterized simultaneously by transient reflecting grating technique”, Int. Thermophys., vol. 34, pp. 1579–1584, Oct. 2012.

[3.80] G. L. Eesley, “Observation of nonequilibrium electron heating in copper”, Phys. Rev. Lett., vol. 51, pp. 2140–2143, Dec. 1983.

[3.81] C. A. Paddock and G. L. Eesley, “Transient thermoreflectance from thin metal films”, J. Appl. Phys., vol. 60, no. 285, Mar. 1986.

[3.82] R. J. Stoner and H. J. Maris, “Kapitza conductance and heat flow between solids at temperatures from 50 to 300 K”, Phys. Rev. B, vol. 48, no. 22, pp. 16373–16387, Dec. 1993.

[3.83] D. T. Owens, C. Fuentes-Hernandez, J. M. Hales, J. W. Perry, and B. Kippelen, "A comprehensive analysis of the contributions to the nonlinear optical properties of thin Ag films", J. Appl. Phys., vol. 107, no. 123114, Apr. 2010.

[3.84] M. V. Exter and A. Lagendijk, “Ultrashort surface-plasmon and phonon dynamics”, Phys. Rev. Lett., vol. 60, no. 1, pp. 49–52, Jan. 1988.

[3.85] K. Katayama, T. Sawada, Q. Shen, and A. Harata, "Detection of photoinduced electronic, thermal, and acoustic dynamics of gold film using a transient reflecting grating method under three types of surface plasmon resonance conditions", Phys. Rev. B, vol. 58, no. 13, Apr. 1998.

[3.86] J. Wang, J. Wu, and C. Guo, "Resolving dynamics of acoustic phonons by surface plasmons", Opt. Lett., vol. 32, no. 6, pp. 719–721, Dec. 2006.

[3.87] S. Yamaguchi and T. Tahara, “Coherent acoustic phonons in a thin gold film probed by femtosecond surface plasmon resonance”, J. Raman Spectrosc., vol. 39, pp. 1703–1706, July 2008.

4. DEVELOPMENT OF SUB-NANOSECOND PUMP PROBE SYSTEM

Pump probe technique is a time-resolved spectroscopy technique. In this technique, photothermal elastic response induced by irradiation of pump light is observed as an optical reflectivity change. The reflectivity change is measured by probe light, as a convolution signal of the thermoelastic response and the pulsed probe light. Therefore, the pulse duration of the pulsed laser used affects the measured responses of the reflectivity change. As a result, expensive femtosecond Ti-sapphire pulsed lasers are often preferred for pump probe systems [4.1, 4.2, 4.3]. However, there are only few studies on pump probe response with sub-nanosecond pulsed laser systems despite the fact that the characteristics of transient response in the sub-nanosecond time region is important for materials used in SPR ultrasonic sensors for high-resolution PAM systems [4.4, 4.5]. Therefore, it is first necessary to develop a pump probe system with sub-nanosecond pulsed laser before conducting studies on sub-nanosecond pump probe under SPR. The objective of this chapter is to introduce the developed pump probe system with sub-nanosecond pulsed laser. In Section 4.1, the configuration of the developed sub-nanosecond pump probe system is explained. In addition, the observation results of transient response by this system are shown in Section 4.2.

4.1 CONFIGURATION OF THE DEVELOPED SUB-NANOSECOND PUMP PROBE SYSTEM

The developed sub-nanosecond pump probe measurement system is shown in Fig. 4.1. The configuration and the functions of the system are explained below.

In the system developed, a sub-nanosecond pulsed laser with pulse duration of 640 ps and wavelength of 1064 nm (Herios 1064-5-50, Coherent Inc., Santa Clara, CA) was used. The pulsed laser was irradiated by the sub-nanosecond pulsed laser with a specific repetition frequency. Laser light was separated into pump light with s-polarization and probe light with p-polarization by a polarized beam splitter (PBS). The optical power ratio of the pump light to the probe light was adjusted using a polarization variable attenuator composed of a PBS and a ½-λ plate. The function of the polarization variable attenuator is described in Subsection 4.1.1.

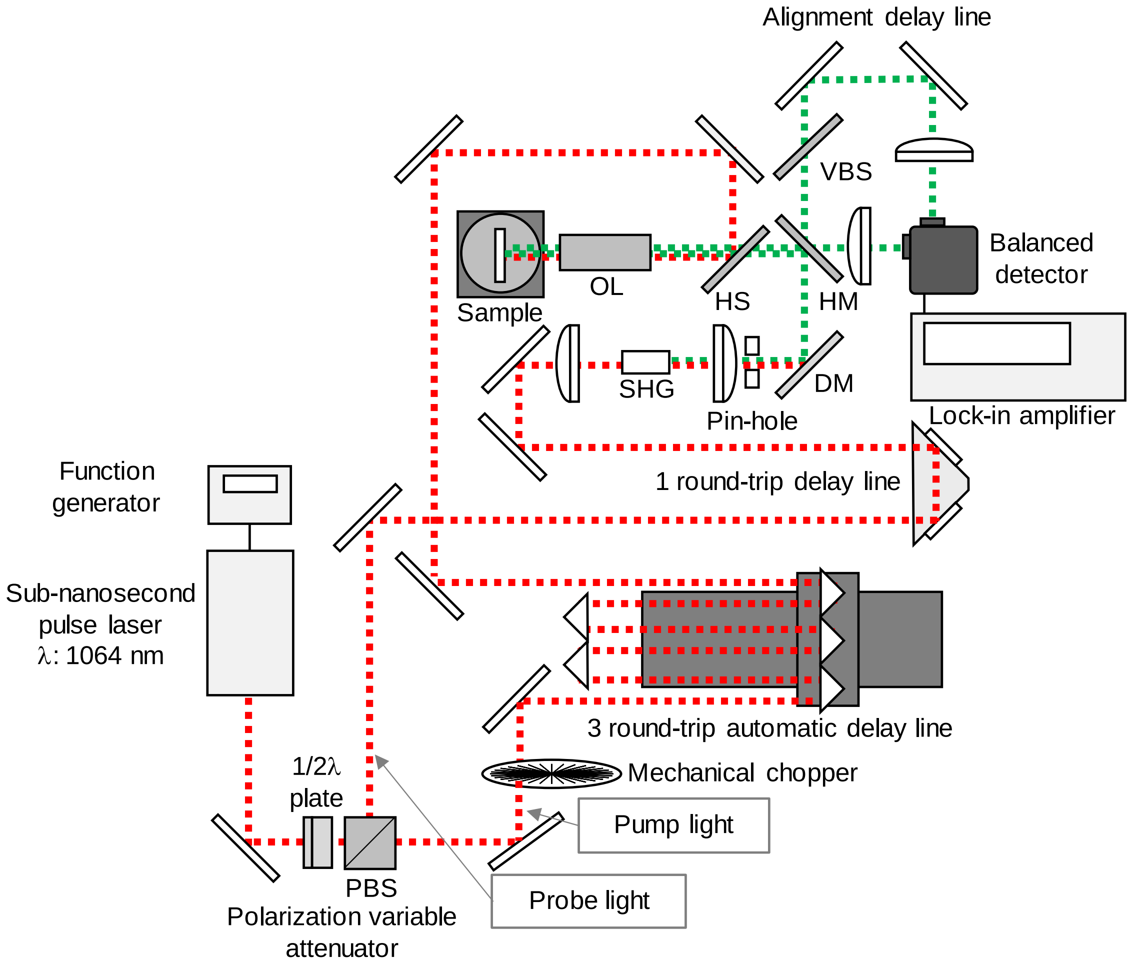

Fig. 4.1 Developed sub-nanosecond pump probe system with coaxial focusing of the pump and probe lights.

PBS: Polarization beam splitter,	SHG: Second harmonic generator,
DM: Dichroic mirror,	HM: Half mirror,
HS: Harmonic separator,	VBS: Variable beam splitter
OL: Objective lens.	

The intensity of the pump light was modulated using a mechanical light chopper (5584A, NF Corp., Kanagawa, Japan). This modulation is necessary for the lock-in measurement. In this system, the sweep time was controlled by delaying the pump light with a three-round-trip automatic delay line. The long-time measurement of 10 ns is attained by the delay line. The construction and function of the delay line are described in Subsection 4.1.2. The arrival time of the probe light was also fine-adjusted using a manual one-round trip delay line. The wavelength of the probe light was converted to 532 nm by second harmonic generation (SHG) with a LiB_3O_5

(LBO) crystal (LBO-402, Eksma Optics, Vilnius, Lithuania). As a result, the pump and probe lights were distinguishable based on their unique wavelengths. The mechanism of the SHG is described in Subsection 4.1.3. The scattering light from the SHG were eliminated by a pinhole. The transmitted light with a wavelength of 1064 nm was filtered by a dichroic mirror (DM). The converted light was then separated into the probe light and the reference light by a half mirror (HM). The reference light is necessary for the sensitive differential detection system with a balanced detector (1607-AC-FS, Newport Corp., Irvine, California). The function of the differential detection system is described in Subsection 4.1.4. The probe and pump lights were coupled by a harmonic separator (HS) and were coaxially focused on the surface of the measurement sample using an objective lens (OL) with a focal length of 20 mm (PAL-20-NIR-HR-LC00, Sigma Koki Co., Ltd., Saitama, Japan). The pump and probe lights were irradiated in the same area of the sample because of the coaxial focusing. The reflected light of the probe light passed through the same optical path and entered the balanced detector. The arrival timing of the reference light was fine-adjusted to the same timing of the reflected probe light using a one-round trip delay line. The intensity of the reference light was adjusted to the same intensity of the reflected probe light using a variable beam splitter (VBS). Reflectivity changes due to the pump light irradiation were obtained by measuring the differential signals using a differential detection system and a lock-in amplifier (LI5660, NF Corp., Kanagawa, Japan). The mechanism of the lock-in measurement is described in Subsection 4.1.5.

4.1.1 POLARIZATION VARIABLE ATTENUATOR

Many techniques have been suggested to vary the light intensity. One of the famous techniques is a method using a neutral density (ND) filter. It enables attenuation of the intensity of the transmitted light by light absorber contained in that. Especially, there are two types of ND filter: fixed type and variable type. However, the fixed type ND filter only enables the variation of light intensity discretely. The variable type one, also, has a problem in the sense that the gradation of the absorber concentration affects the distribution of the transmitted light intensity. However, it is known that the technique using a variable beam splitter (VBS) can attain the continuous adjustment of the light intensity. This technique operates such that the transmittivity of VBS is a function of the incident angle. However, the optical path of the transmitted light through VBS changes due to refraction depending on the incident angle. Because of it, this technique is not suitable for a fixed optical system. Here, polarization variable attenuator can be used in the fixed system to vary the light intensities continuously. This technique was adopted in the developed sub-nanosecond pump probe system to adjust the ratio of the intensities of the pump and probe lights. The schematic image is shown in Fig. 4.2. The polarization variable attenuator is composed of a ½-λ plate and a PBS. The light with s-polarization is reflected on the PBS. On the other hand, the one with p-polarization transmits through the PBS. Utilizing these characteristics of PBS, the ratio of the reflected and transmitted lights was controlled by changing the optical polarization of the incident light with a ½-λ plate arranged in front of the PBS. The transmitted light with p-polarization was used as a pump light and the reflected light with s-polarization was used as a probe light. The ratio of the reflected and transmitted lights controlled by the system is shown in Fig. 4.3.

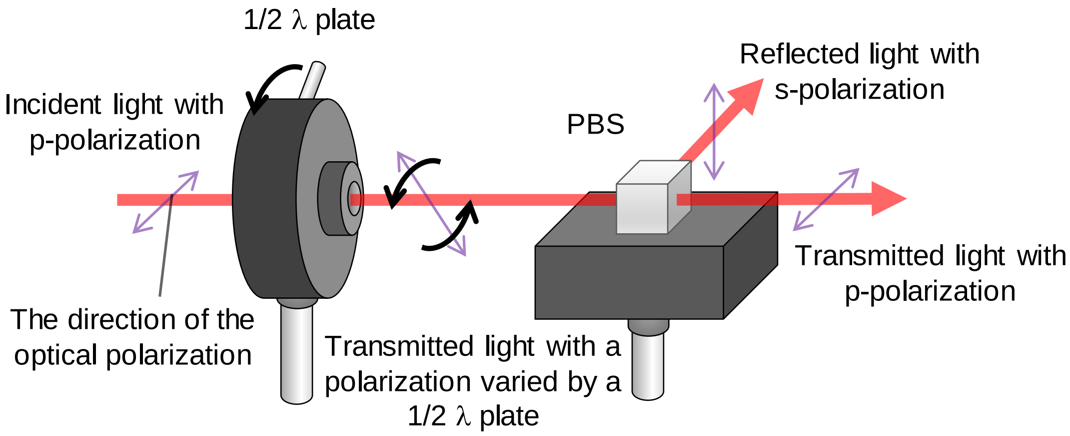

Fig. 4.2 Conceptual image of the function of polarization variable attenuator comprised of a ½-λ plate and a PBS.

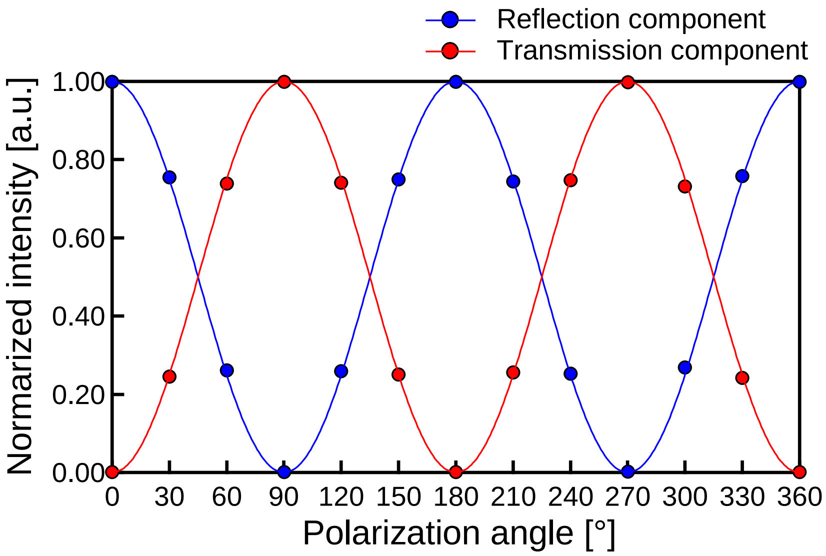

Fig. 4.3 Normalized light intensities of the reflection and transmission components of the polarization variable attenuator. Plots are measured data. The areas between the plots are complemented by a fitting curve of sine wave.

4.1.2 THREE ROUND-TRIP AUTOMATIC DELAY LINE

The arrival time of the pump or probe light needs to be swept in obtaining the pump probe response with time scale. In general, the sweep of time is attained by using a mechanical delay line. A technique to attain the time delay using two pulsed lasers without a mechanical delay line had also been reported [4.6]. However, the system was very expensive because the equipment had two pulsed lasers. Sweep time longer than several nanoseconds is necessary for sub-nanosecond pump probe system because the transient responses with time scale of nanoseconds are induced by irradiating the pump light with duration of sub-nanoseconds. The structure of the automatic delay line used in the system developed is shown in Fig. 4.4. Five retroreflectors and an automatic stage with a stepping motor were used in this system. The light reflected on the retroreflector travels parallel to the incident light as shown in Fig. 4.5 (a). By utilizing this characteristic of the retroreflector, the round-trip delay line can easily be assembled. In the system developed, the operation with optical length of 3.0 m was attained by three round-trip reflections using these five retroreflectors, which enabled long-time delay of 10 ns.

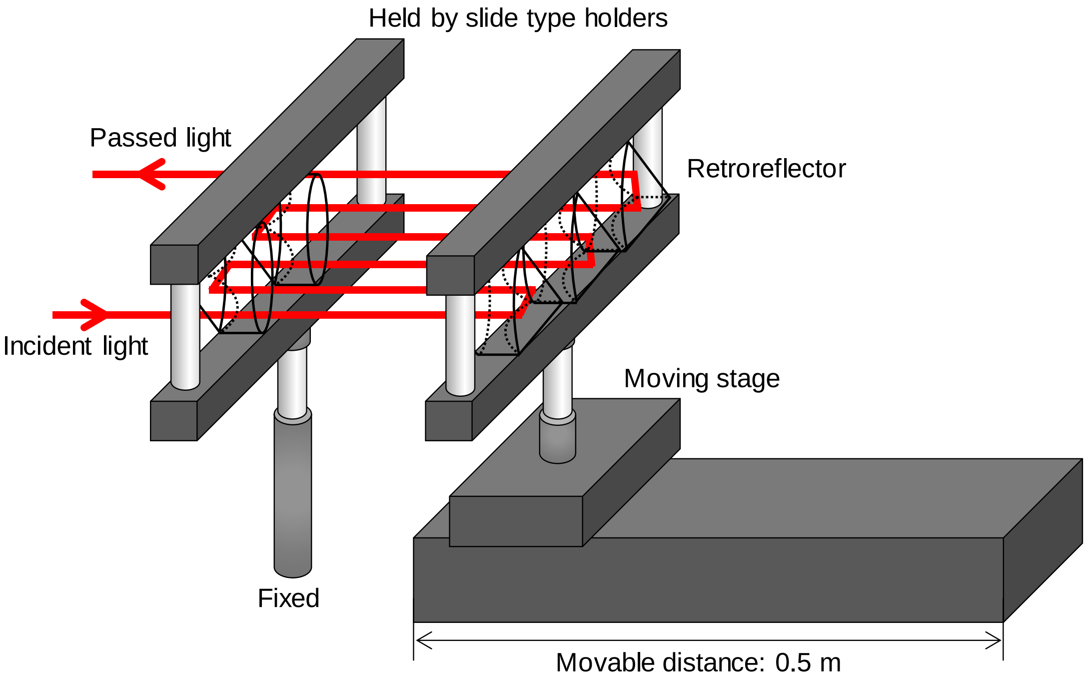

Fig. 4.4 Schematic image of the three round-trip automatic delay line composed of five retroreflectors and an automatic moving stage.

Retroreflector has a characteristic to change the polarization of the light. Thus, it is important to understand the polarization characteristic. If the incident light with linear polarization hits the surface of the retroreflector in normal direction, the light is reflected on each reflection surface with incident angle of 55°. Thus, the polarization of the reflected light changes due to the different phase delays, which depends on the direction of the polarization [4.7]. Polarization directions of the reflected light for an incident light with p-polarization to each reflection surface are shown in Fig. 4.5 (b). As can be seen in Fig. 4.5 (b), the polarization direction of the reflected light becomes elliptical polarization. The polarization of the pump light changed to a circular polarization state because the light is reflected on five retroreflectors. The polarization of the pump light after passing through the three round-trip automatic delay line is shown in Fig. 4.6.

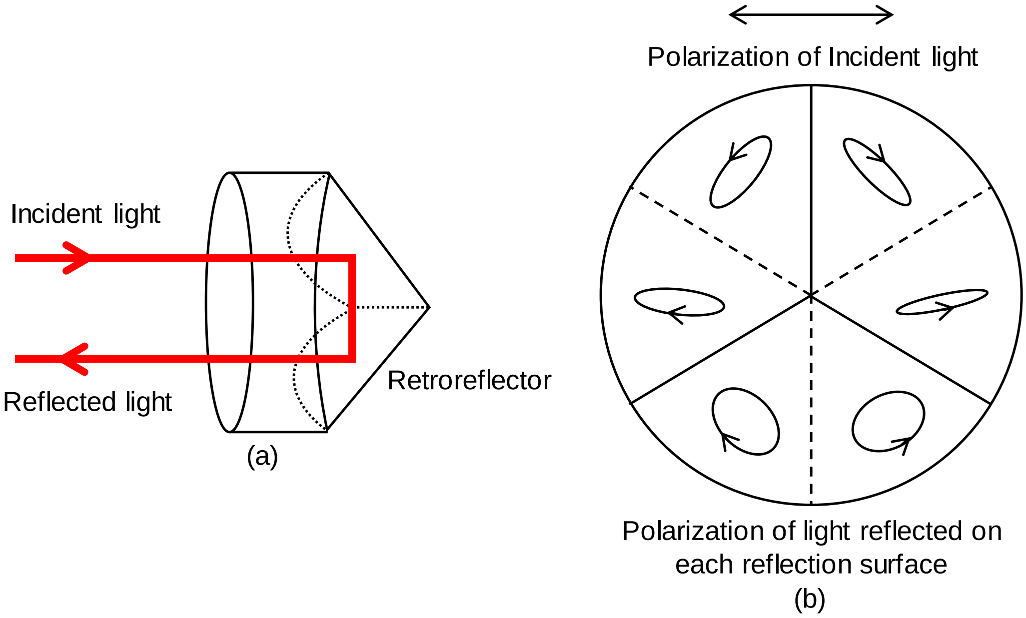

Fig. 4.5 (a) Schematic image of the retroreflector. (b) The polarization directions of the reflected light for an incident light to each reflection surface [4.7].

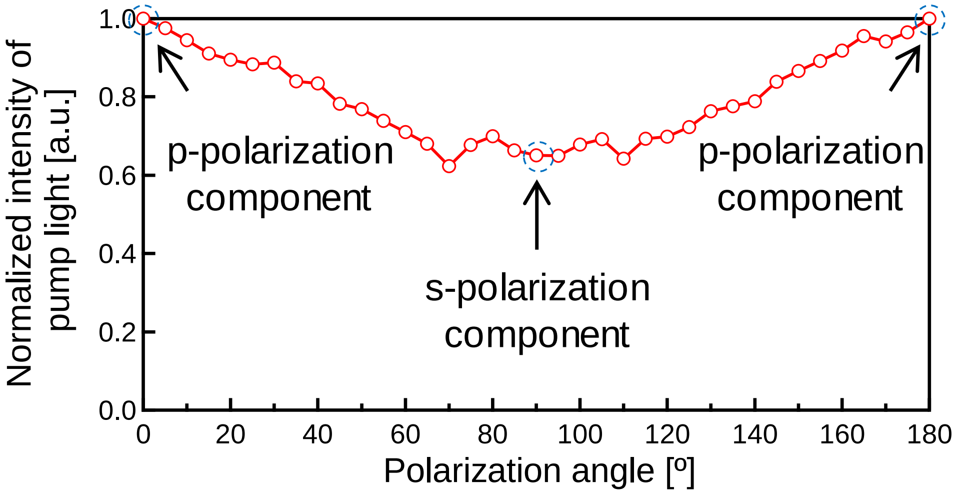

Fig. 4.6 Polarization of the pump light after passing through the three round-trip automatic delay line.

4.1.3 SECOND HARMONIC GENERATOR

In a pump probe method, it is necessary to distinguish clearly between the pump light and the probe light because the pump light must not enter the optical path of the probe light for precise measurement with low noise. Generally, light with different wavelength from that of the probe light is used as the pump light. In the case of a system with one pulsed laser, the wavelength of the pump or probe light must be converted by a non-linear optical crystal such as a second harmonic generator (SHG) to distinguish these lights. The mechanism of wavelength conversion by SHG is explained below.

A non-linear optical crystal has birefringence because of its uniaxial structure. When light hits a non-linear optical crystal, the dielectric polarizations with high-order term are generated due to the electric field of the light. Thus, the generated polarization P is written like below [4.8]:

$$P = \sum_{j=1}^{\infty} \chi^{(j)} S_{\mathrm{i}}^{j} \tag{4.1}$$

where, j is the order, $\chi^{(j)}$ is the non-linear optical coefficient in the order of j and S_{i} is the electric field of the incident light. The phases of fundamental wave and second harmonic wave must match for the continuous conversion of the wave to second harmonic wave. A conceptual image of the relationship between the incident angle and the refractive index is shown in Fig. 4.7. n_{o} and n_{e} are the refractive indices of ordinary ray and extraordinary ray, respectively. n^{ω} and $n^{2\omega}$ are the refractive indices for fundamental wave and second harmonic wave, respectively. θ_{pm} is the phase matching angle. As can be seen in Fig. 4.7, the refractive indices for the fundamental wave and the second harmonic wave match at incident angle of θ_{pm}, which is written below [4.8]:

$$n^{2\omega}(\theta_i) = n_{\mathrm{o}}^{\omega} \tag{4.2}$$

As a result, the phase velocities of both waves match at the phase matching angle. Therefore, cut surface of SHG crystal needs to be optimized such that the phase matching angle is met when an incident light strikes the crystal surface normally.

In the system developed, a LBO crystal ($3 \times 3 \times 15$ mm^3) was used as a SHG, which is suitable for the conversion of the laser with wavelength of 1064 nm to that with 532 nm [4.9]. The conversion efficiency of SHG is inversely proportional to the beam size passing through the SHG crystal. Therefore, when the light passed through the SHG, it was focused by a focus lens with a focal length of 400 mm.

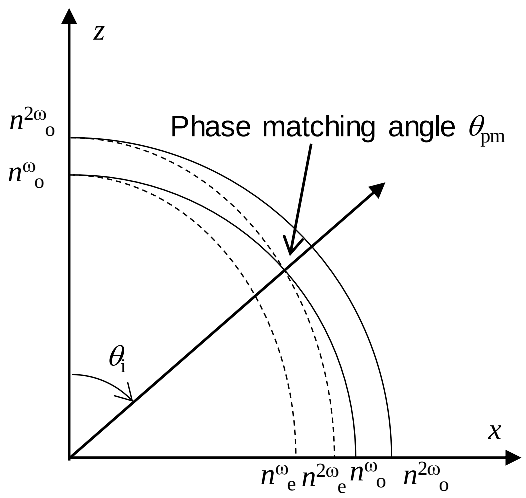

Fig. 4.7 The conceptual image of the relationship between the incident angle of the laser and the refractive indices. n_o and n_e are the refractive indices of ordinary ray and extraordinary ray, respectively. n^{ω} and $n^{2\omega}$ are the refractive indices for fundamental wave and second harmonic wave, respectively. θ_i is the angle between the incident light and the crystal axis. θ_{pm} is the phase matching angle.

4.1.4 DIFFERENTIAL DETECTION SYSTEM

Signal intensity obtained by the probe light is very weak in pump probe method. Therefore, the detection technique with high signal to noise (S/N) ratio is important in performing pump probe measurement with high sensitivity. In the system developed, differential detection technique with a balanced detector (1607-AC-FS, Newport Corp., Irvine, California) was used for high S/N ratio. Functional block diagram of the balanced detector used is shown in Fig. 4.8 (referred from the specification sheet). In obtaining the differential signal, the reflected probe light and the reference light were entered to two silicon photodiodes of PD_1 and PD_2, respectively. In the system, the repetition frequency of the pulse light source was controlled under 15 kHz because the band width of the output was limited under 15 kHz. In advance, the intensity and the arrival time of the reference light were adjusted to be the same with those of the probe light using a VBS and an alignment delay line. As shown in Fig. 4.9, the background intensities in output $V_2 - V_1$, such as light powers and noises, became too low through these alignments while the desired signal intensity did not change. As a result, the measurement with high S/N ratio was attained.

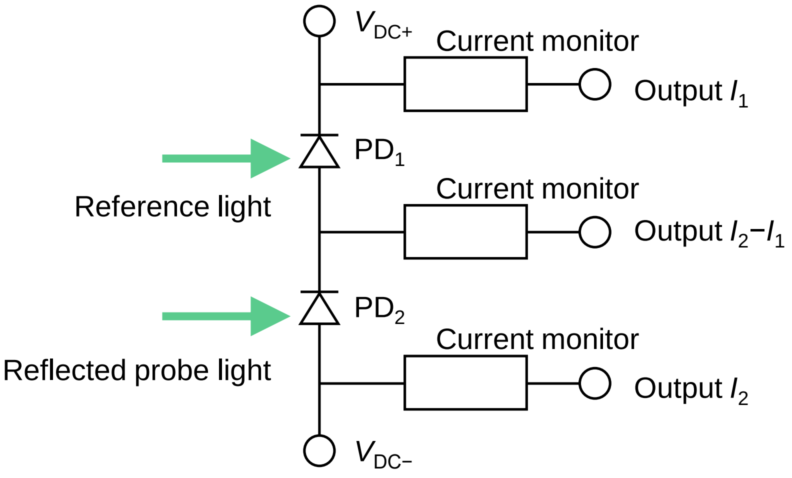

Fig. 4.8 Functional block diagram of the balanced detector used (1607-AC-FS, Newport Corp., Irvine, California) in the pump probe system developed. This block diagram is referred from the specification sheet. V_{DC} is the direct voltage. I_1 and I_2 are the output currents.

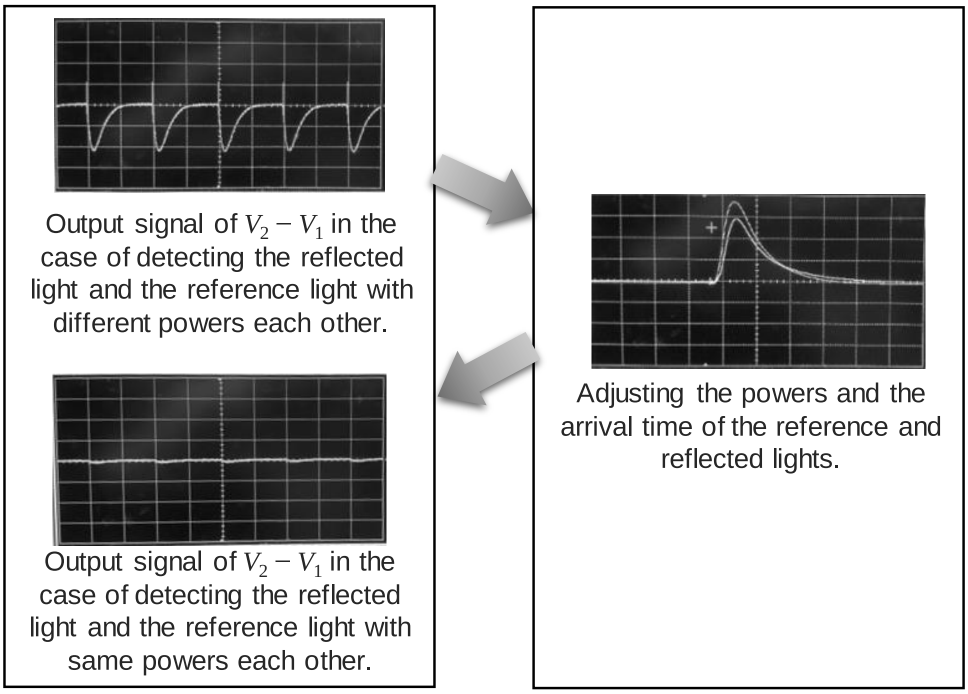

Output signal of $V_2 - V_1$ displayed on an oscilloscope

Output signals of V_2 and V_1 displayed on an oscilloscope

Fig. 4.9 Alignment process of the powers of the reflected probe light and the reference light in attaining the differential detection with high S/N ratio.

4.1.5 LOCK-IN MEASUREMENT

Lock-in measurement is a powerful tool to measure the amplitude of a signal with low S/N ratio. Thus, this technique is often used in pump probe measurements. Figure 4.10 shows a circuit diagram of a lock-in amplifier. In the system developed, a lock-in amplifier equipped with binary phase shift keying (BPSK) was used. Here, measurement mechanism of the lock-in amplifier with BPSK is explained below.

The input voltage $V_t(t)$ to the lock-in amplifier with temporal dimension is written below based on the inverse Fourier transform.

$$V_t(t) = \int_{\omega=-\infty}^{\omega=\infty} V_\omega(\omega) \cos\{\omega t + \phi(\omega)\}\, d\omega \tag{4.3}$$

where, ω is the angular frequency, V_ω is the amplitude of the input voltage with frequency dimension, and ϕ is the phase of each frequency components. The reference signal $V_{\mathrm{r1}}(t)$ is also given below.

$$V_{\mathrm{r1}}(t) = \cos(\omega_{\mathrm{r}} t) \tag{4.4}$$

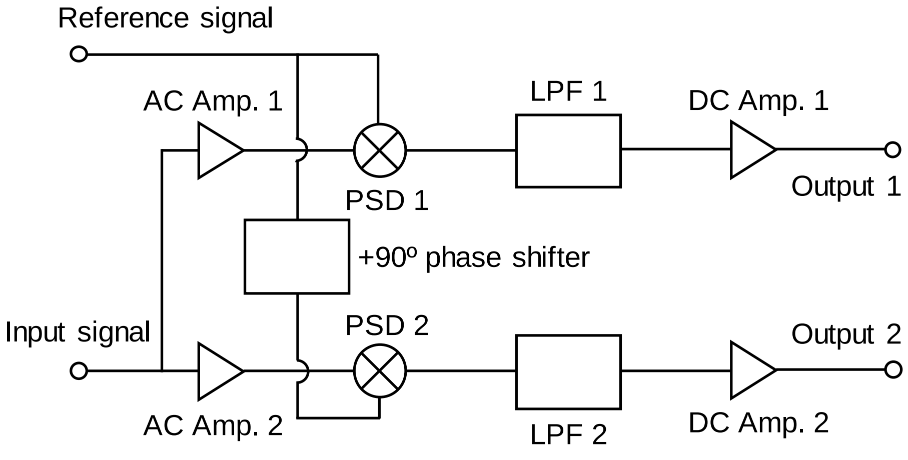

Fig. 4.10 Circuit diagram of a lock-in amplifier.
Amp.: Amplifier, PSD: Phase sensitive detector,
LPF: Low pass filter.

where, ω_r is the angular frequency of the reference signal, which indicates the desired frequency component. The reference signal is inputted to a phase sensitive detector (PSD) 1. In addition, the reference signal is also inputted to a PSD 2 after making a phase shift of 90°. Considering the phase shift, the reference signal $V_\mathrm{r2}(t)$ is written as below.

$$V_\mathrm{r2}(t) = \sin\,(\omega_\mathrm{r} t) \tag{4.5}$$

The reference signals $V_\mathrm{r1}(t)$ and $V_\mathrm{r2}(t)$ are mixed with the input signal by PSD 1 and PSD 2, respectively. The mixed signals are written as below:

$$V_t(t)V_\mathrm{r1}(t) = \int_{\omega=-\infty}^{\omega=\infty} \frac{V_\omega(\omega)}{2} [\cos\{(\omega - \omega_\mathrm{r})t + \phi(\omega)\} + \cos\{(\omega + \omega_\mathrm{r})t + \phi(\omega)\}]\, d\omega \tag{4.6}$$

$$V_t(t)V_\mathrm{r2}(t) = \int_{\omega=-\infty}^{\omega=\infty} \frac{V_\omega(\omega)}{2} [-\sin\{(\omega - \omega_\mathrm{r})t + \phi(\omega)\} + \sin\{(\omega + \omega_\mathrm{r})t + \phi(\omega)\}]\, d\omega \tag{4.7}$$

The direct components only pass through the outputs 1 and 2 by a low pass filter (LPF). As a result, the outputs 1 and 2 are described below.

$$\mathrm{Output\ 1} = \frac{V_\omega(\omega_\mathrm{r})}{2} \cos\{\phi(\omega_\mathrm{r})\} \tag{4.8}$$

$$\mathrm{Output\ 2} = \frac{V_\omega(\omega_\mathrm{r})}{2} \sin\{\phi(\omega_\mathrm{r})\} \tag{4.9}$$

Finally, the amplitude of the detected signal is obtained by the sum of square of outputs 1 and 2 described above, as expressed below.

$$2\sqrt{(\mathrm{Output\ 1})^2 + (\mathrm{Output\ 2})^2} = V_\omega(\omega_\mathrm{r}) \tag{4.10}$$

Therefore, the amplitude of the signal with the desired frequency component can be determined by lock-in measurement because the lock-in amplifier acts as a band pass filter (BPF) with selective narrow band. In the system developed, the intensity of the pump light was modulated by a mechanical chopper. Therefore, the response induced by the pump light includes the frequency component of the mechanical chopping. The lock-in measurement enabled the amplitude measurement of the response by using the modulating signal as a reference signal.

4.2 TRANSIENT RESPONSE OBSERVED BY THE SUB-NANOSECOND PUMP PROBE SYSTEM

A demonstration was conducted using a typical film sample to confirm if the response due to the thermoelastic stress can be observed by the system developed. In this demonstration, a Au (100nm) / Cr (20nm) bimetal film was used as a measurement sample because it is often used as a base material for thin film devices [4.10]. A schematic image of the sample is shown in Fig. 4.11. These metal films were deposited on a silica glass plate using an electron-beam deposition apparatus.

In the demonstration, the pump and probe lights were irradiated to the surface of the film material. The repetition frequency of the pulsed laser was 6.0 kHz controlled by a function generator. The irradiated laser energy of the pump light was around 6 μJ and the energy of the probe light was 0.01-times less compared with that of the pump light. Their spot diameters were around 5 μm, which was measured through knife edge method.

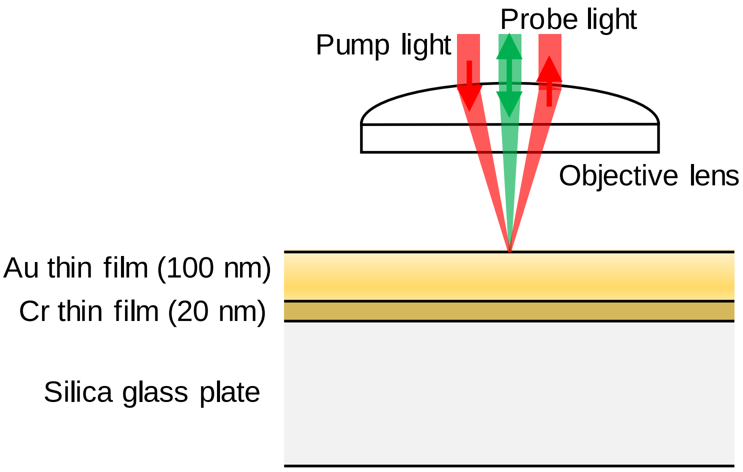

Fig. 4.11 Schematic image of the Au/Cr bimetal film sample.

The obtained signal is shown in Fig. 4.12. This signal is assumed to be the response due to thermoelastic effect because the ablation was not caused at the sample surface during experiment. As a reference of the signal wave form, the simulation result of temperature increase at the surface of Au metal film is shown in Fig. 4.13. This estimation was simply calculated considering a Au metal film with enough thickness [4.11]. As can be seen in Figs. 4.12 and 4.13, it is confirmed that the obtained thermoelastic signal was due to the temperature increase because the signal intensity increased simultaneously with the increase in temperature. Note that the tendency of temperature decrease due to heat conduction is not helpful in the simple simulation because the thickness of the Ag metal film and the existences of a Cr bottom film and a glass plate were not considered. The thermal relaxation time almost depends on the structure considering them. However, the simultaneous increase of the observed signal with the calculated temperature increase implies that a transient signal caused by the irradiation of the pump light can be observed using the measurement system developed in spite of the large noise.

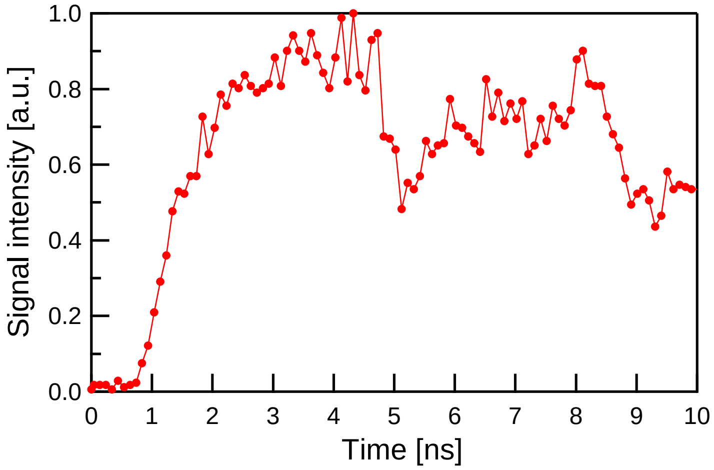

Fig. 4.12 The obtained thermoelastic response as a reflectivity change at a surface of Au (100 nm) /Cr (20 nm) bimetal film deposited on a Silica glass plate.

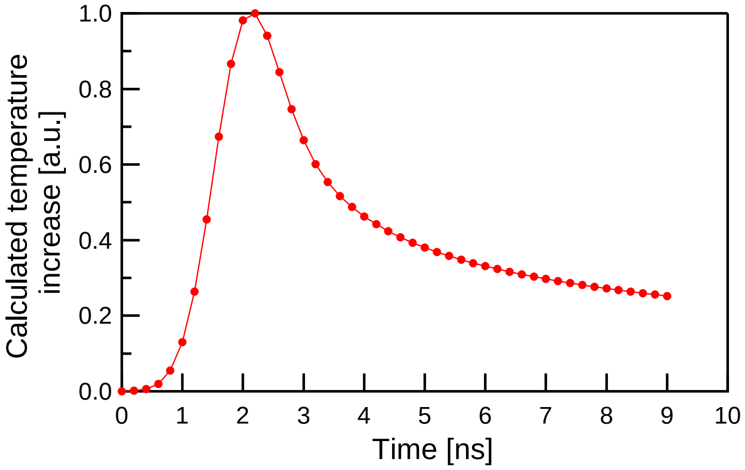

Fig. 4.13 Estimation result of the temperature increase at the surface of Au metal film. This data is calculated considering a gold film with enough thickness.

REFERENCES

[4.1] C. Thomsen, J. Strait, Z. Vardeny, H. J. Maris, and J. Tauc, "Coherent phonon generation and detection by picosecond light pulses", Phys. Rev. Lett., vol. 53, no. 10, pp. 989−992, Sep. 1984.

[4.2] C. Thomsen, H. T. Grahn, H. J. Maris, and J. Tauc, “Surface generation and detection of phonons by picosecond light pulses”, Phys. Rev. B, vol. 34, no. 6, Sep. 1986.

[4.3] P. Ruello and V. E. Gusev, “Physical mechanisms of coherent acoustic phonons generation by ultrafast laser action”, Ultrasonics, vol. 56, pp. 21−35, June 2014.

[4.4] E. M. Strohm, E. S. L. Berndl, and M. C. Kolios, “High frequency label-free photoacoustic microscopy of single cells”, Photoacoustics, vol. 1, pp. 49–53, Aug. 2013.

[4.5] E. M. Strohm, M. J. Moore, and M. C. Kolios, “Single cell photoacoustic microscopy: A review”, IEEE J. Sel. Top. Quantum Electron., no. 6801215, June 2016.

[4.6] A. Bartels, F. Hudert, C. Janke, T. Dekorsy, and K. Köhler, “Femtosecond time-resolved optical pump-probe spectroscopy at kilohertz-scan-rates over nanosecond-time-delays without mechanical delay line”, Appl. Phys. Lett., vol. 88, no. 041117, Jan. 2006.

[4.7] P. Rabinowitz, S. F. Jacobs, T. Shultz, and G. Gould, "Cube-corner Fabry-Perot interferometer," J. Opt. Soc. Am., vol. 52, pp. 452−453, Apr. 1962.

[4.8] P. Franken, A. Hill,C. Peters, and G. Weinreich "Generation of Optical Harmonics", Phys. Rev. Lett., vol. 7, no. 4, Aug. 1961.

[4.9] S. Lin, Z. Sun, B. Wu, and C. Chen, "The nonlinear optical characteristics of a LiB3O5 crystal", J. Appl. Phys., vol. 67, no. 634, Sep. 1989.

[4.10] H. Ichihashi, H. Hayashi, S. Takayanagi, and M. Matsukawa, “Sub-nanosecond pump probe measurement in a Au/Cr bimetal film”, Proceedings of the 7th Asia-Pacific Optical Sensors Conference, Shimane, May 2018.

[4.11] C. B. Scruby, L. E. Drain, Laser Ultrasonics: Techniques and Applications, New York:Adam Hilger, 1990.

5. OBSERVATIONS OF PUMP PROBE RESPONSE UNDER SPR

The sub-nanosecond pump probe system explained in Chapter 4 was improved for measuring the response due to thermoelastic stress under SPR. First, measurement with focusing probe light was conducted to simply measure the responses in the entire angle region near SPR angle because the angle of the cone of radiation by the objective lens was larger than the angle region where SPR occurred. Next, measurement with straightforward probe light was conducted for more detailed investigations considering the effects of the angle dependence of SPR. The objective of this chapter is to show the experimental results of the pump probe measurements under SPR. In Section 5.1, the sample used is explained in detail. In Section 5.2, the improved sub-nanosecond pump probe system with focusing probe light for measurements under SPR is explained. In Section 5.3, the observation results are shown. In Section 5.4, the sub-nanosecond pump probe system with straightforward probe light for more detailed measurement under SPR is explained. Finally, the observation results are also shown in Section 5.5.

5.1 KRETSCHMANN-TYPE SPR SAMPLE

5.1.1 SAMPLE PREPARATION

A SPR sample with simple Kretschmann configuration was prepared for the experiments [5.1]. The sample was composed of a Ag metal film and an isosceles BK7 grass prism (10 mm × 10 mm) (RPB-10-2L, Sigma Koki Co., Ltd., Saitama, Japan). The Ag metal film was deposited on the BK7 glass prism by electron-beam (EB) evaporation (EB1200, Canon Anelva Corp., Kanagawa, Japan). The deposition rate was 0.1 nm/s and the pressure in the chamber was 0.13×10^{-3} Pa. In this study, the Ag metal film of the SPR sample prepared was exposed because the SPR angle and the SPR curve were affected by the SiO_2 protective film coating of the metal film [5.2].

5.1.2 SPR CURVE OF THE SAMPLE

The SPR curve of the sample was measured to confirm the optical characteristic and the film thickness. A wattmeter (S120B, THORLAB, New Jersey, US) and CW laser (mpc3000, Laser Quantum, Manchester, UK) with a wavelength of 532 nm were used in this measurement. Figure 5.1 shows the measured reflectivity as a function of incident angle. The theoretical fitting with the multiple reflection model (described in Section 3.2.3) is also shown in Fig. 5.1, represented by the red solid line. As can be seen in Fig. 5.1, a sharp SPR curve with the full width at half maximum (FWHM) of 0.46° was confirmed. The SPR angle and the minimum value of the reflectivity at the SPR angle were confirmed to be 43.7° and 0.04, respectively.

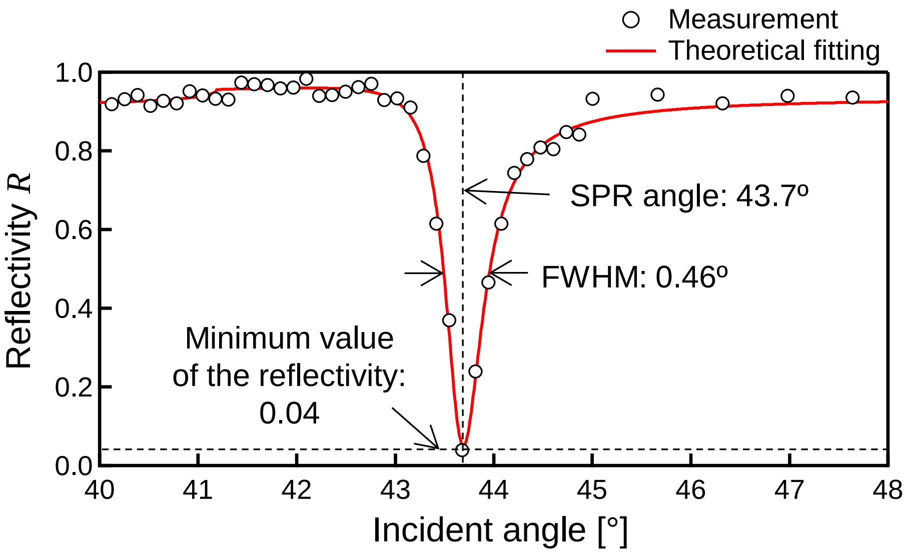

Fig. 5.1 Incident angle dependence of the reflectivity of the SPR sample used. The theoretical fitting is also drawn with a solid red line.

5.1.3 PERMITTIVITY OF THE Ag METAL FILM

The theoretical fitting shown in Fig. 5.1 was obtained by a least-square method with three variable parameters: the real and imaginary parts of the permittivity, and the film thickness of Ag metal film. Therefore, the permittivity of the metal film was determined by the theoretical fitting. The real part Re($\varepsilon_{\mathrm{Ag}}$) and imaginary part Im($\varepsilon_{\mathrm{Ag}}$) of the permittivity were −11.16 and 0.57, respectively. The reported permittivity values of a Ag metal film deposited by EB evaporation were also Re($\varepsilon_{\mathrm{Ag}}$) = −11.17 and Im($\varepsilon_{\mathrm{Ag}}$) = 0.65 (thickness: 19.7 nm) and Re($\varepsilon_{\mathrm{Ag}}$) = −11.19 and Im($\varepsilon_{\mathrm{Ag}}$) = 0.43 (thickness: 160 nm) [5.3]. The real part was in good agreement with the reported values, although the imaginary part was different. One possible reason appears to be the effect of the morphology such as the thickness, the grain diameter, and the surface roughness.

5.1.4 FILM THICKNESS OF THR Ag METAL FILM

The thickness was also determined using the theoretical fitting, which resulted in 56 nm. In addition, the film thickness was measured by a stylus profilometer (Dektak150, Bruker, Billerica, US) for the validation of the measurement results of the permittivity and the film thickness by the theoretical fitting. Obtained profile is shown in Fig. 5.2. The measurement value was 55.9 nm, which was in good agreement with the measurement value from the theoretical fitting. Therefore, the measurement results by the theoretical fitting were validated.

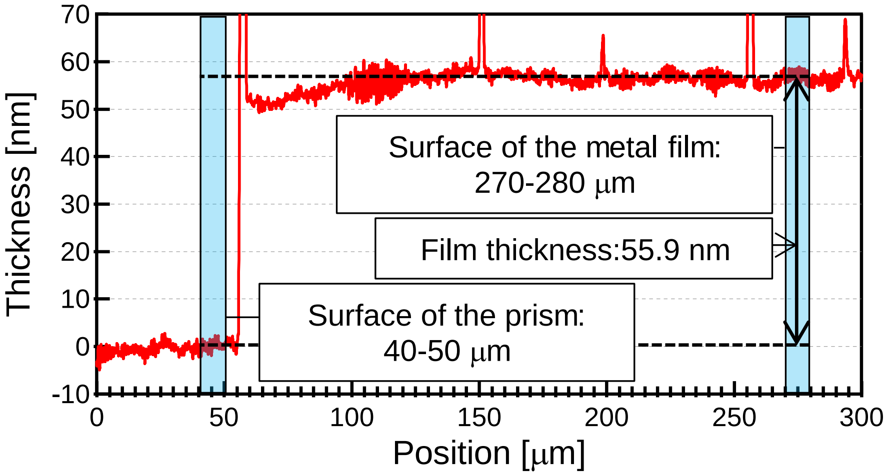

Fig. 5.2 Measurement profile at the interface between the deposition area and the non-deposition area obtained using a stylus profilometer.

5.1.5 GRAIN DIAMETER OF THR Ag METAL FILM

The grain diameter was also measured. Figure 5.3 is a scanning electron microscopy (SEM) (S2460N, Hitachi, Ltd., Tokyo, Japan) image of the surface of the Ag metal film. The histogram of the grain diameter obtained from the SEM image is also shown in Fig. 5.4. As a result, the average value of the grain diameter was 47 nm.

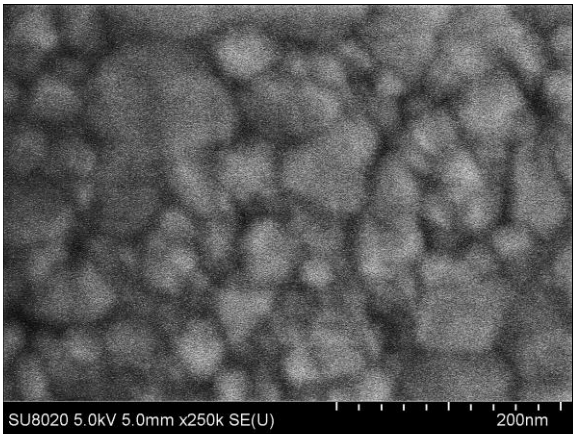

Fig. 5.3 A SEM image of the surface of the Ag metal film.

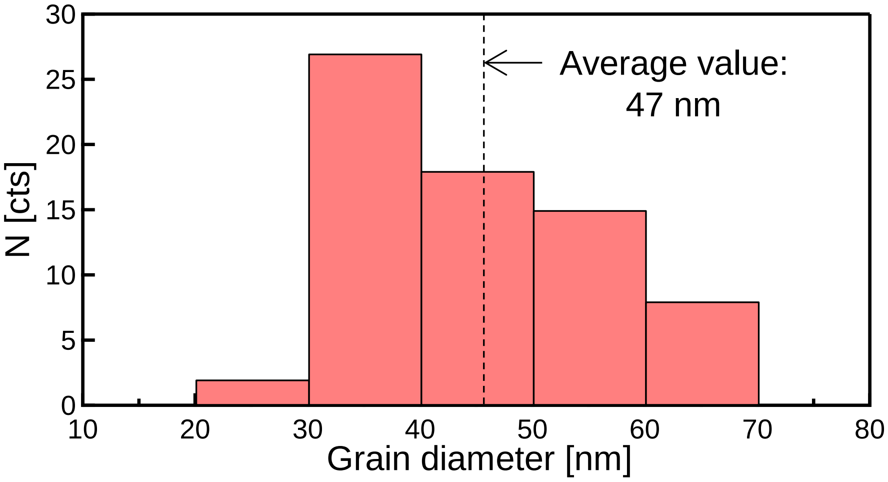

Fig. 5.4 Histogram of the grain diameter obtained from the SEM image in Fig. 5.3.

5.1.6 SURFACE ROUGHNESS OF THE Ag METAL FILM

Figure 5.5 shows the image data of the surface roughness of the Ag metal film. This data was measured by an atomic force microscopy (AFM) (NanoWizard III NW3-XS-O, Bruker, Berlin, Germany). The histogram of the surface roughness is also shown in Fig. 5.6. Here, the surface roughness was determined as a root-mean square roughness r_{rms}, which is described in the following equation:

$$r_{\mathrm{rms}} = \sqrt{\frac{1}{L}\int_0^L \left|f_{\mathrm{rp}}(x)\right|^2 dx} \tag{5.1}$$

where, L is the measurement length, f_{rp} is the roughness profile. As a result, the determined root-mean-square roughness of the film was 1.8 nm.

Finally, the obtained physical parameters of the SPR sample (Ag metal film) are summarized in Table 5.1.

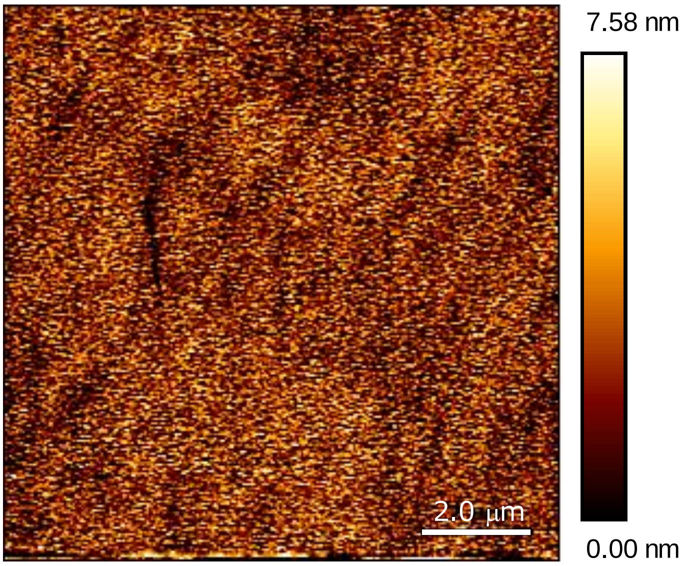

Fig. 5.5 An AFM image of the surface of the Ag metal film.

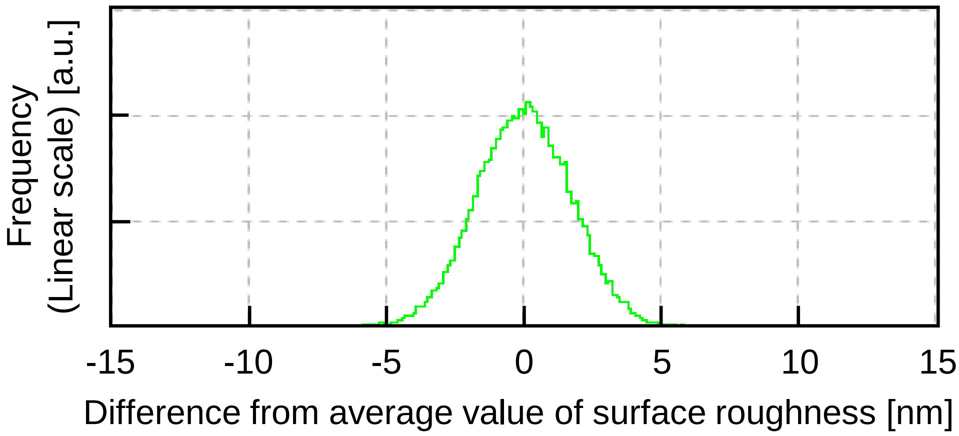

Fig. 5.6 Histogram of the surface roughness obtained from the AFM image in Fig. 5.5.

Table 5.1 Determined physical parameters of the SPR sample used (Ag metal film)

Optical parameter		Morphological parameter		
Re($\varepsilon_{\mathrm{Ag}}$) [a.u.]	Im($\varepsilon_{\mathrm{Ag}}$) [a.u.]	Film thickness [nm]	Grain diameter [nm]	Surface roughness [nm]
−11.16	0.57	56	47	1.8

5.2 SUB-NANOSECOND PUMP PROBE SYSTEM WITH FOCUSING PROBE LIGHT UNDER SPR

When the angle of the cone of probe light radiation by the objective lens is larger than the angle region where SPR exists, it is expected that the utilization of focusing probe light enables measurement of the responses in the entire angle region near SPR angle [5.4]. The improved sub-nanosecond pump probe system with focusing probe light is shown in Fig. 5.7. The explanation of the system is described below.

In this system, the repetition frequency of the laser was 10 kHz. The pump light was modulated with a mechanical light chopper with a chopping frequency of 250 Hz. In this measurement system, the measurement sample used with simple Kretschmann configuration composed of a Ag metal film and a BK7 glass prism was mounted on a rotation stage. The probe light was focused on the glass prism/metal interface of the sample using an objective lens with a focal length of 20 mm (PAL-20-NIR-HR-LC00, Sigma Koki Co., Ltd., Saitama, Japan). While, the pump light was focused on the air/metal interface using a focus lens with a focal length of 60 mm. The energy of the pump light was 0.1 μJ/pulse, and the energy of the probe light was several hundred times less than that. The spot diameters of the pump and probe lights were 32 and 5 μm, respectively. The probe light reflected on the sample was allowed to pass through a harmonic separator (HS) to filter the scattering light from the pump light, and was inputted to a balanced detector.

The pump light and the probe light were aligned to irradiate at the same area by microscopic observation. Figures 5.8 (a) and (b) show the spot images of the reflected probe light in SPR condition and non-SPR condition, respectively. They were obtained by switching the optical polarization of the probe light to p-polarization (SPR condition) and s-polarization (non-SPR condition) by a ½-λ plate in front of the sample as shown in Fig. 5.8 (c). This is because the surface plasmon wave k_{sp} needed to obtain SPR was not induced by the incident laser with s-polarization. Figures 5.8 (a) and (b) confirm the strong attenuation of reflectivity indicated by the disappearance of the center line. This is because the FWHM of the SPR curve (0.46°) was lower than the converging angle (1.1°) of the OL.

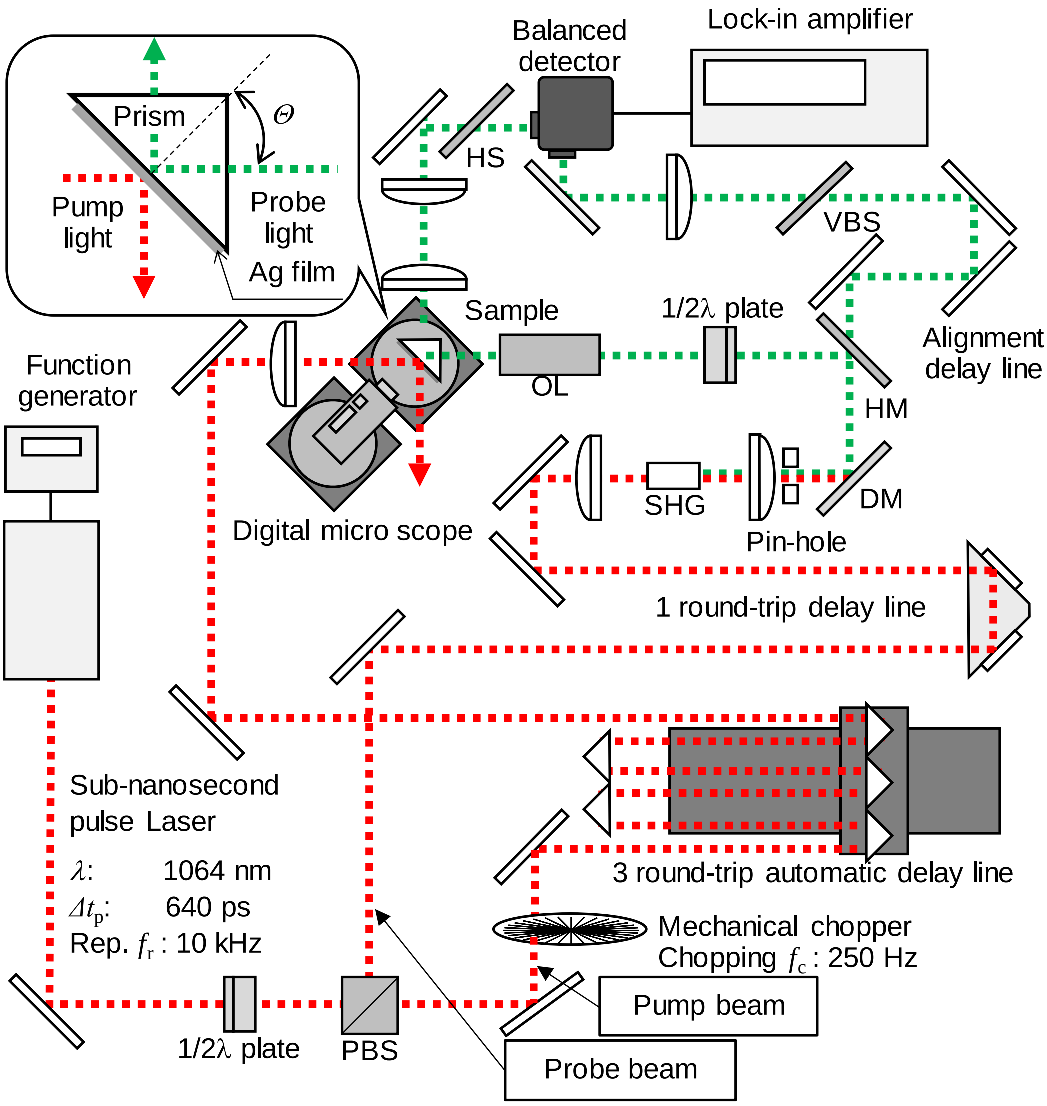

Fig. 5.7 Improved sub-nanosecond pump probe system with focusing pump and probe lights for observing the response due to thermoelastic stress under SPR. The signal of mechanical light chopper was used as a reference signal for the lock-in amplifier.

PBS: Polarization beam splitter,	SHG: Second harmonic generator,
DM: Dichroic mirror,	HM: Half mirror,
HS: Harmonic separator,	VBS: Variable beam splitter
OL: Objective lens.	

s-polarization
(Non-SPR condition)
(a)

p-polarization
(SPR condition)
(b)

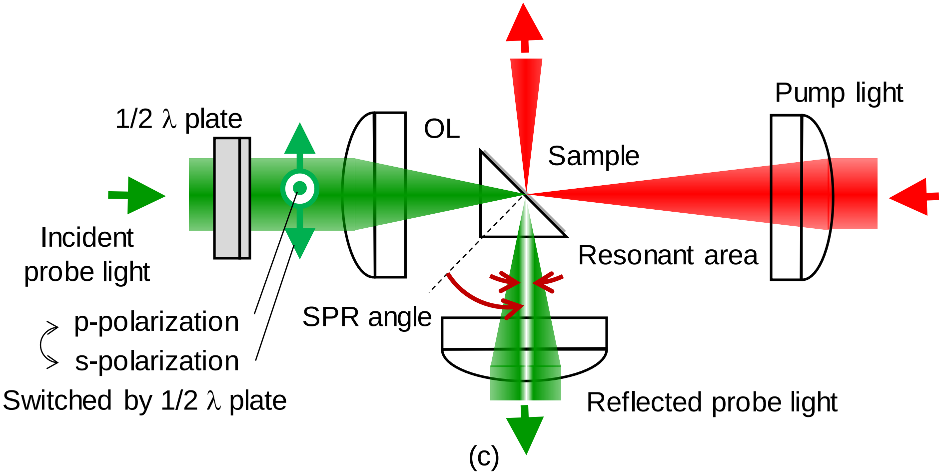

(c)

Fig. 5.8 (a) A spot image of the reflected probe light in non-SPR condition.
(b) A spot image of the reflected probe light in SPR condition.
(c) The method applied to switch the optical polarization of the probe light.

5.3 TRANSIENT RESPONSE MEASURED BY THE SYSTEM WITH FOCUSING PROBE LIGHT UNDER SPR

At first, using the developed sub-nanosecond pump probe system, the reflectivity changes in the pulsed probe light due to the pulsed pump irradiation were observed while changing the polarization of the incident probe light. Figure 5.9 shows the reflectivity changes in the probe light with p-polarization (pump probe measurement of the SPR condition) and s-polarization (pump probe measurement of the non-SPR condition). Here, the response caused by the transient stress due to the thermoelastic effect clearly appeared with the reflectivity change of the p-polarization probe light (SPR condition), while no signal appeared with the s-polarization probe light (non-SPR condition). Thus, the reflectivity change in the SPR condition became more sensitive to the thermal and stress effects than that in the non-SPR condition.

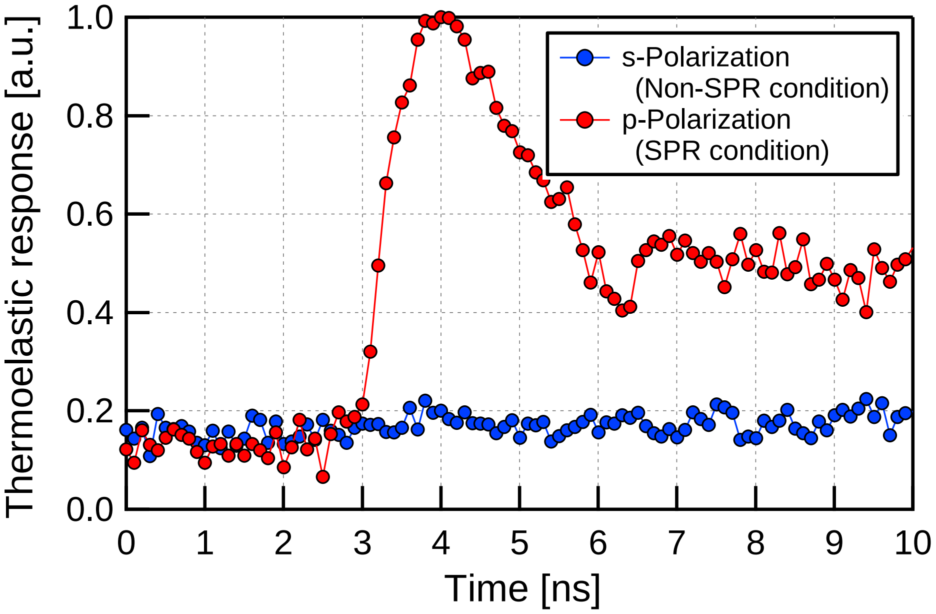

Fig. 5.9 Transient thermoelastic responses observed using the pump probe technique with probe lights of p-polarization (SPR condition) and s-polarization (non-SPR condition). These responses were measured by the system with the focused probe light shown in Fig. 5.7.

As a supplemental experiment, transient responses of the reflectivity change were observed while changing the incident angle of the probe light near the SPR angle θ_r. The observed responses as a function of the incident angle of the probe light are shown in Fig. 5.10. As can be seen in Fig. 5.10, the response due to thermoelastic stress did not appear at the incident angles of $\theta_r - 2.5°$ and $\theta_r + 6.0°$. At these incident angles, it was confirmed that the optical reflectivities were not attenuated by SPR, as seen in Fig. 5.1. While, at incident angles of $\theta_r - 0.5°$, θ_r, and $\theta_r + 0.5°$, where the optical reflectivities were attenuated by SPR, strong thermoelastic responses appeared as the incident angle approached the SPR angle. These data validate the results in Fig. 5.9, showing that they were caused by SPR and were not merely due to a difference in optical polarization. Thus, by utilizing the SPR, it results in the increase of reflectivity change with the elastic and thermal effects at the sub-nanosecond timescale.

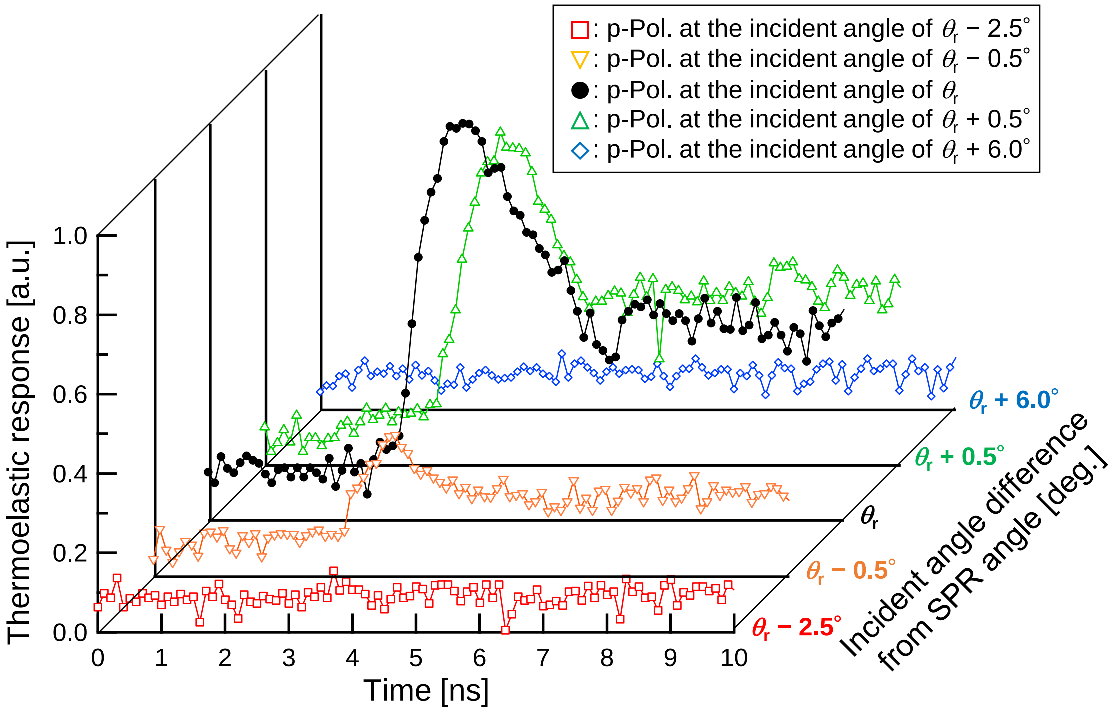

Fig. 5.10 Transient thermoelastic responses observed using the pump probe technique near the SPR angle. θ_r is the SPR angle. These responses were measured using the system with focused probe light shown in Fig. 5.7.

5.4 SUB-NANOSECOND PUMP PROBE SYSTEM WITH STRAIGHTFORWARD PROBE LIGHT UNDER SPR

The system shown in Fig. 5.7 with focusing probe light attained the measurement of the response in the entire angle region where SPR occurs because the converging angle of the OL was larger than the FWHM of the SPR curve. Moreover, the incident angle dependence of the transient responses was measured. As a result, strong transient responses appeared as the incident angle approached the SPR angle. This tendency was in good agreement with the reports of the picosecond and femtosecond pump probe measurements with focusing probe light under SPR by Katayama et al. [5.5] and Wang, et al. [5.6]. However, the system with focusing probe light cannot investigate the change of the SPR curve, which means that this system cannot reveal the mechanism of the pump probe response under SPR because the measurement considering the incident angle dependence of the SPR cannot be measured. Thus, sub-nanosecond pump probe system with straightforward probe light was prepared for more detailed investigations of the pump probe responses under SPR.

5.4.1 SYSTEM CONFIGURATION

The system is shown in Fig. 5.11. The explanation of the system is described below.

The pulse duration and wavelength of the pulsed laser (Herios 1064-5-50, Coherent Inc., Santa Clara, CA) were 640 ps and 1064 nm, respectively. The repetition frequency was 10 kHz. The pump light was modulated with a chopping frequency of 3.5 kHz by a mechanical light chopper (5584A, NF Corp., Kanagawa, Japan). When the probe light entered the LBO crystal, it was focused using a focus lens (L1) with a focal length of 400 mm and was collimated using a focus lens (L2) with a different focal length of 120 mm, which attained the narrow beam with the spot diameter of 400 μm. The probe light was focused on the prism/metal surface of the SPR sample using a focus lens (L3) with a long focal length of 250 mm. In contrast, the pump light was focused on the air/metal surface using a focus lens (L4) with a long focal length of 450 mm. The focal length of L3 was long enough to neglect the converging angle dependence of SPR because the angle of the cone of irradiation was sufficiently smaller than the angle region of SPR. The pulse energies of the pump and probe lights were measured, which were 16.0 μJ/pulse and 1.7 nJ/pulse, respectively. The pump and probe lights were aligned to irradiate at the same area by microscopic observation.

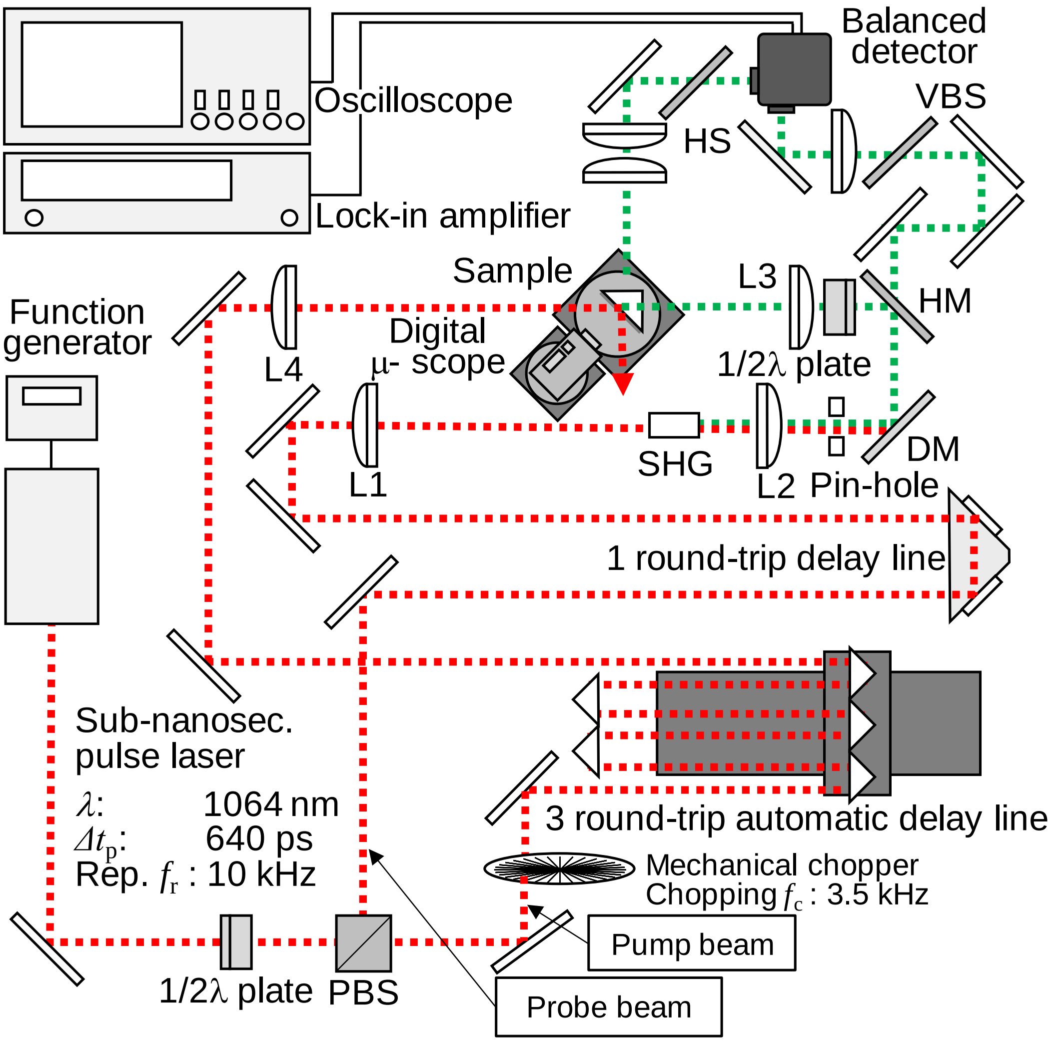

Fig. 5.11 Improved sub-nanosecond pump probe system with straightforward probe light for detailed investigations of the transient responses due to thermoelastic stress under SPR. The focal lenses (L1 and L2) were used to attain the narrow beam. The focal length of the lens in front of the sample (L3) was long enough to neglect the converging angle, which attains the straightforward probe light. The signal of mechanical light chopper was used as a reference signal for the lock-in amplifier.

PBS: Polarization beam splitter, SHG: Second harmonic generator,
DM: Dichroic mirror, HM: Half mirror,
HS: Harmonic separator, VBS: Variable beam splitter

5.4.2 SPOT DIAMETER

The spot diameters of the pump and probe lights were measured by the knife edge method. Knife edge method enables the determination of the spot diameter by measuring the transmitted light intensity as a function of the position of the knife edge. Then, the spot diameter r_{spot} is defined as the following equation [5.7]:

$$r_{\mathrm{spot}} = 1.56 \times |L_{0.9} - L_{0.1}| \tag{5.2}$$

where, $L_{0.9}$ and $L_{0.1}$ are the positions of the knife edge where the intensities of the transmitted light become 0.9- and 0.1-times the incident light. Figures 5.12 and 5.13 are the measurement data of the intensity of transmitted probe and pump lights at the focused position as a function of the position of the knife edge, respectively. As a result, the focused spot diameters of the pump and probe lights were 952 µm and 390 µm, respectively.

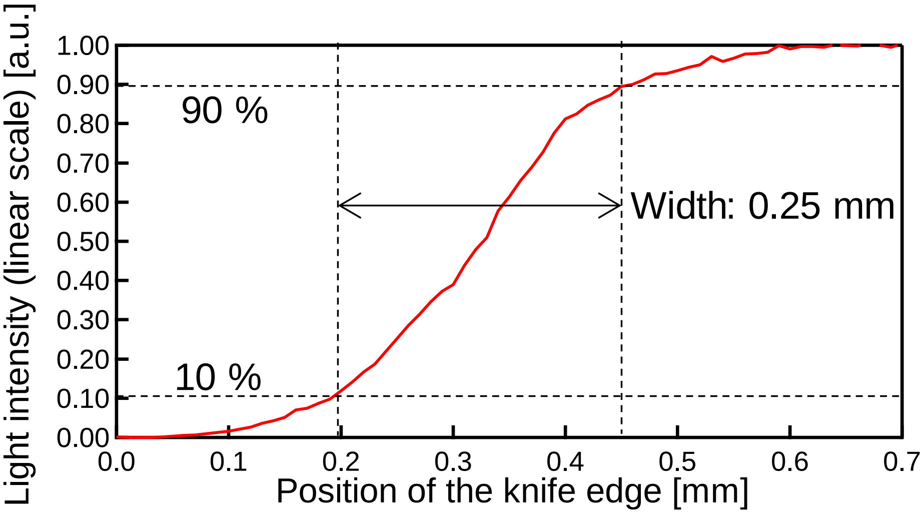

Fig. 5.12 Intensity of the transmitted probe light as a function of the position of the knife edge.

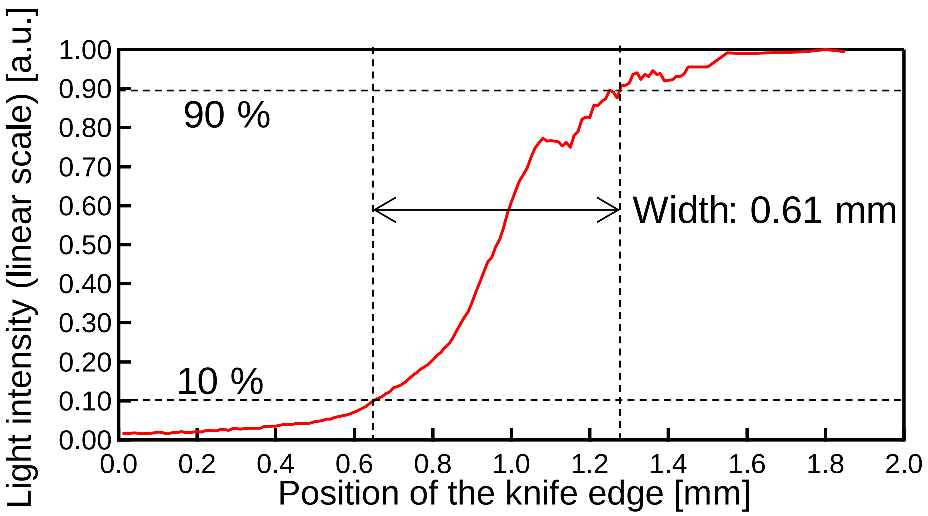

Fig. 5.13 Intensity of the transmitted pump light as a function of the position of the knife edge.

5.4.3 CONVERGING ANGLE

The converging angle of the probe light is important for the system because it affects the SPR characteristic. The spot diameters at the focused position and the position before focusing with a lens were measured by the knife edge method to confirm the converging angle. Fig. 5.14 shows the measurement data of the intensity of transmitted probe lights at the focused position and the position before focusing as a function of the position of the knife edge. As can be seen in Fig. 5.14, both spot diameters were nearly same. As a result, the converging angle of the probe light was approximately 0º. The probe light was successfully focused into a straight light in the system.

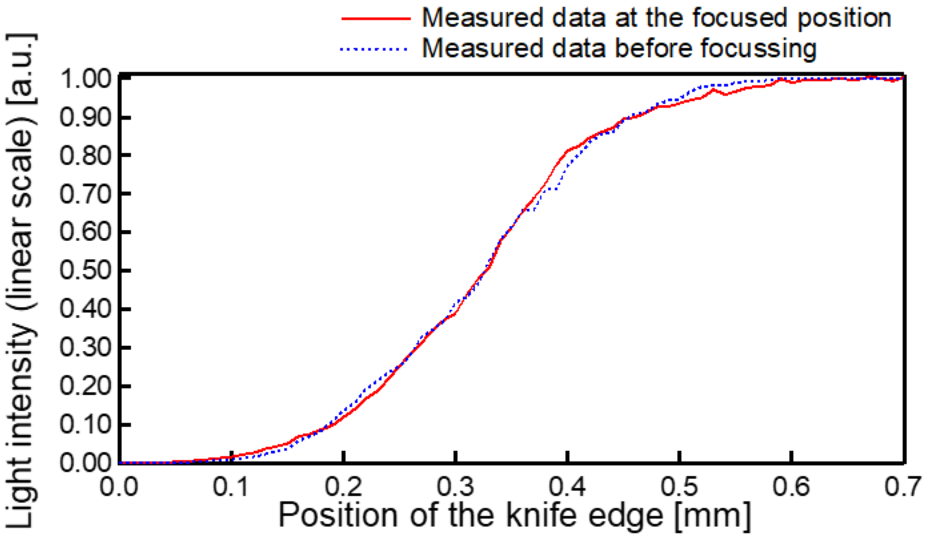

Fig. 5.14 Intensities of the transmitted probe lights at the focused position and the position before focusing as a function of the position of the knife edge.

5.4.4 REFLECTIVITY CHANGE

In the measurements using this system, the reflectivity change was determined by a balanced detector and a lock-in amplifier. The measured reflectivity change $|\Delta R'|$ is described below:

$$|\Delta R'| = \frac{V_{\omega}(\omega_{\mathrm{r}})}{AGI_0} \tag{5.3}$$

where, V_ω is the output voltage measured by a lock-in amplifier, ω_r is the modulation frequency by a mechanical light chopper, I_0 is the light intensity of the probe light, and G (2.34×10^5 V/W) is the gain of the balanced detector depending on the sensitivity (0.234 A/W) and the transimpedance (10^4 Ω). A is the conversion coefficient between the outputs of the balanced detector and the lock-in amplifier, which is 0.0203.

5.5 TRANSIENT RESPONSE MEASURED BY THE SYSTEM WITH STRAIGHTFORWARD PROBE LIGHT UNDER SPR

The transient responses due to the pump light irradiation were measured by the probe lights with the s-polarization (non-SPR condition) and p-polarization (SPR condition). The measured responses were shown in Fig. 5.15. These responses were measured by the probe light with the incident angle of $\theta_r + 0.18°$. Here, the transient response caused by the thermoelastic stress clearly appeared as the reflectivity change of the p-polarization probe light (SPR condition), while, no signal appeared with the s-polarization probe light (non-SPR condition). These data showed the same results with those measured using the system with focused probe light, which are shown in Fig. 5.9. However, clear response with lower noise was obtained compared with that measured by the system with focused probe light with p-polarization.

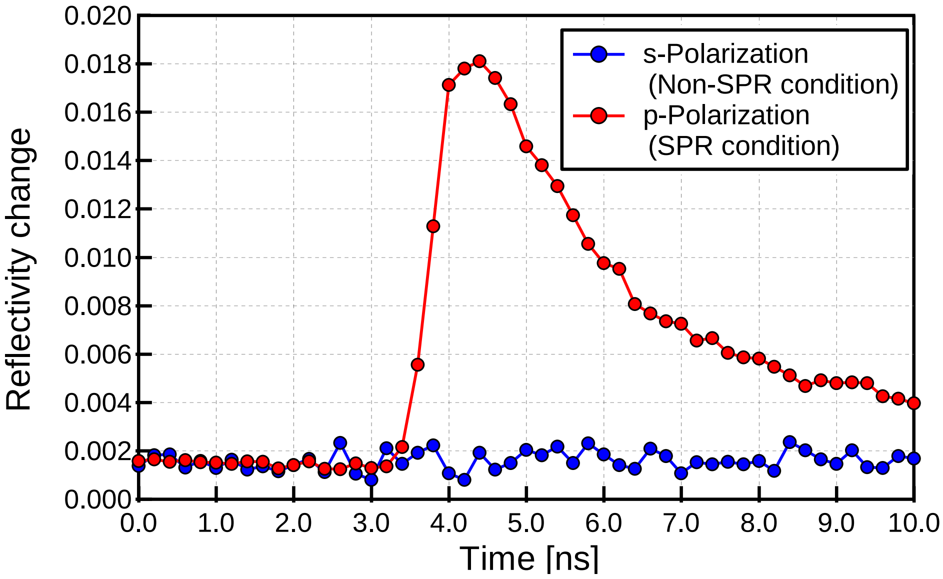

Fig. 5.15 Transient thermoelastic responses observed by the pump probe technique with probe lights of p-polarization (SPR condition) and s-polarization (non-SPR condition). These responses were measured by the system with the straightforward probe light shown in Fig. 5.11.

The transient time responses of the reflectivity as a function of incident angle are shown in Fig. 5.16. As can be seen in Fig. 5.16, the reflectivity changes near the SPR angles of θ_r and $\theta_r + 0.04°$ were lower than those at the far angles of $\theta_r - 0.06°$ and $\theta_r + 0.18°$. This tendency is different from that measured by the system with focused probe light shown in Fig. 5.10. Such different tendencies were initially attributed to the converging angle of the probe light. However, the converging angle of this system was approximately 0º. Thus, the converging angle of the probe light in the system was actually low enough to ignore its effect on the measured responses. In contrast, the spot diameter and the focal length of the probe light in the system with the focused probe light were 5 μm and 20 mm, respectively. Therefore, the converging angle of the probe light in the system was around 1.1º, whereas, the full width at half maximum (FWHM) of the dip of the SPR curve shown in Fig. 5.1 was 0.46º. It was lower than the converging angle. Here, the response measured by the pump probe system under SPR results in the sum of those in the entire converging angles. Because of it, the tendency of the responses measured by the system with focused probe light had maximum response at the SPR angle while that measured by the system with straightforward probe light had maximum responses at two angles, of which one was larger and the other was lower than the SPR angle. In the system with straightforward probe light, the minimum reflectivity change was observed at the angle of θ_r + 0.04º, which was not the SPR angle. Considering these results, it was assumed that the reflectivity changes were caused by the broadening of the SPR curve and the shift of the SPR angle.

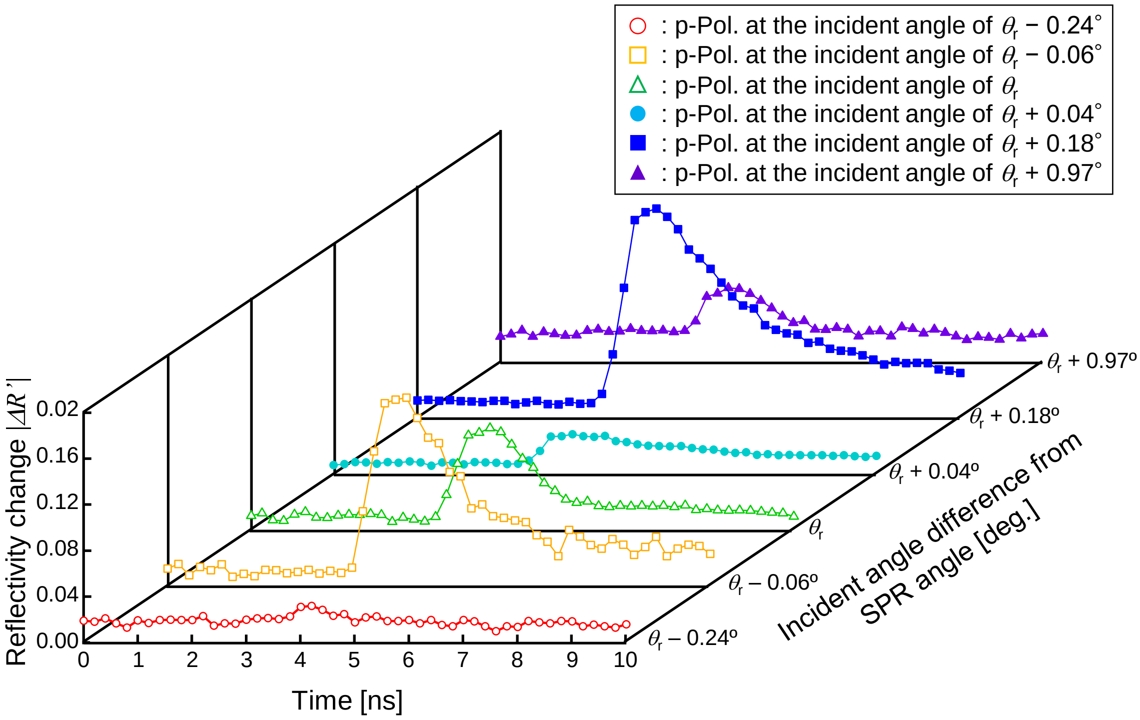

Fig. 5.16 Transient thermoelastic responses observed by the pump probe technique near the SPR angle. θ_r is the SPR angle. These responses were measured by the system with the straightforward pump and probe lights shown in Fig. 5.11.

REFERENCES

[5.1] W. H. Weber and G. W. Ford, "Optical electric-field enhancement at a metal surface arising from surface -plasmon excitation", Opt. Lett., vol. 6, no. 3, pp. 122−124, Dec. 1980.

[5.2] M. Chikhi and F. Benkabou, “Theoretical analysis of multilayer surface plasmon resonance sensors using thin-film optical admittance formalism”, Plasmonics, vol. 10, pp. 1467−1472, Apr. 2015.

[5.3] D. T. Owens, C. Fuentes-Hernandez, J. M. Hales, J. W. Perry, and B. Kippelen, "A comprehensive analysis of the contributions to the nonlinear optical properties of thin Ag films", J. Appl. Phys., vol. 107, no. 123114, Apr. 2010.

[5.4] H. Ichihashi, H. Hayashi, S. Takayanagi, M. Matsukawa, and Y. Watanabe, “Highly sensitive detection of photo-thermal transient stress by a sub-nanosecond pump probe with surface plasmon resonance”, AIP Advances, vol. 8, no. 105102, Sep. 2018.

[5.5] K. Katayama, T. Sawada, Q. Shen, and A. Harata, "Detection of photoinduced electronic, thermal, and acoustic dynamics of gold film using a transient reflecting grating method under three types of surface plasmon resonance conditions", Phys. Rev. B, vol. 58, no. 13, Apr. 1998.

[5.6] J. Wang, J. Wu, and C. Guo, "Resolving dynamics of acoustic phonons by surface plasmons", Opt. Lett., vol. 32, no. 6, pp. 719−721, Dec. 2006.

[5.7] Y. Suzuki and A. Tachibana, "Measurement of the mm sized radius of Gaussian laser beam using the scanning knife-edge", Appl. Opt., vol. 14, no. 12, pp. 2809−2810, Dec. 1975.

6. THEORETICAL MODEL OF THE SUB-NANOSECOND PUMP PROBE RESPONSE UNDER SPR

An integrated theoretical model of the pump probe response under SPR by a sub-nanosecond pump probe system was constructed in order to understand the mechanism of the optical reflectivity change due to the irradiation of the pump light. The conceptual enlarged view around the SPR sample is shown in Fig. 6.1. Constructed theoretical model is composed of six steps, the preparation of the laser profile, temperature increase at the irradiated area of the pump light, generation of the thermoelastic stress, estimation of the permittivity change in the Ag metal film, estimation of the reflectivity change and final convolution process. The block diagram of the theoretical model is summarized in Fig. 6.2.

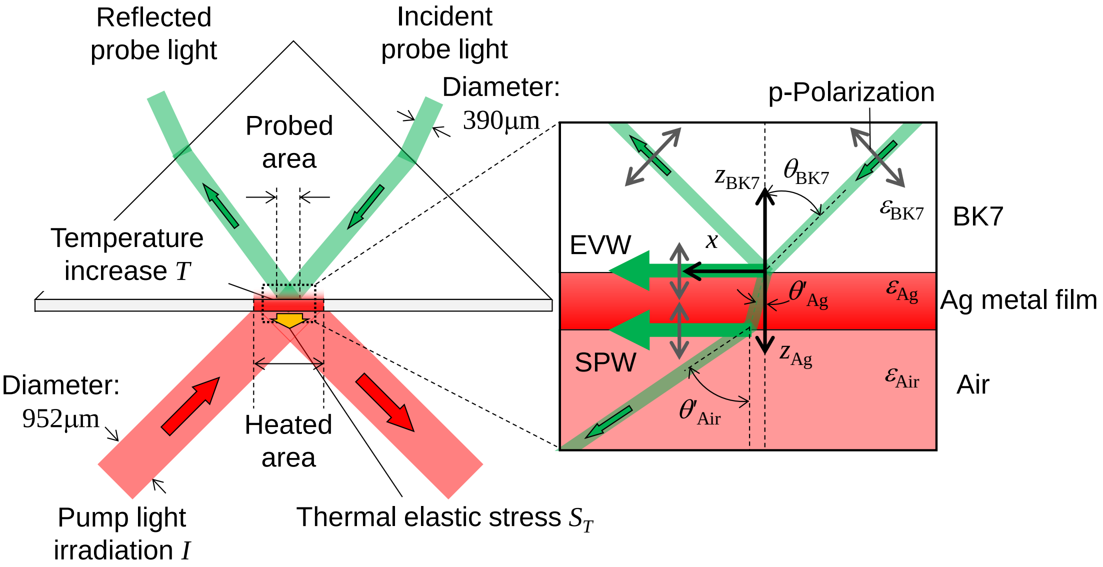

Fig. 6.1 The conceptual enlarged view around a SPR sample with Kretschmann configuration. x is the axis of the in-plane direction in the Ag metal film. z_{Ag} and z_{BK7} are the axis of the normal directions in the Ag metal film and the BK7 glass prism. The spot diameters of the probe and pump lights were 390 and 952 μm, respectively. θ_{BK7} is the incident angle of the probe light in the BK7 glass prism. θ'_{Ag} and θ'_{Air} are the refraction angles in the Ag metal film and the air. ε_{BK7}, ε_{Ag} and ε_{Air} are the permittivities of the BK7 glass prism, the Ag metal film and the air, respectively.

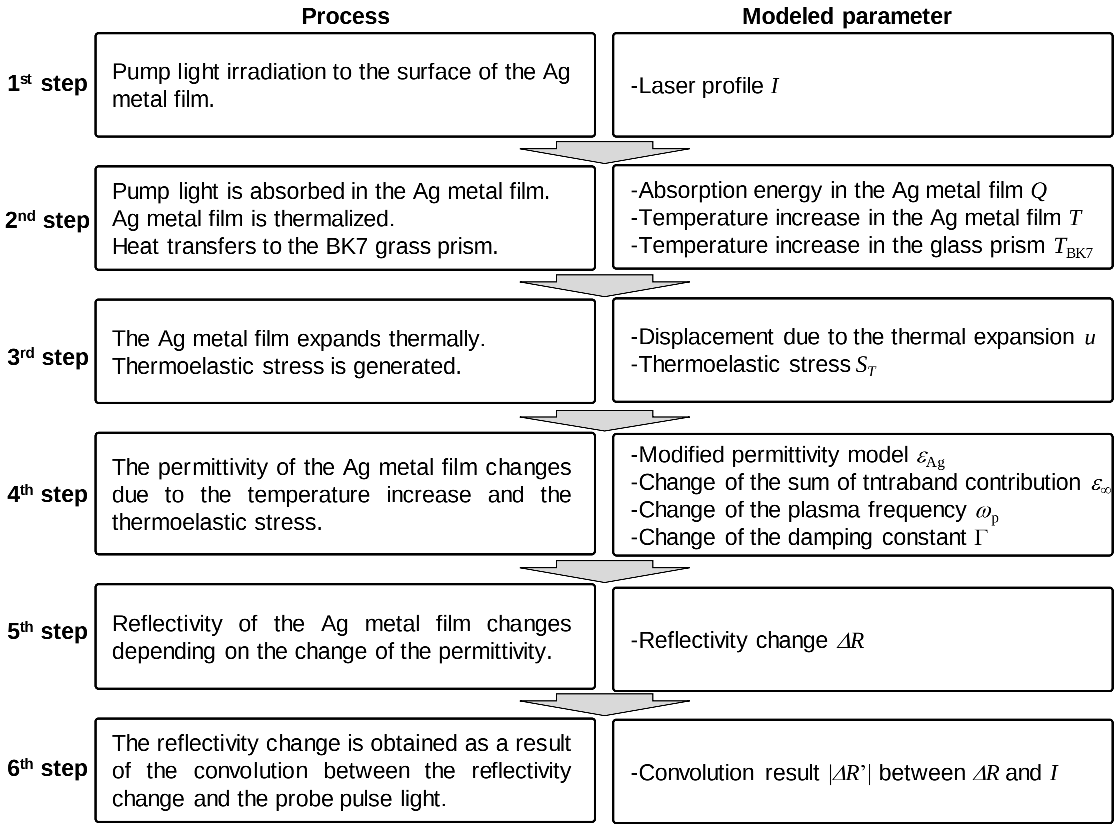

	Process	**Modeled parameter**
1st step	Pump light irradiation to the surface of the Ag metal film.	-Laser profile I
2nd step	Pump light is absorbed in the Ag metal film. Ag metal film is thermalized. Heat transfers to the BK7 grass prism.	-Absorption energy in the Ag metal film Q -Temperature increase in the Ag metal film T -Temperature increase in the glass prism T_{BK7}
3rd step	The Ag metal film expands thermally. Thermoelastic stress is generated.	-Displacement due to the thermal expansion u -Thermoelastic stress S_T
4th step	The permittivity of the Ag metal film changes due to the temperature increase and the thermoelastic stress.	-Modified permittivity model $\varepsilon_{\mathrm{Ag}}$ -Change of the sum of tntraband contribution ε_∞ -Change of the plasma frequency ω_{p} -Change of the damping constant Γ
5th step	Reflectivity of the Ag metal film changes depending on the change of the permittivity.	-Reflectivity change ΔR
6th step	The reflectivity change is obtained as a result of the convolution between the reflectivity change and the probe pulse light.	-Convolution result $\lvert\Delta R'\rvert$ between ΔR and I

Fig. 6.2 The block diagram of the integrated theoretical model of the pump probe response under SPR by the system where a pulsed laser with the duration of sub-nanosecond range is used.

The objective of this chapter is to explain the constructed theoretical model. In Section 6.1, the process of the preparation of the laser profile was explained. In Section 6.2, the energy absorption and the temperature increase in the Ag metal film due to the irradiation of the pump light is described. In Section 6.3, the thermoelastic stress generated by the temperature increase is described. In Section 6.4, the modified permittivity model and the change due to the temperature increase and the generated thermoelastic stress are described. In Section 6.5, the reflectivity change is explained considering the permittivity change of the Ag metal film. Finally, the convolution process necessary for the pump probe measurement is explained in Section 6.6.

6.1 LASER PROFILE

As the first step, the laser profile was assumed as a Gaussian function. To make the model of the pulsed laser form used in the pump probe system, the pulsed wave form of the laser was measured by a photodiode (S9055-01, Hamamatsu photonics corp., Shizuoka, Japan). Considering the measured pulsed wave form resulted from convolution with the Gaussian filter of the photodiode with cutoff frequency of 2.0 GHz (described in the specification of the photodiode), the duration (full width at half maximum) of the laser pulse was determined, which was 640 ps. Figure 6.3 shows the measured pulsed wave form and estimated laser profile $I(t)$. Here, the laser profile $I(t)$ is written as:

$$I(t) = I_0 exp\left[-\frac{4\xi}{\tau_0}(t-t_0)^2\right] \tag{6.1}$$

where, I_0 is the light intensity of the laser, ξ is the $-\log_e(1/2)$, τ_0 (= 640 ps) is the duration of the laser, and t_0 is the irradiation time of the pump light.

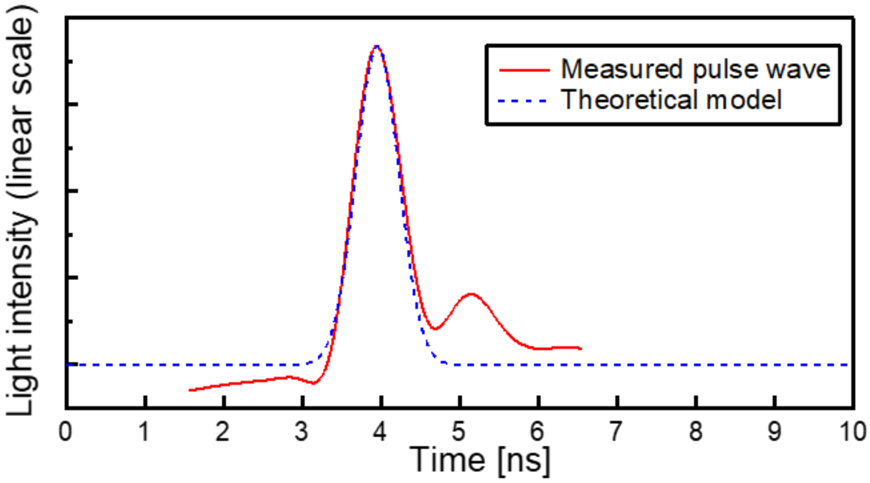

Fig. 6.3 The pulsed wave of the sub-nanosecond pulsed laser used and the estimated Gaussian laser profile. In the estimated profile, the response time of the photodiode was considered by the convolution.

6.2 ENERGY ABSORPTION AND TEMPERATURE INCREASE

In the second step, the energy absorption $Q(t)$ and the temperature increase $T(t)$ in the Ag metal film due to the pump light irradiation were estimated using a plane wave approximation. The plane wave approximation is reasonable because the diameter of the pump light is sufficiently larger than that of the probe light. Here, the absorptance q per unit depth is written below:

$$q = \gamma_a \exp(-\gamma_a z_{\mathrm{Ag}}) \tag{6.2}$$

where, γ_a ($= 8.6 \times 10^7$ m^{-1}) is the optical absorption coefficient of the Ag metal film [6.1] and z_{Ag} is the position of the normal direction in the Ag metal film. The absorbance in the Ag metal film is written below:

$$q_{all} = \int_{z_{\mathrm{Ag}}=0}^{z_{\mathrm{Ag}}=d} \gamma_a \exp(-\gamma_a z_{\mathrm{Ag}})\, dz_{\mathrm{Ag}} \tag{6.3}$$

where, d is the film thickness of the Ag metal film. The estimated light absorbance as a function of the depth position of Ag is shown in Fig. 6.4.

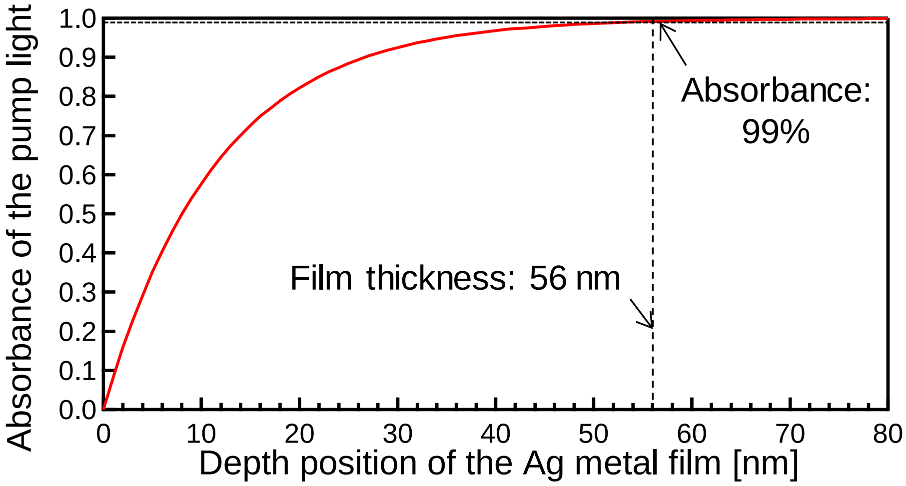

Fig. 6.4 Estimated light absorbance plotted as a function of the depth position of the Ag. Wavelength was assumed to be 1064 nm in the estimation.

The absorbance of the Ag metal film was estimated to be 99% because the film thickness was sufficiently thick, which was 56 nm. Therefore, it was assumed that most of the pump light transmitted through the surface of the Ag metal film is absorbed in the film. However, the reflected component of the irradiated pump light is not absorbed in the Ag metal film, but only the transmitted component. Thus, the surface density of the absorbed energy in the Ag metal film $Q(t)$ was estimated using the following equation:

$$Q(t) = \tilde{I}(t)(1 - R)q_{all} \cong \tilde{I}(t)(1 - R) \tag{6.4}$$

where, $\tilde{I}(t)$ is the surface energy density of the pump light and R (= 0.98) is the optical reflectance [6.2].

Next, the temperature increase in the Ag metal film $T(t)$ was estimated using the following equations:

$$\frac{\partial^2 T_{\mathrm{BK7}}(z_{\mathrm{BK7}},t)}{\partial z_{\mathrm{BK7}}^2} - \frac{1}{K_T}\frac{\partial T_{\mathrm{BK7}}(z_{\mathrm{BK7}},t)}{\partial t} = -\frac{1}{k_c}Q(t) \tag{6.5}$$

$$T(t) = T_{\mathrm{BK7}}(z_{\mathrm{BK7}},t)|_{z_{\mathrm{BK7}}=0} \tag{6.6}$$

where, z_{BK7} is the position of the normal direction in the BK7 glass prism and $T_{\mathrm{BK7}}(z_{\mathrm{BK7}}, t)$ is the temperature increase in the BK7 glass prism. K_T (= 0.529×10^{-6} m^2/s) and k_c (= 1.01 W/mK) are the thermal diffusion coefficient and the thermal conductivity of the BK7 glass prism, respectively [6.2]. As shown in Equation (6.4), the energy of the transmitted pump light at the surface of the Ag metal film is nearly absorbed and changes to heat. The induced heat in the Ag metal film rapidly conducts toward the direction of the film thickness. The conduction time of the heat in the Ag metal film is very short compared with the pulse duration of the pump light of 640 ps because the time constant (= $d^2 / 4K_T$) of the thermal diffusion in the Ag metal film through the distance of its film thickness is 4.6 ps [6.3, 6.4, 6.5]. Therefore, the temperature in the Ag metal film is treated as an equilibrium condition. As shown in Equation (6.5), the heat conducts into the BK7 glass prism following the well-known thermal diffusion equation because the external air medium acts as a heat insulator [6.6]. Thus, it was assumed that the temperature of the Ag metal film was equal to that of the BK7 glass prism at the interface, as shown in Equation (6.6). Here, the temperature increase is obtained by the following equation:

$$T(t) = \frac{1}{k_c}\sqrt{\frac{K_T}{\pi}} \int_{\tau=0}^{\tau=t} \frac{Q(t-\tau)}{\sqrt{\tau}} \exp\left(\frac{-z_{\mathrm{BK7}}^2}{4K_T\tau}\right) d\tau \Bigg|_{z_{\mathrm{BK7}}=0} \tag{6.7}$$

where, τ is the integral variable. As shown in Equation (6.7), the temperature increase was obtained using Duhamel’s theory [6.6].

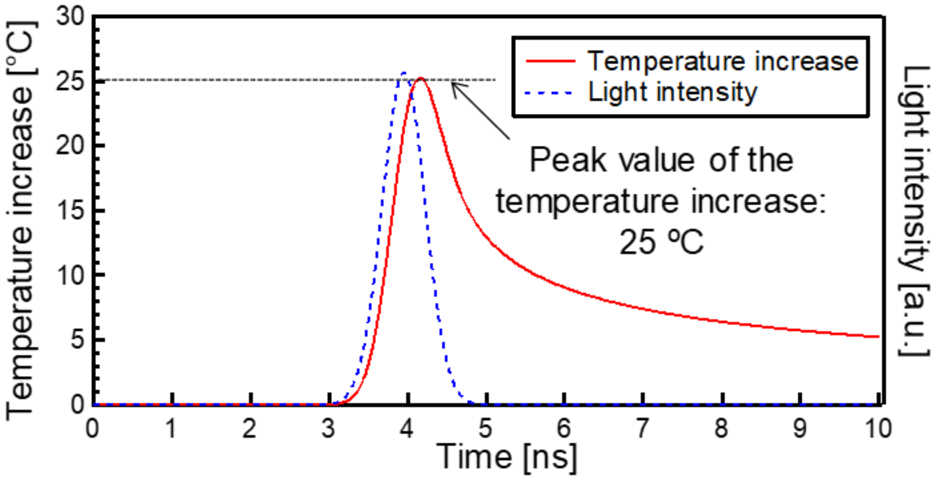

Fig. 6.5 Theoretical estimation of the temperature increase in the Ag metal film and the estimated Gaussian laser profile.

The obtained temperature increase is the average values in the film. The estimated temperature is shown in Fig. 6.5. The peak value of the estimated temperature increase was around 25 ºC, which was not high, owing to the low power density of the pump light. In these simple estimations, the interfacial thermal resistance between the BK7 glass prism and the Ag metal film, and the gradient of the intrinsic temperature in the Ag metal film were ignored. The model is, however, valid because the time scale of the pump light is sufficiently long for the thermal equilibrium condition.

6.3 THERMOELASTIC STRESS

In the third step, the thermoelastic stress $S_T(t)$ in the Ag metal film due to the pump light irradiation was also estimated using a plane wave approximation. The thermoelastic stress $S_T(t)$ in the Ag metal film was estimated using the following equations:

$$S_{\mathrm{ext}} = c_{33}\frac{\partial u(t,z_{\mathrm{Ag}})}{\partial z_{\mathrm{Ag}}} - 3\alpha' K T(t) = 0 \tag{6.8}$$

$$S_T(t) = c_{33}\frac{\partial u(t,z_{\mathrm{Ag}})}{\partial z_{\mathrm{Ag}}} \cong c_{33}\frac{u(t)}{d} \tag{6.9}$$

where, S_{ext} is the external stress, c_{33} (= 139 GPa) is the elastic constant [6.5, 6.7], $u(t, z_{\mathrm{Ag}})$ is the displacement of the normal direction in the Ag metal film, α' (= 3.1×10^{-5}) is the linear thermal expansion coefficient [6.8], and K (= 103 GPa) is the bulk modulus [6.7]. Equation (6.8) is based on the thermal elastic equation [6.6]. Here, the surface of the Ag metal film is in a free boundary from restraint. In addition, ablation does not occur because the temperature increase is too low. Therefore, it was assumed that the external stress is zero, as shown in Equation (6.8). The thermoelastic stress is obtained as Equation (6.9) because thermal equilibrium was assumed in the Ag metal film. As a result, the thermoelastic stress $S_T(t)$ and the displacement $u(t)$ are obtained by the following equations:

$$S_T(t) = 3\alpha' K T(t) \tag{6.10}$$

$$u(t) = \frac{d}{c_{33}} S_T(t) \tag{6.11}$$

The estimated thermoelastic stress is shown in Fig. 6.6. The peak value of the thermoelastic stress due to thermal expansion was estimated around 241 MPa. In addition, the peak value of displacement was estimated around 0.083 nm (0.15% of the film thickness).

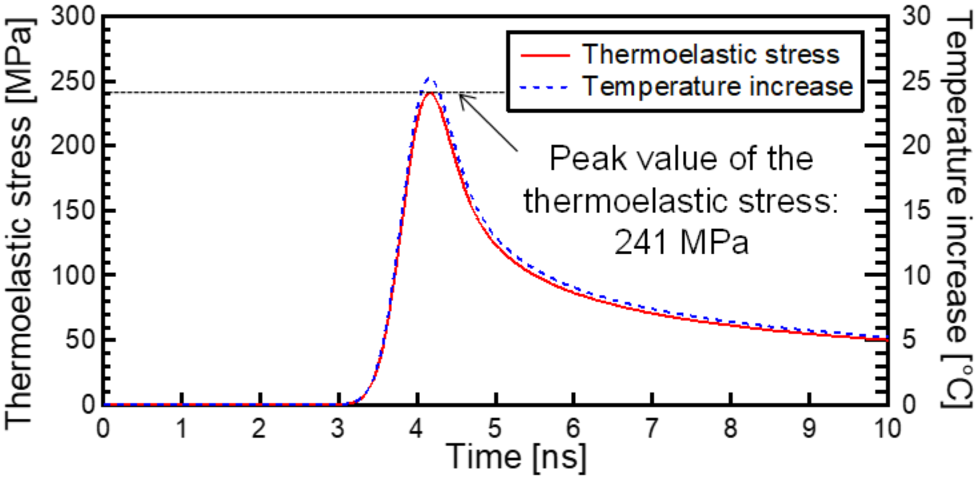

Fig. 6.6 Theoretical estimation of the thermoelastic stress and the temperature increase in the Ag metal film.

6.4 PERMITTIVITY CHANGE OF THE Ag METAL FILM

In the Fourth step, the change in the permittivity of the Ag metal film was theoretically estimated. The permittivity of the Ag metal film $\varepsilon_{\mathrm{Ag}}$ depends on the wavelength of the probe light. Then, well-known Drude theory was used assuming a Fermi liquid model to estimate $\varepsilon_{\mathrm{Ag}}$. This model can be used in the energy range of 0.1 – 3.0 eV because the interband transition of Ag exists near 3.8 eV (wavelength: 326 nm) [6.9]. Therefore, the use of this model is valid because the energy of the probe light was 2.33 eV (wavelength: 532 nm). Drude model is written as the following equations:

$$\varepsilon_{\mathrm{Ag}} = \varepsilon_{\infty} - \frac{\omega_{\mathrm{p}}^2}{\omega^2 + i\Gamma\omega} \tag{6.12}$$

$$\mathrm{Re}\left(\varepsilon_{\mathrm{Ag}}\right) \cong \varepsilon_{\infty} - \frac{\omega_{\mathrm{p}}^2}{\omega^2} \tag{6.13}$$

$$\mathrm{Im}\left(\varepsilon_{\mathrm{Ag}}\right) \cong \frac{\omega_{\mathrm{p}}^2}{\omega^3}\Gamma \tag{6.14}$$

where, ω is the angular frequency of the probe light, ε_{∞} is the sum of intraband contributions, ω_{p} is the plasma frequency, and Γ is the damping constant. The approximations of Equations (6.13) and (6.14) are valid in the case of $\Gamma \ll \omega$. As shown in Equations (6.13) and (6.14), the imaginary part depends on the ω_{p} and Γ, while the real part depends on the ε_{∞} and ω_{p}. The Drude parameters of ε_{∞}, ω_{p}, and Γ were modified to obtain the change in $\varepsilon_{\mathrm{Ag}}$ due to pump light irradiation. The modified Drude parameters are described in Subsections of 6.4.1, 6.4.2 and 6.4.3. Finally, the estimated permittivity is shown in Subsection 6.4.4.

6.4.1 SUM OF INTRABAND CONTRIBUTION ε_{∞}

First, the change in ε_{∞} due to the temperature increase is caused by the smearing of the Fermi distribution [6.10, 6.11, 6.12] and the shift in the Fermi level [6.12, 6.13]. The smearing of the Fermi distribution is caused by the broadening of the absorption band due to an increase in the electron temperature T_e. On the other hand, the shift in the Fermi level is caused by thermal expansion due to the increase in lattice temperature T_l. In 2010, Daniel et al. estimated experimentally the temperature and frequency dependencies of ε_{∞} in a Ag metal film deposited by EB evaporation, using pump probe spectroscopy with a femtosecond pulsed laser [6.14]. Their results were given by fitting using the two-temperature model, which considers the effects of both temperature increases of T_e and T_l [6.15]. Their results on the temperature dependence of ε_∞ were introduced in the modified model. The nonlinear behavior of ε_∞ was reported as:

$$\varepsilon_\infty = 3.94 + (0.7 + 3.0 \times 10^{-32}\omega^2) \times (1.5 \times 10^{-4}T_l + 4.3 \times 10^{-8}T_e^2). \qquad (6.15)$$

The electron temperature was assumed to be equal to the lattice temperature because the pulse duration of the laser was sufficiently slower than the thermal phonon vibration.

When the temperature of the Ag metal film increases 25 ºC, the increase of ε_∞ is estimated to be 0.0047. This change corresponds to 0.042% of the real part of $\varepsilon_{\mathrm{Ag}}$.

6.4.2 PLASMA FREQUENCY ω_p

ω_p is a function of the carrier density N and the effective electron mass m^*, which is written as:

$$\omega_\mathrm{p} = \sqrt{\frac{e^2N}{\varepsilon_\mathrm{v}m^*}} \qquad (6.16)$$

where, e is the elementary charge and ε_v is the permittivity in vacuum. Harsha et al. reported that the ω_p of Ag increases with increasing temperature. N generally decreases with increasing temperature because the volume increases due to thermal expansion. They, however, explained that the influence of decrease in m^* due to band transitions was larger than that of increase in N [6.16, 6.17, 6.18]. Sriharsha et al. also reported the same characteristics of ω_p [6.19]. In contrast, Sundari et al. reported the increase of ω_p with increasing temperature. They explained experimentally that ω_p increased due to the decrease of void fraction by Braggeman effective medium approximation (BEMA) [6.20]. Moreover, according to the report by Xu et al. in 2017 [6.21], a decrease in ω_p was expected with increasing temperature by first principle calculations. The decrease in ω_p with increasing temperature was confirmed experimentally in a Ag metal film by variable angle spectroscopic ellipsometry (VASE), explaining that the temperature characteristic of ω_p depended on the thermal expansion. Therefore, the strong effect of the thermoelastic stress due to the thermal expansion was considered in the modified model because voids were not clearly observed in the measured SPR sample through SEM. Using Equations of

(6.10) and (6.11), the change in ω_p is then given by the following equation:

$$\omega_\mathrm{p} \cong \sqrt{\frac{e^2}{\varepsilon_\mathrm{v} m^*}\left(\frac{N_0 d}{d+u(t)}\right)} = \omega_\mathrm{p0}\sqrt{\frac{d}{d+u(t)}} = \omega_\mathrm{p0}\sqrt{\frac{c_{33}}{c_{33}+S_T(t)}} \tag{6.17}$$

where, ω_{p0} (= 9.078 eV) and N_0 are the plasma frequency and carrier density at room temperature, respectively [6.14].

When the thermoelastic stress of 241 GPa, which is generated by the temperature increase of 25 °C, is induced, the increase in $-\omega_p^2/\omega^2$ is estimated to be 0.027. This change corresponds to 0.24% of the real part of ε_{Ag}. Moreover, the increase in $-\omega_p^2/\omega^2$ is 5 times larger than that of ε_∞. This means that the change in the real part of ε_{Ag} nearly depends on the change in ω_p. In other words, the real part of ε_{Ag} changes depending on the change in the film thickness due to the thermoelastic stress.

6.4.3 DAMPING CONSTANT Γ

In the modified model, the total of damping constant was expressed following the Mathiessen's rule [6.22, 6.23]. According to the rule, Γ depends on the sum of scattering rate from electron-electron $\Gamma_{e\text{-}e}$, electron-phonon $\Gamma_{e\text{-}ph}$, electron-surface Γ_s, electron-grain boundary Γ_{gb}, and electron-impurity Γ_{im}, which is written below:

$$\Gamma = \Gamma_\mathrm{e-e} + \Gamma_\mathrm{e-ph} + \Gamma_\mathrm{s} + \Gamma_\mathrm{gb} + \Gamma_\mathrm{im} \tag{6.18}$$

$\Gamma_{e\text{-}e}$ and $\Gamma_{e\text{-}ph}$ mean the intrinsic properties, while Γ_s, Γ_{gb}, and Γ_{im} mean the extrinsic collision rates. According to Lawrence [6.24], $\Gamma_{e\text{-}e}$ expresses the frequency dependence of Γ, which follows the equation:

$$\Gamma_\mathrm{e-e} = \frac{\pi^4 \Sigma\Delta}{6\hbar E_\mathrm{F}}\left[(k_\mathrm{B}T(t))^2 + \left(\frac{\hbar\omega}{2\pi}\right)^2\right] \tag{6.19}$$

where, k_B is the Boltzmann constant, $\hbar$ is the Planck constant, E_F (= 5.5 eV) is the Fermi energy [6.14], Σ is the constant giving the average of the scattering probability over the Fermi surface, and Δ is the fractional Umklapp scattering [6.25]. The value of ΣΔ is 0.097eV [6.19]. The temperature dependence of Γ mainly depends on $\Gamma_{e\text{-}ph}$, which increases as phonons increase, which results from increase in temperature because phonons follow Bose Einstein statistics. In the case of $E_F \gg \hbar\omega \gg k_B T$, $\Gamma_{e\text{-}ph}$ can be written using the Holstein's expression [6.26, 6.27],

$$\Gamma_{\mathrm{e-ph}} = \Gamma_0 \left[\frac{2}{5} + 4 \left(\frac{T(t)}{T_{\mathrm{D}}} \right)^5 \int_{\tau=0}^{\tau=\frac{T_{\mathrm{D}}}{T(t)}} \frac{\tau^4}{e^{\tau}-1} d\tau \right] \tag{6.20}$$

where, T_{D} (= 225.15 K) is the Debye temperature [6.28]. Γ_0 can be derived from $\Gamma_{\mathrm{e-ph}}$ at room temperature, which was 0.0296 eV [6.9]. Γ_{s} and Γ_{gb} can be expressed based on the Boltzmann transport equation, which are [6.29, 6.30, 6.31]:

$$\Gamma_{\mathrm{s}} = \Gamma_{\mathrm{e-ph}} \left\{ \left[1 - \frac{3l}{2(d+u(t))} \int_{h=1}^{h=\infty} (1-p) \left(\frac{1}{h^3} - \frac{1}{h^5} \right) \frac{1-exp\{-h(d+u(t))/l\}}{1-p\, exp\{-h(d+u(t))/l\}} dh \right]^{-1} - 1 \right\} \tag{6.21}$$

$$p = exp\left[- \left(\frac{4\pi r_{\mathrm{rms}}}{\lambda_{\mathrm{F}} h} \right)^2 \right] \tag{6.22}$$

$$\Gamma_{\mathrm{gb}} = \Gamma_{\mathrm{e-ph}} \left\{ \left[1 - \frac{3}{2}\alpha + 3\alpha^2 - 3\alpha^3 log\left(1 + \frac{1}{\alpha}\right) \right]^{-1} - 1 \right\} \tag{6.23}$$

$$\alpha = \frac{lR_e}{D(1-R_e)} \tag{6.24}$$

where, l (= 52 nm) is the intrinsic mean free path [6.32], p is the fraction of elastically scattered electrons at the film surface, λ_{F} (= 0.523 nm) is the de Broglie wavelength of electrons at the Fermi surface [6.28], r_{rms} is the root mean square roughness at the film surface, $R_{\mathrm{e}} = 0.25$ is the reflection coefficient of electron [6.33, 6.34], and D is the grain diameter. Equation (6.22) shows the effect of surface roughness on scattering [6.35]. In our study, the values of r_{rms} and D were measured by AFM and SEM. Γ_{im} was not introduced into the modified model because it is not significantly large to consider for the measured pure metal film sample [6.25].

When the temperature of the Ag metal film increases 25 ºC, the total damping constant Γ increases 0.0036 eV. This change corresponds to 4.3% of Γ. On the other hand, a 0.07% change in ω_{p} results from the temperature increase of 25 ºC. Therefore, the change in the imaginary part of $\varepsilon_{\mathrm{Ag}}$ mostly depends on the change in Γ. In addition, the change in $\Gamma_{\mathrm{e-ph}}$ composes 65% of the change in Γ. Moreover, the changes in Γ_{s} and Γ_{gb}, which depend on $\Gamma_{\mathrm{e-ph}}$, compose 34% of the change in Γ. The change in $\Gamma_{\mathrm{e-e}}$ composes only 1% of the change in Γ. This means that the change in imaginary part of $\varepsilon_{\mathrm{Ag}}$ mostly depends on the change in the scattering rate from phonon-electron $\Gamma_{\mathrm{e-ph}}$.

6.4.4 ESTIMATED PERMITTIVITY CHANGE

The estimated permittivity $\varepsilon_{\mathrm{Ag}}$ based on the modified model were Re($\varepsilon_{\mathrm{Ag}}$) = −11.18 and Im($\varepsilon_{\mathrm{Ag}}$) = 0.55 at room temperature. These values were in good agreement with the values of Re($\varepsilon_{\mathrm{Ag}}$) = −11.16 and Im($\varepsilon_{\mathrm{Ag}}$) = 0.57 obtained by fitting the measured reflectivity curve shown in Fig. 5.1. The estimated changes in $\varepsilon_{\mathrm{Ag}}$ due to the temperature increase and thermoelastic stress are shown in Fig. 6.7. 0.28% change in the real part was observed, whereas 4.1% change was observed in the imaginary part. As a result, the change in Re($\varepsilon_{\mathrm{Ag}}$) nearly depends on the change in ω_p due to the thermoelastic stress, while the change in Im($\varepsilon_{\mathrm{Ag}}$) depends on the change in $\Gamma_{\text{e-ph}}$ due to the temperature increase.

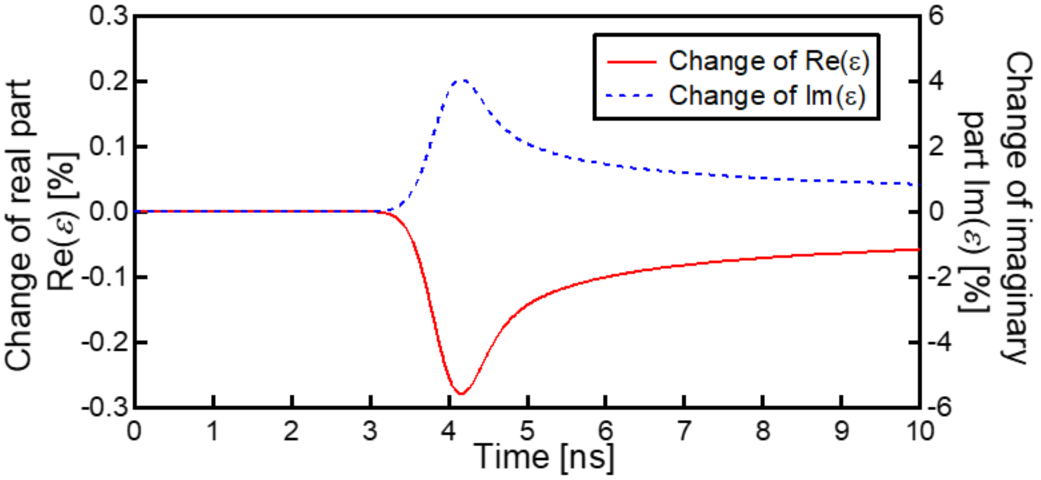

Fig. 6.7 Theoretical estimations of the changes in Re($\varepsilon_{\mathrm{Ag}}$) and Im($\varepsilon_{\mathrm{Ag}}$) of an Ag metal film caused by temperature increase and thermoelastic stress due to pump light irradiation.

6.5 REFLECTIVITY CHANGE DUE TO PUMP LIGHT IRRADIATION

In the fifth step, the reflectivity change $\Delta R = R - R_0$ due to pump light irradiation was estimated based on the well-known multiple reflection model, which is described in the following equation:

$$\Delta R = R - R_0 = \left| \frac{r_{\mathrm{BK7-Ag}} + r_{\mathrm{Ag-Air}} exp[2ik_z(d+u(t))]}{1 + r_{\mathrm{BK7-Ag}} r_{\mathrm{Ag-Air}} exp[2ik_z(d+u(t))]} \right|^2 - R_0 \tag{6.25}$$

where, R_0 is the reflectivity at room temperature, k_z is the wave vector in the direction of the film depth in the Ag metal film, $r_{\mathrm{BK7-Ag}}$ is the reflectivity at the interface between the BK7 glass prism and Ag metal film, and $r_{\mathrm{Ag-Air}}$ is the reflectivity at the interface between the Ag metal film and air. Detailed explanation of R_0 is described in Subsection 3.2.3. Here, $r_{\mathrm{BK7-Ag}}$ and $r_{\mathrm{Ag-Air}}$ are described in the following equations:

$$r_{\mathrm{BK7-Ag}} = \frac{\sqrt{\varepsilon_{\mathrm{BK7}}}\cos\theta'_{\mathrm{Ag}} - \sqrt{\varepsilon_{\mathrm{Ag}}}\cos\theta_{\mathrm{BK7}}}{\sqrt{\varepsilon_{\mathrm{BK7}}}\cos\theta'_{\mathrm{Ag}} + \sqrt{\varepsilon_{\mathrm{Ag}}}\cos\theta_{\mathrm{BK7}}} \tag{6.26}$$

$$r_{\mathrm{Ag-Air}} = \frac{\sqrt{\varepsilon_{\mathrm{Ag}}}\cos\theta'_{\mathrm{Air}} - \sqrt{\varepsilon_{\mathrm{Air}}}\cos\theta'_{\mathrm{Ag}}}{\sqrt{\varepsilon_{\mathrm{Ag}}}\cos\theta'_{\mathrm{Air}} + \sqrt{\varepsilon_{\mathrm{Air}}}\cos\theta'_{\mathrm{Ag}}} \tag{6.27}$$

$$\theta'_{\mathrm{Ag}} = \cos^{-1}\sqrt{1 - \frac{\varepsilon_{\mathrm{BK7}}}{\varepsilon_{\mathrm{Ag}}}\sin^2\theta_{\mathrm{BK7}}} \tag{6.28}$$

$$\theta'_{\mathrm{Air}} = \cos^{-1}\sqrt{1 - \frac{\varepsilon_{\mathrm{BK7}}}{\varepsilon_{\mathrm{Air}}}\sin^2\theta_{\mathrm{BK7}}} \tag{6.29}$$

where, $\varepsilon_{\mathrm{BK7}}$, $\varepsilon_{\mathrm{Ag}}$, and $\varepsilon_{\mathrm{Air}}$ are the permittivities of the BK7 glass prism (1.519), the Ag metal film, and the air (1.0), respectively. θ_{BK7} is the incident angle of the probe light to the BK7 glass prism. θ'_{Ag} and θ'_{Air} are the refraction angles in the Ag metal film and air, respectively. The wave vector in the direction of the film depth in the Ag metal film is described below:

$$k_z = \sqrt{\varepsilon_{\mathrm{Ag}}\left(\frac{\omega}{c_{\mathrm{v}}}\right)^2 - k_{\mathrm{ev}}^2} \tag{6.30}$$

$$k_{\mathrm{ev}} = k_x = \frac{\omega}{c_{\mathrm{v}}}\sqrt{\varepsilon_{\mathrm{Ag}} - \varepsilon_{\mathrm{Ag}} cos^2\theta'_{\mathrm{Ag}}} \tag{6.31}$$

where, c_{v} is the light velocity in vacuum. k_{ev} is the wave number of the evanescent wave (EVW). When the incident probe light with *p*-polarization irradiates the metal film from the BK7 glass prism, evanescent waves are excited at the surface of the metal film. SPR occurs when the momentum matches the wave vectors of the EVW k_{ev} and the SPW k_{sp}.

6.6 CONVOLUTION PROCESS

The actual reflectivity changes are obtained as the absolute value of the convolution result using the profile of probe light pulse by the pump probe measurement. Because of it, deconvolution techniques were also studied in order to obtain the original transient response without the need of theoretical fitting [6.36, 6.37]. However, the signal processing needed to perform the deconvolution is very difficult. Thus, for precise estimations, the reflectivity change as the convolution result should be estimated based on the constructed theory. As a result, the absolute value of the convolution result $|\Delta R'|$ was estimated as below:

$$|\Delta R'(t)| = \left| \frac{\int_{\tau=-\infty}^{\tau=\infty} \Delta R(\tau) I(t-\tau)\, d\tau}{\int_{\tau=-\infty}^{\tau=\infty} I(\tau)\, d\tau} \right| \tag{6.32}$$

Here, the reflectivity change $\Delta R(t)$ given by the Equation (6.25) and the convolution result $|\Delta R'(t)|$ are shown in Fig. 6.8. These data were estimated in the case where the incident angle of the probe light was $\theta_r + 0.18°$. As can be seen in Fig. 6.8, the peak value decreased compared with the original reflectivity change. In addition, the time width of the transient response broadened.

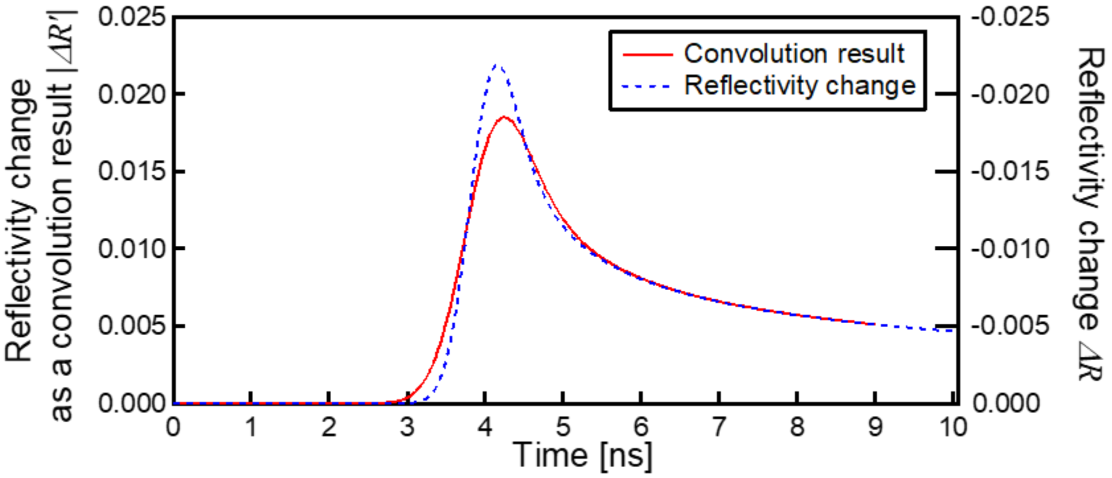

Fig. 6.8 Reflectivity change ΔR and the convolution result $|\Delta R'|$.

REFERENCES

[6.1] P. Winsemius, F. F. van Kampen, H. P. Lengkeek, and C. G. van Went, "Temperature dependence of the optical properties of Au, Ag and Cu", J. Phys. F: Metal Phys., vol. 6, no. 8, pp. 1583–1606, 1976.

[6.2] Ľ. Kubiĉár, V. Vretenár, and U. Hammerschmidt, "Thermophysical parameters of optical glass BK 7 measured by the pulse transient method", Int. J. Thermophys., vol. 26, no. 2, pp. 507–518, Mar. 2005.

[6.3] A. Jain and A. J. H. MacGaughey, "Thermal transport by phonons and electrons in aluminum, silver, and gold from first principles", Phys. Rev. B, vol. 93, no. 081206, Feb. 2016.

[6.4] J. W. Arblaster, "Thermodynamic properties of silver", J. Phase Equil. Diff., vol. 36, no. 6, pp. 573–591, Sep. 2015.

[6.5] O. L. Anderson, "Determination and some uses of isotropic elastic constants of polycrystalline aggregates using single-crystal data" in Physical Acoustics, New York:Academic, vol. 3B, p. 43, 1965.

[6.6] C. B. Scruby, L. E. Drain, Laser Ultrasonics: Techniques and Applications, New York:Adam Hilger, 1990.

[6.7] B. Lehr, H. Ulrich, and O. Weis, "Hypersound attenuation and phase velocities in evaporated polycrystalline films of silver, copper and constantan between 1 and 24 GHz", Condens. Matter, vol. 48, pp. 23–30, Apr. 1982.

[6.8] Y. Zoo, D. Adams, J. W. Mayer, and T. L. Alford, "Investigation of coefficient of thermal expansion of silver thin film on different substrates using X-ray diffraction", Thin Solid Films, vol. 513, pp. 170–174, Aug. 2006.

[6.9] H. U. Yang, J. D'Archangel, M. L. Sundheimer, E. Tucher, G. D. Boreman, and M. B. Raschke, "Optical dielectric function of silver", Phys. Rev. B, vol. 91, no. 235137, June 2015.

[6.10] R. Rosei, "Temperature modulation of the optical transitions involving the Fermi surface in Ag: Theory", Phys. Rev. B, vol. 10, no. 2, July 1974.

[6.11] R. Rosei, "Temperature modulation of the optical transitions involving the Fermi surface in Ag: Experimental", Phys. Rev. B, nol. 10, no. 2, July 1974.

[6.12] R. H. M. Groeneveld, R. Sprik, and A. Lagendijk, "Ultrafast relaxation of electrons probed by surface plasmons at a thin silver Film", Phys. Rev. Lett., vol. 64, no. 7, pp. 784–787, Feb. 1990.

[6.13] P. Winsemius, F. F. van Kampen, H. P. Lengkeek, C. G. van Went, "Temperature dependence of the optical properties of Au Ag and Cu", J. Phys. F Metal Phys., vol. 6, no. 8, pp. 1583–1606, 1976.

[6.14] D. T. Owens, C. Fuentes-Hernandez, J. M. Hales, J. W. Perry, and B. Kippelen, "A comprehensive analysis of the contributions to the nonlinear optical properties of thin Ag films", J. Appl. Phys., vol. 107, no. 123114, Apr. 2010.

[6.15] L. Guo, S. L. Hodson, T. S. Fisher, and X. Xu, “Heat transfer across metal-dielectric interfaces during ultrafast-laser heating”, J. Heat Transfer, vol. 134, no. 042402, 2012.

[6.16] H. Reddy, U. Guler, K. Chaudhuri, A. Dutta, A. V. Kildishev, V. M. Shalaev, and A. Boltasseva, "Temperature-dependent optical properties of single crystalline and polycrystalline silver thin films", ACS Photon., vol. 4, no. 5, pp. 1083–1091, Apr. 2017.

[6.17] V. Z. Kresin and G. O. Zaĭtsev, "Temperature dependence of the electron specific heat and effective mass", Sov. Phys. JETP, vol. 47, no. 5, pp. 983–989, May 1978.

[6.18] C-Y. Young, "The frequency and temperature dependence pf the optical effective mass of conduction electrons in simple metals", J. Phys. Chem. Solids, vol. 30, no. 12, pp. 2765–2769, Dec. 1969.

[6.19] S. V. Jayanti, J. H. Park, A. Dejneka, D. Chvostova, K. M. McPeak, X. Chen, S-H. Oh, and D. J. Norris, "Low-temperature enhancement of plasmonic performance in silver films", Opt. Mater. Express, vol. 5, no. 5, pp. 1147–1155, Mar. 2015.

[6.20] S. T. Sundari, S. Chandra, and A. K. Tyagi, "Temperature dependent optical properties of silver from spectroscopic ellipsometry and density function theory calculations", J. Appl. Phys., vol. 114, no. 033515, June 2013.

[6.21] M. Xu, J-Y. Yang, S. Zhang, and L. Liu, "Role of electron-phonon coupling in finite-temperature dielectric functions of Au, Ag, and Cu", Phys. Rev. B, vol. 96, no. 115154, Sep. 2017.

[6.22] R. C. Munoz, and C. Arenas, "Size effects and charge transport in metals: Quantum theory of the resistivity of nanometric metallic structures arising from electron scattering by grain boundaries and by rough surfaces", Appl. Phys. Rev, vol.4, no. 011102, Nov. 2016.

[6.23] S. Zhang, Y. Pei, and L. Liu, "Dielectric function of polycrystalline gold films: Effects of grain boundary and temperature", J. Appl. Phys., vol. 124, no. 165301, Sep. 2018.

[6.24] W. E. Lawrence, "Electron-electron scattering in the low-temperature resistivity of the noble metals", Phys. Rev. B, vol. 13, no. 12, pp. 5316–5319, June 1976.

[6.25] R. T. Beach and R. W. Christy, "Electron-electron scattering in the intraband optical conductivity of Cu, Ag, and Au", Phys. Rev. B, vol. 16, no. 12, pp. 5277–5284, Dec. 1977.

[6.26] J. A. McKay and J. A. Rayne, "Temperature dependence of the infrared absorptivity of the noble metals", Phys. Rev. B, vol. 13, no. 2, pp. 673–685, Jan. 1976.

[6.27] H. P. Chiang, P. T. Leung, and W. S. Tse, "Optical properties of composite materials at high temperatures", Solid State Commun., vol. 101, no. 1, pp. 45–50, Sep. 1996.

[6.28] C. Kittel, Introduction to Solid-State Physics, New York, NY, USA:Wiley, 2012.

[6.29] E. H. Sondheimer, "The mean free path of electrons in metals", Adv. Phys., vol. 1, no. 1, pp. 1–42, Jan. 1952.

[6.30] A. F. Mayadas and M. Shatzkes, "Electrical-resistivity model for polycrystalline films: the case of arbitrary reflection at external surfaces", Phys. Rev. B, vol.1, no. 4, pp. 1382–1389, Feb. 1970.

[6.31] D. I. Yakubovsky, A. V. Arsenin, y. V. Stebunov, D. Y. Fedyanin, and V. S. Volkov, "Optical constants and structural properties of thin gold films", Opt. Express, vol.25, no. 21, pp. 25574–2587, Sep. 2017.

[6.32] F. W. Reinhold and G. R. Stilwell, "Mean free paths of electrons in evaporated metal films", Phys. Rev., vol. 88, no.2, pp. 418–419, Oct. 1952.

[6.33] E. I. Tochitskii and N. M. Belyavskii, "Grain-boundary electron scattering effect on metal film resistivity" Phys. Status Solidi A, vol.61, no. 1, pp. K21–K24, Sep. 1980.

[6.34] Y. Jiang, S. Pillai, and M. A. Green, "Grain boundary effects on the optical constants and Drude relaxation times of silver films", J. Appl. Phys., vol. 120, no. 233109, Dec. 2016.

[6.35] S. B. Soffer, "Statistical model for the size effect in electrical conduction", J. Appl. Phys., vol. 38, no. 4, pp. 1710–1715, Mar. 1967.

[6.36] E. Keszei, "Efficient model-free deconvolution of measured femtosecond kinetic data using a genetic algorithm", J. Chemometrics, vol. 23, no. 188, Dec. 2008.

[6.37] N. E. Henriksen and V. Engel, “On the deconvolution of the temporal width of laser pulses from pump–probe signals”, J. Chem. Phys., vol. 111, no. 23, Sep. 1999.

7. MECHANISM OF THE SUB-NANOSECOND PUMP PROBE RESPONSE UNDER SPR

The experimental investigation results of the pump probe response under SPR were described in Chapter 5. The transient reflectivity changes were measured by the pump probe system with the straightforward probe light to investigate in detail. As a result, it was confirmed that the changes were resulted from the broadening of SPR curve and the shift in SPR angle. Moreover, the theoretical model of the pump probe response under SPR was explained in Chapter 6. The objective of this chapter is to explain the investigation results and to discuss the mechanism of the sub-nanosecond pump probe responses under SPR. In Section 7.1, comparison results between the experimental results and the theoretical estimations are shown to confirm the validity of the constructed theoretical model. In Section 7.2, discussion on the mechanism of the pump probe response under SPR is given based on the comparison results described in Section 7.1. Finally, the application possibility as an evaluation method for SPR sensors is discussed in Section 7.3.

7.1 COMPARISON OF EXPERIMENTAL MEASUREMENT AND THEORETICAL ESTIMATION

SPR occurs when the momentums of the wave vectors of EVW k_{ev} and SPW k_{sp} matches. Reflectivity drastically decreases in SPR condition. Generally, the matching is attained by manipulating the incident angle of the probe light because k_{ev} is a function of the incident angle. Therefore, the SPR characteristic is easily confirmed by measuring the incident angle dependence of the reflectivity. In addition, the transient thermoelastic stress was induced as the time response in the pump probe. Therefore, to confirm the validity of the constructed theoretical model, the incident angle dependence of the maximum reflectivity change $|\Delta R'(\theta_{\mathrm{BK7}})|$ and the time responses $|\Delta R'(t)|$ were compared between the experimental results and the theoretical estimations.

First, the incident angle dependence of the maximum reflectivity change $|\Delta R'(\theta_{\mathrm{BK7}})|$ was measured to compare with the theoretical estimations. The measured incident angle dependence of the reflectivity change is represented by red circles in Fig. 7.1. The measured reflectivity without the irradiation of the pump light R is also plotted using the blue circles. The horizontal axis is the angle difference from the SPR angle θ_{r} without the irradiation of the pump light.

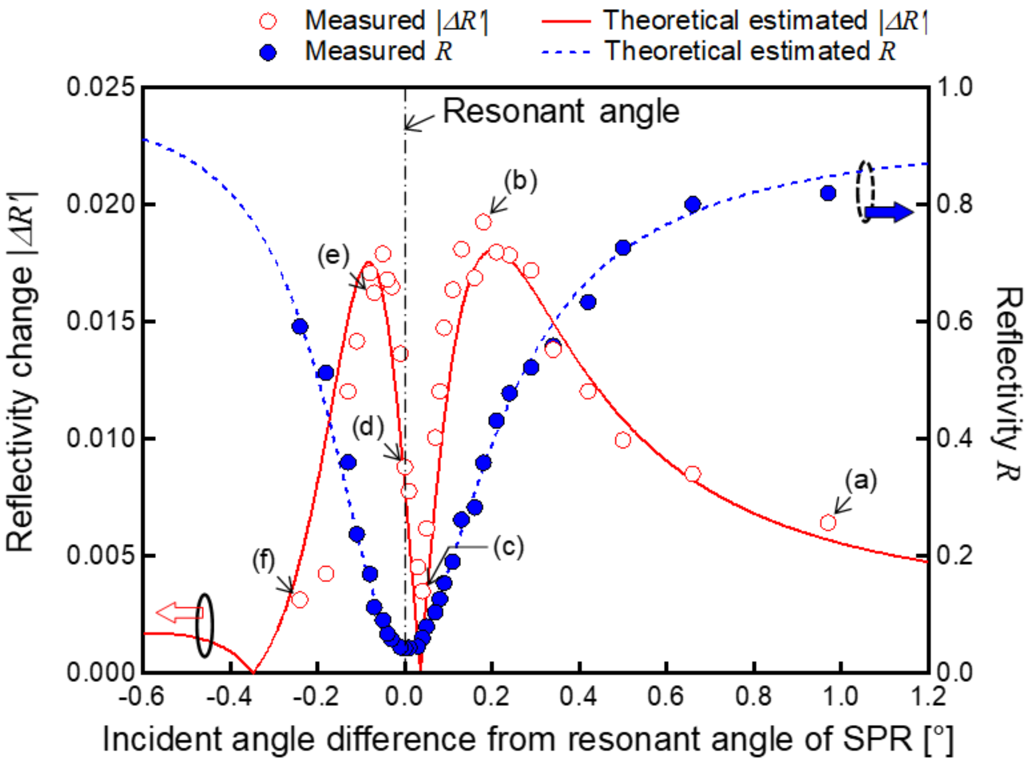

Fig. 7.1 Maximum reflectivity change plotted as a function of the incident angle. Measured reflectivity changes are represented by red circles. Measured reflectivities at room temperature are represented by blue circles. Theoretical estimations of the reflectivity and its change are shown as dashed and solid lines, respectively.

Two major changes in the reflectivity |ΔR'| were 0.018 and 0.019 at the angles around θ_r – 0.06° and θ_r + 0.18°, respectively. The angle in which the change in reflectivity shifts from positive to negative values occurs around θ_r + 0.04°. Here, the coefficient of determination between the measured SPR curve and the theoretical estimation was confirmed as a fit index, which was 0.99. Therefore, the estimated reflectivity curve at room temperature was in good agreement with the measured data without the irradiation of the pump light. Moreover, the coefficient of determination between the measured reflectivity change |ΔR'| and the theoretical estimations was also confirmed, which was 0.78. The tendency of the estimated reflectivity change |ΔR'| was also in good agreement with the experimental data.

Next, the time responses |ΔR'(t)| were measured in the pump probe by the sub-nanosecond pulsed laser at each incident angle which corresponds to the angle marked in Fig. 7.1. The measured time responses are plotted as a function of incident angle in Figs. 7.2 (a) – (f). (b) and (e) are the angles where the reflectivity changed maximally, (c) is the angle where the reflectivity changed from positive to negative, and (d) is the resonant angle. Theoretically estimated responses are shown as solid black lines. Here, the coefficients of determination between the measured time responses and the theoretical estimations were confirmed in the time region of 3.3 – 9.0 ns when the time responses appear. The coefficients of determination at the incident angles of (a), (b), (c), (d), (e) and (f) were 0.94, 0.97, 0.29, 0.96, 0.96 and 0.70, respectively. The coefficient of determination at the angle of (c) was not in good agreement. This is because the accuracy of the angle in the measurement system was not better than ±0.01°. However, other time responses were in good agreement with the theoretical estimations.

As a result, these comparison results between the experiments and the theoretical estimations show the validity of the constructed theoretical model.

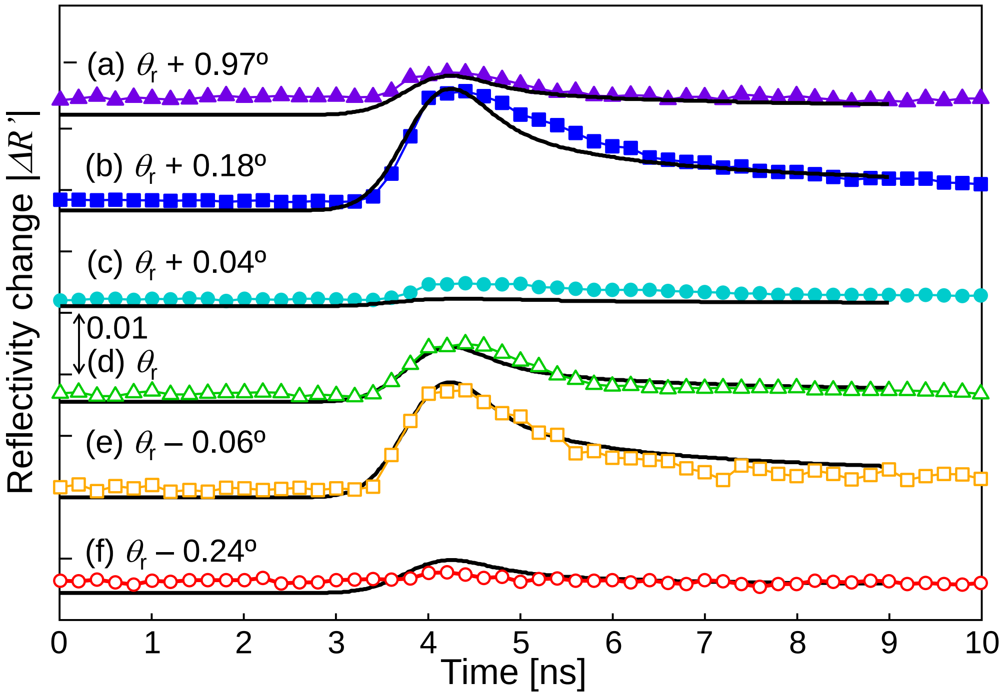

Fig. 7.2 Time responses observed by the sub-nanosecond pump probe system at incident angles of (a) $\theta_r + 0.97^o$, (b) $\theta_r + 0.18^o$, (c) $\theta_r + 0.04^o$, (d) θ_r, (e) $\theta_r - 0.06^o$, and (f) $\theta_r - 0.24^o$. Theoretical estimations at different incident angles are also drawn as solid black lines. θ_r is the resonant angle of SPR and the incident angles (a) – (f) correspond to the angles marked in Fig. 7.1.

7.2 FACTORS OF THE REFLECTIVITY CHANGE

The measured data |Δ*R*'| was from the convolution of the probe light pulse and the reflectivity change Δ*R*. Then, the original reflectivity changes Δ*R* were estimated using the constructed theoretical model. Figure 7.3 (a) and (b) shows the theoretically estimated time response of the reflectivity change as a function of the incident angle. Figure 7.4 (a) also shows the incident angle dependence of the maximum reflectivity change. The time when the reflectivity changed maximally is 4.2 ns, indicated by (G) in Fig. 7.3 (b). The SPR curves without the irradiation of the pump light and with the irradiation of the pump light, *R* and *R*', respectively, are also plotted in Fig. 7.4 (a). The reflectivity increased at around θ_r – 0.08°, while it decreased around θ_r + 0.20°. In addition, the reflectivities at lower and higher angles decreased slightly. As shown in the SPR curves in Fig. 7.4 (a), this tendency seemed to result from two influences, the shift in the SPR angle and broadening of the SPR curve. Figure 7.4 (b) shows the enlarged graph in Fig. 7.4 (a) near the SPR angle. As shown in Fig. 7.4 (b), the SPR angle shifted to higher angle by approximately 0.008°. Figure 7.5 shows the relative reflectivity Δ*R*/*R*, which changed dramatically at an angle slightly less than the SPR angle. The maximum value was estimated to attain up to 30% because the reflectivity near the SPR angle was very low.

As shown in Figs. 7.3 and 7.4, the change in reflectivity was mostly affected by the shift in the SPR angle, which should be carefully understood. The shift in the SPR angle occurs by the change in dispersion relation of SPW (this relation is described in detail in Subsection 3.2.1), which is written as:

$$\mathrm{Re}(k_{\mathrm{sp}}) = \frac{\omega}{c_{\mathrm{v}}}\left[\frac{\mathrm{Re}(\varepsilon_{\mathrm{Ag}})\varepsilon_{\mathrm{Air}}}{\mathrm{Re}(\varepsilon_{\mathrm{Ag}})+\varepsilon_{\mathrm{Air}}}\right]^{\frac{1}{2}} \tag{7.1}$$

The shift in the SPR angle mainly resulted from the change in the plasma frequency in the Ag metal film due to thermal expansion. This is because the change in Re($\varepsilon_{\mathrm{Ag}}$) mostly depends on the change in the plasma frequency. This result supports the latest report of Ag film by Xu et al. [7.1] indicating that the plasma frequency decreases with thermal expansions due to the increasing temperature. Alternatively, the broadening of the SPR curve occurs by the increase in the attenuation of SPW (this relation is also described in detail in Subsection 3.2.1), which is written as:

$$\mathrm{Im}(k_{\mathrm{sp}}) = \frac{\omega}{c_{\mathrm{v}}}\left[\frac{\mathrm{Im}(\varepsilon_{\mathrm{Ag}})}{2\{\mathrm{Re}(\varepsilon_{\mathrm{Ag}})\}^2}\right]\left[\frac{\mathrm{Re}(\varepsilon_{\mathrm{Ag}})\varepsilon_{\mathrm{Air}}}{\mathrm{Re}(\varepsilon_{\mathrm{Ag}})+\varepsilon_{\mathrm{Air}}}\right]^{\frac{3}{2}} \tag{7.2}$$

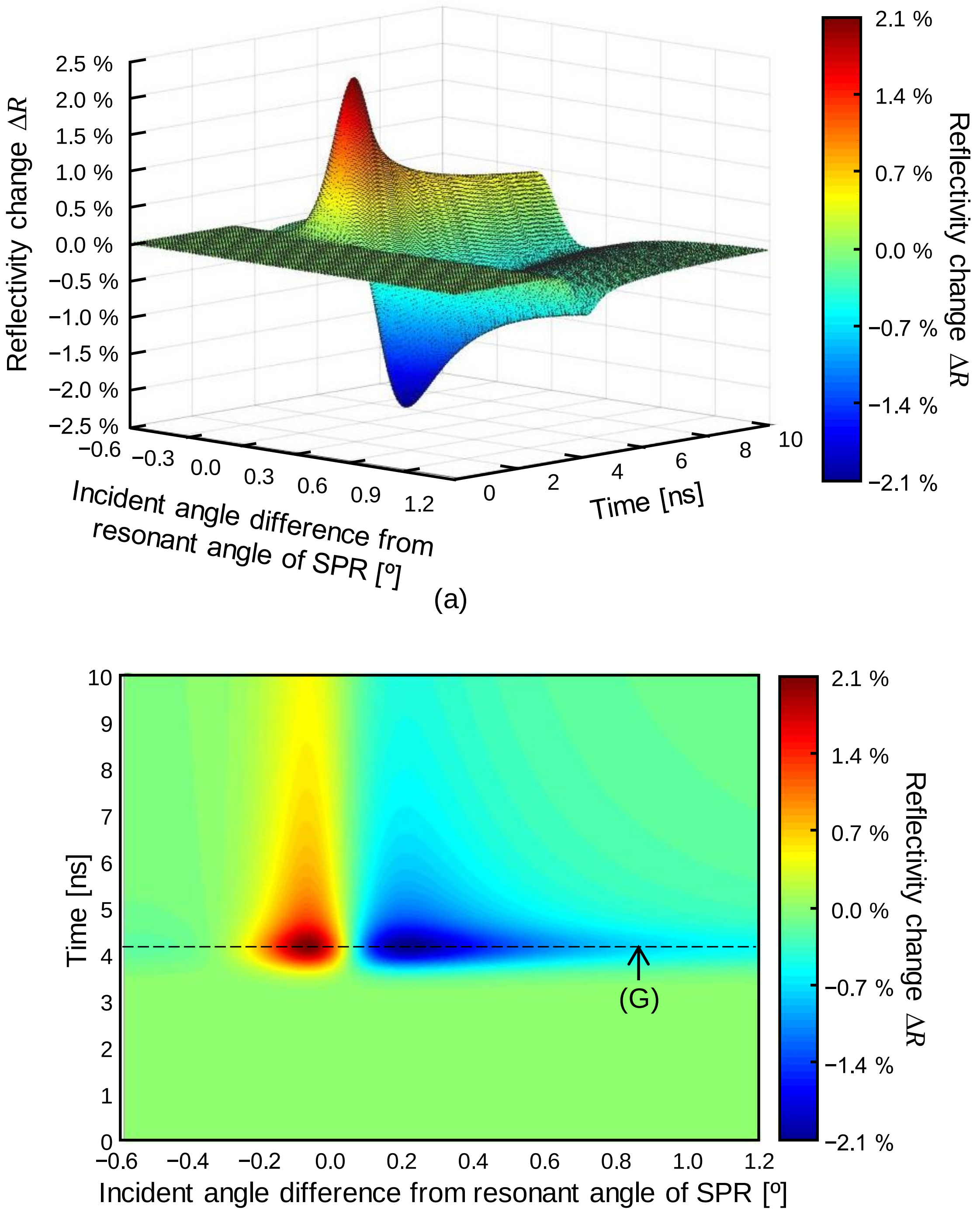

(a)

(b)

Fig. 7.3 Theoretical estimation of the time responses of original reflectivity change plotted as a function of the incident angle and the time. (a) is the 3D view and (b) is the flat view. (G) is the time when the reflectivity changes maximally, which is 4.2 ns.

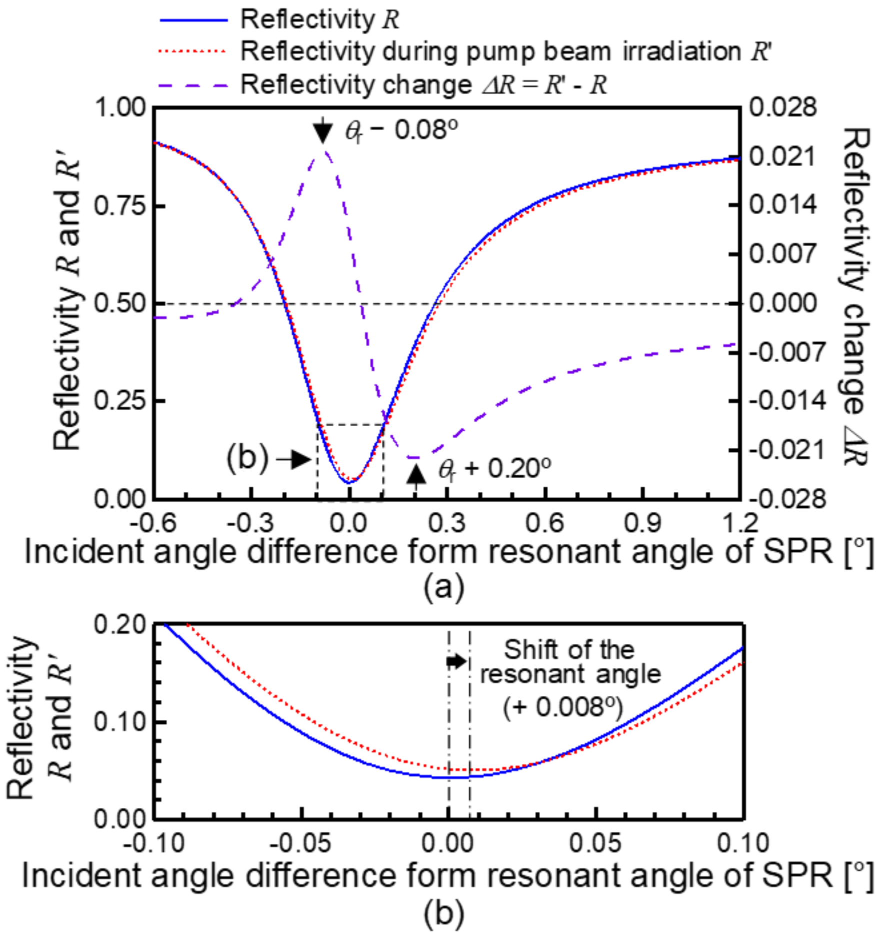

Fig. 7.4 Theoretical estimations of the SPR curves. The reflectivity before the pump light irradiation is drawn as solid blue line. The reflectivity after changing due to the pump light irradiation at time (G) shown in Fig. 7.3 (b) is drawn as dotted red line. The reflectivity change is drawn as dashed purple line. (b) The enlarged view of the reflectivity curves near the resonant angle of SPR.

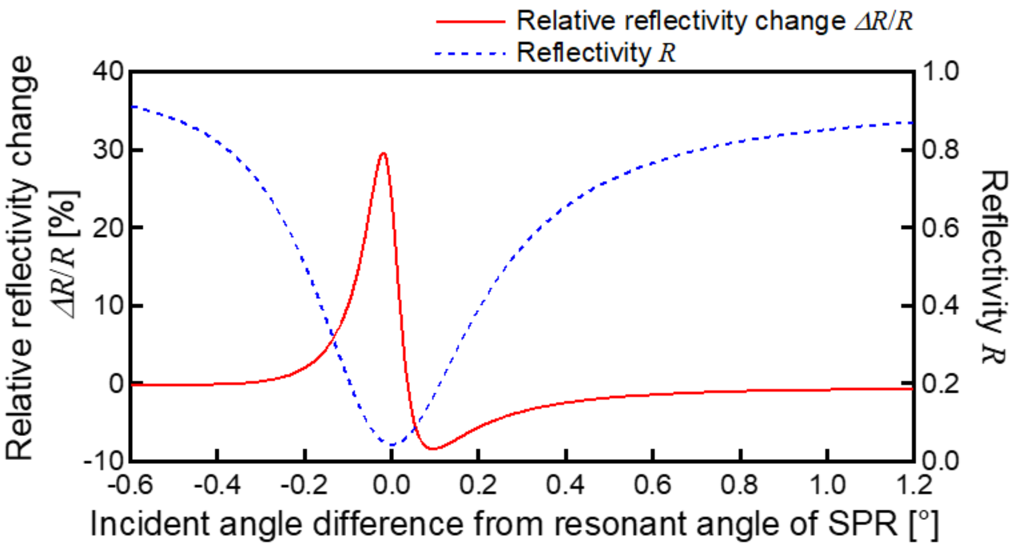

Fig. 7.5 Relative change in the original reflectivity plotted as a function of incident angle at the time (G) shown in Fig. 7.3 (b). The reflectivity curve at room temperature is drawn as dashed blue line.

Therefore, the broadening of the SPR curve mainly resulted from the change in the damping constant of the Ag metal film due to temperature rise. The change in Im($\varepsilon_{\mathrm{Ag}}$) nearly depends on the damping constant. The change in the damping constant corresponds to the change in the electron-phonon scattering rate in the Ag metal film. Thus, the SPR curve broadens by the increase in the electron-phonon scattering rate in the Ag metal film. Yeshchenko et al. explained this with the idea of the local SPR [7.2] using the temperature dependence of SPR broadening of a Ag metal nano-particle from the measurements of the absorption spectra and the theoretical model. The experimental measurements and theoretical estimations in this study also presented similar behaviors. In conclusion, in the pump probe measurements with sub-nanosecond laser light pulses, the shift in SPR angle was attributed to the thermal expansion due to the thermoelastic stress, whereas the broadening of the SPR curve was likely caused by the change in the electron-phonon scattering rate due to the temperature increase.

Here, the influences on the reflectivity change shown in Fig. 7.4 by the changes in the real and imaginary parts of the permittivity of Ag metal film is discussed. Theoretical estimations of the reflectivity curves considering each change in the real and imaginary parts of the permittivity are shown in Fig. 7.6. As can be seen in Fig. 7.6, the influences of the shift in the SPR angle and the broadening of the SPR curve are confirmed in the tendency of the reflectivity change plotted as a function of the incident angle. Actually, when only real part of the permittivity of Ag metal film changes, two major changes in the reflectivity exist at angles around $\theta_r - 0.12^\circ$ and $\theta_r + 0.14^\circ$ due to shift in the SPR angle. In contrast, when only imaginary part of the permittivity changes, one major change in the reflectivity exists at the SPR angle due to the SPR curve broadening. In addition, the major change in the reflectivity by the change in the imaginary part is 0.9%, while that by the change in the real part is 2.2%. As a result, the reflectivity change due to the change in the real part is larger than twice of the reflectivity change due to the change in the imaginary part despite the small change in the plasma frequency.

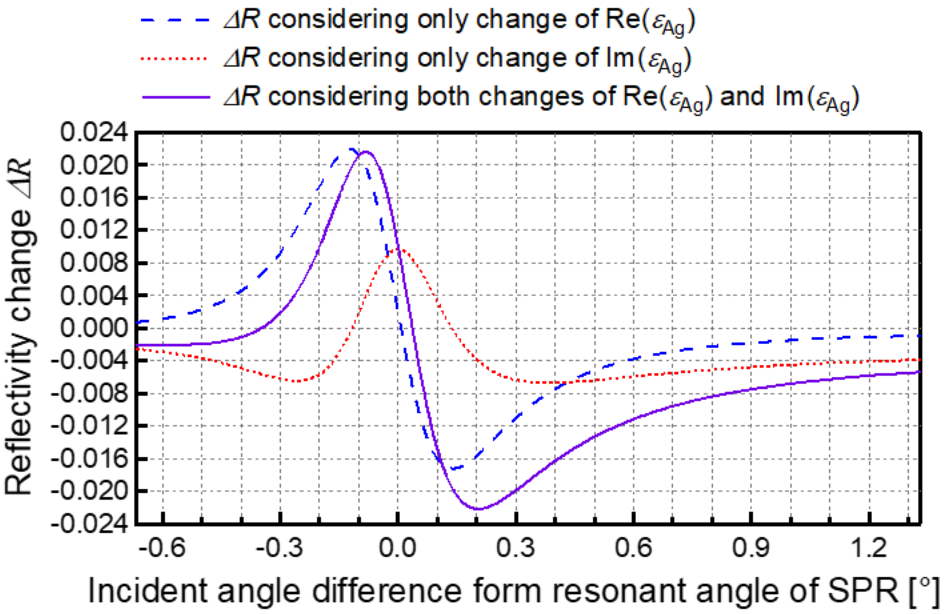

Fig. 7.6 Theoretical estimations of the reflectivity curves considering each change in real and imaginary parts of the permittivity of Ag metal film. The reflectivity change plotted as a function of incident angle at the time (G) shown in Fig. 7.3 (b), considering only the change in Re($\varepsilon_{\mathrm{Ag}}$), is drawn as dashed blue line. The reflectivity considering only the change in Im($\varepsilon_{\mathrm{Ag}}$) is drawn as dotted red line. The reflectivity change considering both changes in Re($\varepsilon_{\mathrm{Ag}}$) and Im($\varepsilon_{\mathrm{Ag}}$) is drawn as solid purple line.

7.3 APPLICATION POSSIBILITY AS AN EVALUATION METHOD FOR SPR SENSORS

From the investigations by experimental and theoretical approaches, the mechanism of the transient response under SPR measured by a sub-nanosecond pump probe technique is explained in detail. The transient response was caused by the changes in the permittivity of the metal film used for the excitation of SPR. Here, the change in the real part shifted the SPR angle and that of the imaginary part broadened the SPR curve. Especially, in the case of the SPR sample with Ag metal film, the influence on the reflectivity change by the change in the real part was larger than that of the imaginary part. The change in the real part came from the change in the plasma frequency, which was caused by the thermoelastic stress. In contrast, the change in the imaginary part came from the change in the damping constant, which was caused by the temperature increase.

Here, the changes in the real and imaginary parts of the permittivity of the metal film can be determined by a variable angle spectroscopy of the sub-nanosecond pump probe near the SPR angle and the theoretical fitting. Moreover, the temperature increase can be estimated from the change of the imaginary part because the change of the imaginary part is a function of temperature mostly. Moreover, the thermal expansion also can be estimated if the thermal expansion coefficient of the metal film is known in advance. Therefore, the sub-nanosecond pump probe spectroscopy has a possibility to be used as an evaluation method of the change of the optical property due to the temperature increase and the thickness deformation of the metal film.

This spectroscopy technique also has a possibility to evaluate the elasticity of a metal film with known thermal expansion coefficient if a glass prism with known thermal properties is used. The temperature increase depended on the thermal conductivity and the thermal diffusion coefficient of the glass prism used because the energy of the transmitted pump light was nearly absorbed in the metal film such that it attained thermal equilibrium during the pump light irradiation. This was because the pulse duration of the laser was long enough to attain thermal equilibrium condition. On the other hand, the generated thermoelastic stress depended on the elastic constant and the thermal expansion coefficient of the metal film used. Therefore, the combination of the sub-nanosecond pump probe spectroscopy and the theoretical fitting has a possibility to be used as an evaluation method of elasticity of a metal film.

By this spectroscopy technique, the measurement of the elasticity and the change of optical property as the transient response in sub-nanosecond region is expected, which is an important property for SPR ultrasonic sensors used in high-resolution PAM systems.

REFERENCES

[7.1] M. Xu, J-Y. Yang, S. Zhang, and L. Liu, "Role of electron-phonon coupling in finite-temperature dielectric functions of Au, Ag, and Cu", Phys. Rev. B, vol. 96, no. 115154, Sep. 2017.

[7.2] O. A. Yeshchenko, I. S. Bondarchuk, A. A. Alexeenko, and A. V. Kotko, "Temperature dependence of the surface plasmon resonance in silver nanoparticles", Functional Materials, vol. 20, no. 3, pp. 357–365, 2013.

8. CONCLUSIONS

All results and discussions in this study are summarized below:

The pump probe system with a sub-nanosecond pulsed laser was developed, which was composed of the laser stated, a polarization variable attenuator, a three round-trip automatic delay line, a second harmonic generator, a differential detection system, and a lock-in measurement system. The transient response was observed using a Au/Cr bimetal sample to demonstrate the system developed. Consequently, it was confirmed that the system enabled the observation of the transient response due to the irradiation of the sub-nanosecond pulsed laser.

To measure the transient response under SPR, the system was improved. In addition, a SPR sample with Kretschmann configuration consisted of a Ag metal film and a BK7 glass prism was prepared. First, the pump probe system with the focused probe light was prepared to simply measure the transient responses in the entire incident angle regions where SPR occurred. Through measurements that involved changing the polarization of the probe light, the transient response caused by the pump light irradiation clearly appeared using the probe light with the p-polarization (SPR condition), while no signal appeared using the probe light with the s-polarization (non-SPR condition). As a result, it was confirmed that the response as a reflectivity change in the SPR condition became highly sensitive to the thermal and stress factors than in the non-SPR condition. Second, to investigate the excited response under SPR in detail, the pump probe system with the straightforward probe light was prepared. Clearer response was obtained by this system compared with that measured by the system with focused probe light. By measuring at several incident angles near the SPR angle, it appeared that the reflectivity changes were caused by the broadening of the SPR curve and the shift in the SPR angle.

Next, an integrated theoretical model of the transient response under SPR by a sub-nanosecond pump probe system was constructed in order to understand the mechanism. Constructed theoretical model was composed of six steps: the preparation of the laser profile, temperature increase at the irradiated area of the pump light, generation of the thermoelastic stress, estimation of the permittivity change in the Ag metal film, estimation of the reflectivity change, and final convolution process. The theoretical estimations were compared with the experimental data to confirm the validity of the constructed theory. Consequently, the theoretical estimations were in good agreement with the experimental measurements. Therefore, the validity of the constructed theoretical model was successfully shown.

According to the constructed theory, the transient response due to the sub-nanosecond pulsed laser was caused by the changes in the permittivity of the metal film. The change in the real part shifted the SPR angle and that of the imaginary part broadened the SPR curve. The changes in the real and imaginary parts came from the changes in the plasma frequency and the damping constant of the metal film, respectively. In conclusion, it was assumed that the transient reflectivity change due to the pump light irradiation was caused by the shift in SPR angle, which was attributed to the thermal expansion due to the thermoelastic stress, and the broadening of the SPR curve, which was attributed to the change in the electron-phonon scattering rate due to the temperature increase.

Here, the changes in the real and imaginary parts of the permittivity of the metal film used can be determined by a variable angle spectroscopy of the sub-nanosecond pump probe near the SPR angle and the theoretical fitting. Moreover, the temperature increase and the thermal expansion can be estimated from the change of the imaginary part which is a function of temperature if the thermal expansion coefficient of the metal film is known in advance. Therefore, the sub-nanosecond pump probe spectroscopy has a possibility to be used as an evaluation method of the change of the optical property due to the temperature increase and the thickness deformation of the metal film. This spectroscopy technique also has a possibility to evaluate the elasticity of a metal film with known thermal expansion coefficient if a glass prism with known thermal properties is used. By this spectroscopy technique, the measurement of the elasticity and the change of optical property as the transient response in the sub-nanosecond region is expected, which is an important property for SPR ultrasonic sensors used in a high-resolution PAM systems.

APPENDIX

In recent years, surface plasmon resonance (SPR) sensors have attracted attention as ultrasonic sensors for photoacoustic microscopy (PAM) system. The application for ultrasonic detection was discovered by Schilling et al. in 1996 for the first time [A.1]. Moreover, they expected that the SPR sensor had the capability to show flat frequency response. In 2015, Wang et al. experimentally demonstrated that a simple Kretschmann-type SPR ultrasonic sensor with a coupling medium of water had a flat frequency response in a wide frequency range of 0.68–126 MHz [A.2]. They also demonstrated 3D imaging of a melanosome with high-resolution by all optical PAM system with a pulsed laser (pulse duration of 10 ps), utilizing the wideband characteristics of the SPR ultrasonic sensor.

SPR sensors enable detections of ultrasonic shock wave in non-resonance by measuring the changes in the reflectivity or the SPR angle. An SPR sensor also acts as a local sensing devise without cables because of optical devise. Therefore, SPR sensors have good potential to detect remotely ultrasound over a wide frequency range with high spatial resolution. Here, the performance of the simple Kretschmann-type SPR sensor was confirmed experimentally. Especially, the capability of detecting ultrasonic pulse wave with high frequency in the MHz range was demonstrated.

A.1 SPR SENSOR WITH COUPLING WATER

For the experimental demonstration, a simple Kretschmann-type SPR sensor was prepared. The sensor was composed of a Ag metal film (56 nm) on a BK7 glass prism. The Ag metal film was deposited by an electron beam deposition apparatus (EB1100, Canon Anelva Corp.). The detailed explanation of this sensor was described in Chapter 5.1. The pure water was used as a coupling medium to detect the ultrasonic wave. The SPR curve of this sensor is shown in Fig. A1. The data were measured by the system shown in Fig. A2. The CW laser (mpc3000, Laser Quantum, Manchester, UK) with a wavelength of 532 nm was used as an optical source. To obtain the reflectivity, the light intensities of the incident and reflected lights were measured outside the water by a wattmeter (S120B, THORLAB, New Jersey, US). The SPR angle was confirmed to be 73.3°. The theoretical estimation was also shown in Fig. A1. In this estimation, the refractive index of water was 1.334. The real and imaginary parts of the permittivity of the Ag metal film were

−11.16 and 0.57, respectively (described in Chapter 5.1). The estimated SPR angle was 73.1°. The difference between the experimental value and the estimated value were assumed to be due to the distortion of the measured SPR curve. The distortion appeared to be caused by the incident angle dependence of the water tank.

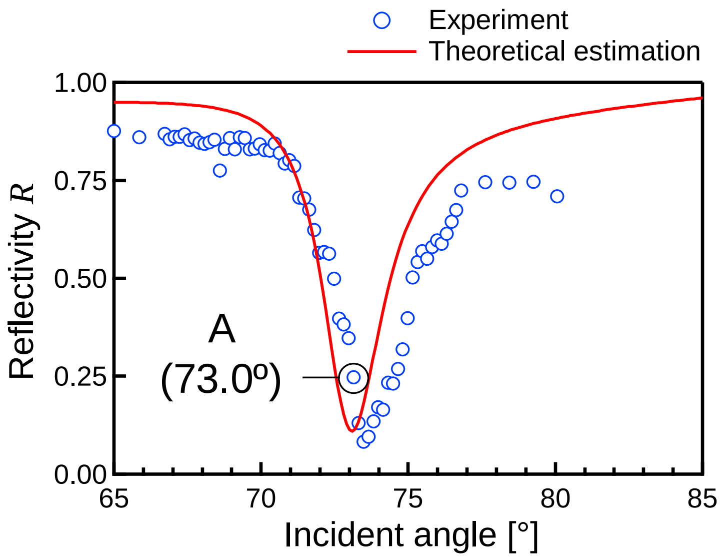

Fig. A1 Incident angle dependence of the reflectivity of the simple Krestchmann-type SPR sensor. The theoretical estimation is also drawn as a solid red line.

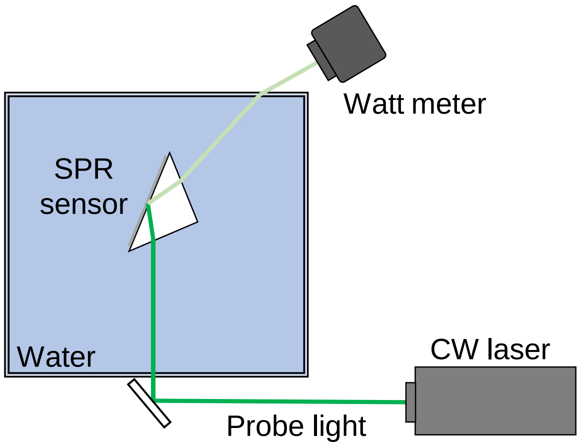

Fig. A2 Measurement system of the SPR curve. To measure the reflectivity, the intensities of the incident and reflected lights were measured outside the water.

A.2 ULTRASOUND DETECTION SYSTEM WITH SPR

To confirm the capability of the ultrasonic detection, simple measurement system was prepared. Figure A3 shows the measurement system. The simple Krestchmann-type SPR sensor was fixed in water because water was used as a coupling medium. CW laser with a wavelength of 532 nm (mpc3000, Laser Quantum, Manchester, UK) was used as an optical source. Laser light was separated to the CW probe light and the reference light by a half mirror (HM). The probe light irradiated to the SPR sensor at the incident angle of 73.0º, which is marked in Fig. A2. Optical reflectivity change of the SPR sensor due to the ultrasonic irradiation was detected by a differential detection system using a balanced detector (1607-AC-FS, Newport Corp., Irvine, California). To attain the differential detection, the reflected light by the SPR sensor and the reference light were inputted to the balanced detector after adjusting the light intensity of the reference light by a variable beam splitter (VBS). The signal voltage was measured by a lock-in amplifier.

To generate an ultrasonic pulse wave, one cycle of sinusoidal wave with the central frequency of 5.0 MHz was applied to a PZT piezoelectric transducer (IWC-B5K10I, Japan probe, Kanagawa, Japan). The signals were applied with a repetition frequency of 1.0 kHz. The repetition frequency was used as a reference signal of the lock-in amplifier. Here, the SPR sensor was set in the distance of 130 mm from the PZT piezoelectric transducer. However, the transducer was fixed external of the water tank to avoid the effect of the electromagnetic noise. The ultrasonic pulse waves were irradiated into the water tank via an acoustic matching layer.

In advance, the maximum pressure values of the irradiated ultrasonic wave were confirmed by a calibrated PVDF ultrasonic transducer.

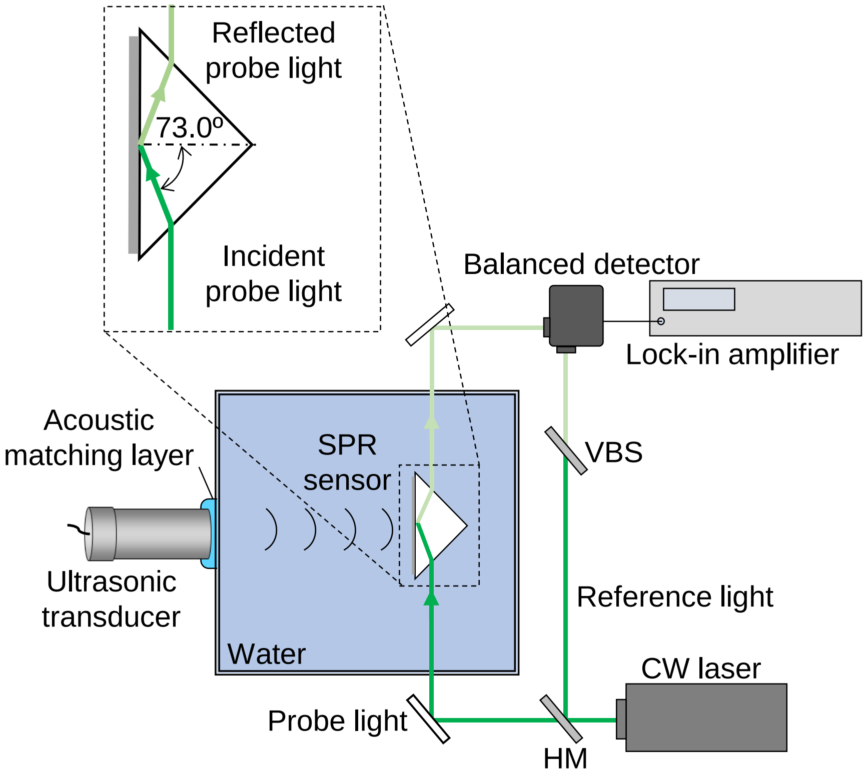

Fig. A3 Measurement system of ultrasonic wave with a SPR ultrasonic sensor. A CW laser with a wavelength of 532 nm was used as an optical source. Signal detection was attained by a differential detection system and a lock-in amplifier. Ultrasonic waves irradiated via acoustic matching layer from outside by an ultrasonic transducer.
HM: Half mirror. VBS: Variable beam splitter.

A.3 DEMONSTRATION OF ULTRASOUND DETECTION

First, the ultrasonic pulse waves were detected by the SPR sensor in the range of the peak values of the pressure between 670 Pa and 2800 Pa. Figure A4 shows the output voltages of the lock-in amplifier as a function of the peak value of pressure of the ultrasonic pulse wave [A.3]. As can be seen in Fig. A4, the measured output voltages had a linear characteristic against the peak values of the pressure. Here, the estimated reflectivity changes are also shown in Fig. A4. The changes of the refractive indices of the water, BK7 glass prism and Ag metal film by the applied pressure were considered in these estimations. The refractive indices of the water $n_w(p)$

[A.4, A.5] and the BK7 glass prism $n_{\mathrm{BK7}}(p)$ [A.6, A.7] as a function of applied pressure p were written below:

$$n_{\mathrm{w}}(p) = 1.334 + 1.35 \times 10^{-10}p \tag{A.1}$$

$$n_{\mathrm{BK7}}(p) = 1.519 + 7.29 \times 10^{-12}p. \tag{A.2}$$

In the change of refractive index of the Ag metal film, the influence of the change of plasma frequency was only considered. The estimated reflectivity changes of the SPR sensor by the applied pressure showed linear tendency. The measured output voltages also showed same tendency with that of theoretical estimations. Therefore, the reflectivity of simple Krestchmann-type SPR sensor appeared to be changed by the applied ultrasonic pulse wave. In accordance with the theoretical estimations, the reflectivity change seems to nearly depend on the change of refractive index of water. Same consideration has been reported by some previous reports [A.1, A.8, A.9].

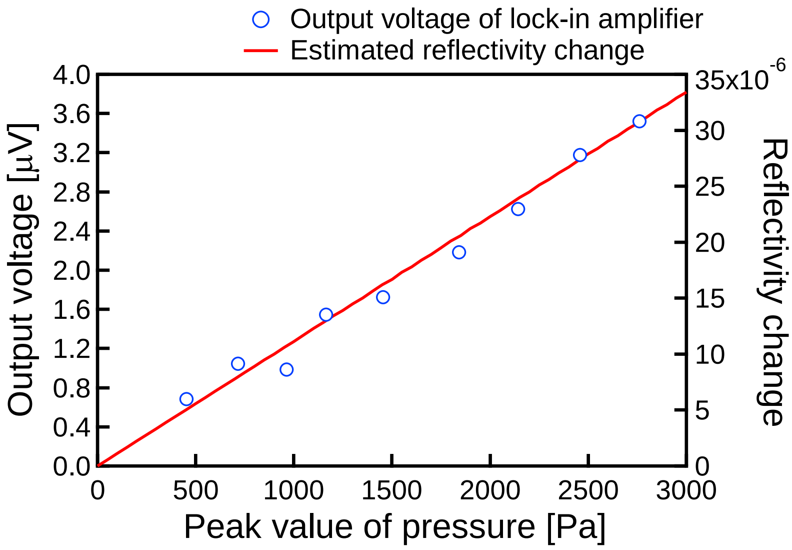

Fig. A4 Output voltages of the lock-in amplifier as a function of the peak value of the ultrasonic pulse wave, which indicates the signal intensities of the simple Kretschmann-type SPR acoustic sensor with a coupling water. The estimated reflectivity changes of the SPR sensor are also shown by a red solid line.

A.4 TECHNIQUES TO IMPROVE THE SENSITIVITY

To improve the sensitivity, several SPR ultrasonic detection techniques have been suggested in the previous reports. Here, there are two approaches to improve the sensitivity: the improvement of the optical detection system and the design of the SPR sensor.

First, several optical detection techniques are introduced. As an optical detector, a photodiode is generally used [A.1, A7, A.8, A.10]. However, the sensitivity is too low to detect the reflectivity change in the SPR ultrasonic sensor. Then, a differential detection technique with a balanced detector is effective to improve the sensitivity [A.4, A.11]. Our demonstration also adopted this detection technique. Next, the method to measure the output voltage of the optical detector is also important. An oscilloscope is widely used to measure the output voltage of the optical detector [A.1]. For better sensitivity, a technique with a lock-in amplifier is utilized [A.5]. This technique is also adopted in our system. However, the temporal waveform cannot be measured by this method. In recent years, the acquisition technique with a low noise amplifier and a digitized data acquisition card has been reported to obtain the temporal waveform with high S/N ratio [A.11].

Next, several improvement methods of the sensor structure are introduced. A simple Ktestchmann-type SPR sensor is mostly investigated as an ultrasonic SPR sensor [A.4, A.11]. The structure of this sensor was also used in our demonstration. In this sensor structure, the selections of the coupling medium, the glass prism and the metal film are important for designing. The sensor design with a plasmonic nanorod metamaterial has been suggested for attaining the better sensitivity [A.5]. This sensor has a structure such that Au metal nanorods on the metal film are surrounded in polymer. In this design, ultrasounds are detected as a reflectivity change which is caused by the change of the LSPR due to the vibration of the metamaterial nanorods. Therefore, the designs of the metal nanorods, the metal films and the surrounding polymer material are important for this sensor structure. In addition, the design with an additional receiving layer has been suggested [A.10]. This sensor has a Kretschmann-type SPR structure with a gap space and an additional receiving layer. In this design, ultrasounds are detected as a reflectivity change which is caused by the interaction between the SPW and the receiving layer vibrated by the ultrasounds. Therefore, the designs of the receiving layer, the gap space and the base as a Krestchmann structure are important for deciding the function of this sensor.

Several new sensor structures and detection technologies have been reported since 2010, and SPR sensing technology has been developing. For the development of PAM technology, SPR ultrasonic detection techniques are expected to progress.

REFERENCES

[A.1] A. Schilling, O. Yavas, J. Bischof, J. Boneberg, and P. Leiderer, “Absolute pressure measurements on a nanosecond time scale using surface plasmons,” Appl. Phys. Lett., vol. 69, no. 27, pp. 4159–4161, Oct. 1996.

[A.2] T. Wang, R. Cao, B. Ning, A. J. Dixon, J. A. Hossack, A. L. Klibanov, Q. Zhou, A. Wang, and S. Hu, "All-optical photoacoustic microscopy based on plasmonic detection of broadband ultrasound" Appl. Phys. Lett., vol. 107, no. 153702, Oct. 2015.

[A.3] S. Ueno, H. Ichihashi, T. Fukunaga, and M. Matsukawa, "Surface plasmon resonance sensor for ultrasound in the MHz range", Abstract of USE 2019.

[A.4] X. Zhu, Z. Huang, G. Wang, W. Li, D. Zou, and C. Li, "Ultrasonic detection based on polarization-dependent optical reflection", Opt. Lett., vol. 42, no. 3, pp. 439–441, Feb. 2017.

[A.5] V. V. Yakovlev, W. Dickson, A. Murphy, J. Mcphillips, R. J. Pollard, V. A. Podolskiy, and A. V. Zayats, "Ultrasensitive non-resonant detection of ultrasound with plasmonic metamaterials", Adv. Mater., vol. 25, pp. 2351–2356, Mar. 2013.

[A.6] M. Terada, S. Hatano, Y. Mori, and K. Nagatama, "Optical method of measuring nanosecond pressure pulse in water", Appl. Surf. Sci., vol. 197-198, pp. 285–288, 2002.

[A.7] R. M. Waxler and C. E. Weir, "Effect of hydrostatic pressure on the refractive indices of some solids", J. Res. NBS, vol. 69A, no. 4, Mar. 1965.

[A.8] J. Boneberg, S. Briaudeau, Z. Demirplak, V. Dobler, and P. Leiderer, “Two-dimensional pressure measurements with nanosecond time resolution”, Appl. Phys. A, vol. 69, pp. S557–S560, Sep. 1999.

[A.9] R. Nuster, G. Paltauf, and P. Burgholzer, "Comparison of surface plasmon resonance devices for acoustic wave detection in liquid", Opt. Express, vol. 15, no. 10, Apr. 2007.

[A.10] A. A. Kolomenskii, E. Surovic, and H. A. Schuessler, "Optical detection of acoustic waves with surface plasmons", Appl. Opt., vol. 57, no. 20, pp. 5604–5613, June 2018.

[A.11] W. Song, L. Peng, G. Guo, F. Yang, Y. Zhu, C. Zhang, C. Min, H. Fang, S. Zhu, and X. Yuan, "Isometrically, resolved photoacoustic microscopy based on broadband surface plasmon resonance ultrasound sensing", Appl. Mater. Interfaces 2019, vol. 11, pp. 27378–27385, 2019.

PREVIOUS PUBLICATIONS AND RESEARCHES

JOURNALS

[1] H. Ichihashi, T. Yanagitani, S. Takayanagi, M. Kawabe, and M. Matsukawa, “Gigahertz acoustic wave velocity measurement in GaN single crystals considering acousto-electric effect,” IEEE Trans. Ultrason. Ferroelectr. Freq. Control, vol. 61, no. 8, pp. 1307–1313, Aug. 2014. (Invited)

[2] H. Ichihashi, T. Yanagitani, M. Suzuki, S. Takayanagi, and M. Matsukawa, “Effect of Sc concentration on shear wave velocities in ScAlN films measured by micro-Brillouin scattering technique”, Proc. IEEE Ultrason. Symp. 2014, pp. 2521-2524, Oct. 2014.

[3] M. Kawabe, T. Yanagitani, H. Ichihashi, S. Takayanagi, M. Suzuki, and M. Matsukawa, “Fast wave velocity measurement by Brillouin scattering using induced phonon from ScAlN piezoelectric thin film”, Proc. IEEE Ultrason. Symp. 2015, pp. 21–24, Oct. 2015.

[4] H. Ichihashi, T. Yanagitani, M. Suzuki, S. Takayanagi, M. Kawabe, S. Tomita, and M. Matsukawa, “Acoustic -wave velocities and refractive indices in an m-plane GaN single-crystal plate and c-axis oriented ScAlN films measured by Brillouin scattering techniques”, Ultrason. Ferroelectr. Freq. Control, vol. 63, no. 5, pp. 117-125, May 2016.

[5] S. Tomita, T. Yanagitani, S. Takayanagi, H. Ichihashi, Y. Shibagaki, H. Hayashi, and M. Matsukawa, "Evaluation of the acoustoelectric effect in the thickness direction of c -plane ZnO single crystals by Brillouin scattering", J. Appl. Phys., vol. 121, no. 23, June 2017.

[6] H. Ichihashi, H. Hayashi, S. Takayanagi, and M. Matsukawa, “Sub-nanosecond pump probe measurement in a Au/Cr bimetal film”, Proceedings of the 7th Asia-Pacific Optical Sensors Conference, May 2018.

[7] H. Ichihashi, H. Hayashi, S. Takayanagi, M. Matsukawa, and Y. Watanabe, “Highly sensitive detection of photo-thermal transient stress by a sub-nanosecond pump probe with surface plasmon resonance”, AIP Advances, vol. 8, no. 105102, Sep. 2018.

[8] M. Kawabe, S. Takayanagi, H. Ichihashi, M. Suzuki, T. Yanagitani, and M. Matsukawa, "Rapid wave velocity measurement by Brillouin scattering using coherent phonons induced by ScAlN piezoelectric thin-film transducer", Ultrason. Ferroelectr. Freq. Control, vol. 65, no. 10, pp. 1882–1887, Oct. 2018.

INTERNATIONAL CONFERENCES

[1] H. Ichihashi, T. Sugimoto, T. Yanagitani, S. Takayanagi, and M. Matsukawa, “Shear and longitudinal GHz elastic properties in GaN single crystals determined by Brillouin scattering method”, 2013 Joint UFFC, EFTF and PFM symposium, July 2013.

[2] H. Ichihashi, T. Yanagitani, S. Takayanagi1, and M. Matsukawa, “Effect of Sc concentration on shear wave velocities in ScAlN films measured by micro-Brillouin scattering technique”, 2014 IEEE International Ultrasonics Symposium, Sep. 2014.

[3] S. Tomita, T. Yanagitani, M. Suzuki, H. Ichihashi, S. Takayanagi, and M. Matsukawa, “Measurement of acoustic wave velocity and refractive index in thickness direction of c-axis oriented ScAlN films by Brillouin scattering”, IEEE International Ultrasonics Symposium 2015, Oct. 2015.

[4] T. Yanagitani, H. Ichihashi, M. Suzuki, S. Takayanagi, and M. Matsukawa, Elastic constant cijE tensors of (0001) ScxAl1-xN films (x=0-0.63), IEEE International Ultrasonics Symposium 2015, Oct. 2015.

[5] M. Kawabe, T. Yanagitani, H. Ichihashi, S. Takayanagi, M. Suzuk, and M. Matsukawa, “Fast wave velocity measurement by Brillouin scattering using induced phonon from ScAlN piezoelectric thin film”, IEEE International Ultrasonics Symposium 2015, Oct. 2015.

[6] S. Tomita, T. Yanagitani, S. Takayanag, H. Ichihashi, and M. Matsukawa, “Brillouin scattering study on piezoelectric stiffening effect in the thickness direction of c-plane ZnO single crystal”, 2016 IEEE International Ultrasonics Symposium, Sep. 2016.

[7] H. Ichihashi, H. Hayashi, S. Takayanagi, and M. Matsukawa, “Sub-nanosecond pump probe measurement in a Au/Cr bimetal film”, The 7th Asia-Pacific Optical Sensors Conference, May 2018.

[8] H. Yasui, M. Kawase, H. Ichihashi, Y. Kuzuhara, M. Ikegawa, and M. Matsukawa, “Evaluation of longitudinal wave velocity in bone of diabetic rats by a micro-Brillouin scattering technique”, 40th International Conference of the IEEE Engineering in Medicine and Biology Society, July 2018.

[9] H. Ichihashi, H. Hayashi, S. Takayanagi, and M. Matsukawa, “High sensitivity sub-nanosecond pump probe measurement with surface plasmon resonance”, 2018 IEEE International Ultrasonics Symposium, Oct. 2018.

[10] H. Hayashi, H. Ichihashi, S. Ueno, M.Matsukawa, “Photo-thermal transient stress observed by sub-nanosecond pump-probe technique with the surface plasmon resonance”, 176th Meeting of the Acoustical Society of America, Nov. 2018.

[11] S. Ueno, H. Ichihashi, T. Nakamura, M. Matsukawa, “Simple optical ultrasound detector with surface plasmon resonance”, IEEE International Ultrasonics Symposium, Oct. 2019.

DOMESTIC CONFERENCES

[1] 市橋隼人, 柳谷隆彦, 高柳真司, 川部昌彦, 松川真美,「Brillouin散乱法を用いたGaN単結晶の音速分散測定」, 第34回超音波エレクトロニクスの基礎と応用に関するシンポジウム（USE2013）, 2013年11月

[2] 市橋隼人, 柳谷隆彦, 高柳真司, 松川真美,「音響電気効果を考慮したGaN単結晶のGHz域音速の温度・周波数分散測定」, 圧電材料・デバイスシンポジウム2014, 2014年1月

[3] 川部昌彦, 市橋隼人, 松川真美,「GHz域のコヒーレントフォノン励起による高速Brillouin光散乱測定」, 電子情報通信学会 フォトニックネットワーク, 2014年1月

[4] 市橋隼人, 柳谷隆彦, 鈴木雅視, 高柳真司, 川部昌彦, 松川真美,「Brillouin光散乱法によるScAlN薄膜の弾性定数c11とc66のSc濃度依存性」, 第35回超音波エレクトロニクスの基礎と応用に関するシンポジウム（USE2014）, 2014年12月

[5] 川部昌彦, 柳谷隆彦, 市橋隼人, 高柳真司, 鈴木雅視, 松川真美, 「ScAlN 圧電薄膜による高周波励起フォノンを用いた高速 Brillouin 散乱測定」, 第 35 回超音波エレクトロニクスの基礎と応用に関するシンポジウム（USE2014）, 2014 年 12 月

[6] 市橋隼人, 柳谷隆彦, 高柳真司, 川部昌彦, 松川真美, 「180°, 90R 散乱配置を用いた Brillouin 散乱計測による GaN の弾性定数測定」, 第 62 回応用物理学会春季学術講演会, 2015 年 3 月

[7] 柳谷隆彦, 市橋隼人, 鈴木雅視, 高柳真司, 松川真美, 「ScAlN 薄膜における弾性定数テンソルの Sc 濃度依存性」, 圧電材料・デバイスシンポジウム 2015 , 2015 年 2 月

[8] 柳谷隆彦, 市橋隼人, 鈴木雅視, 高柳真司, 松川真美, 「共振法および Brillouin 散乱法で測定した ScAlN 薄膜の弾性定数テンソルの Sc 濃度依存性」, 電子情報通信学会 超音波研究会 , 2015 年 9 月

[9] 川部昌彦, 柳谷隆彦, 市橋隼人, 高柳真司, 鈴木雅視, 松川真美, 「Brillouin 散乱法を用いた圧電性 ScAlN 薄膜による励起フォノンの測定」, 第 76 回応用物理学会秋季学術講演会, 2015 年 9 月

[10] 市橋隼人, 林弘通, 柴垣慶明, 松川真美, 「Brillouin 光散乱による弾性波音速計測の測定不確かさ」, 電子情報通信学会 超音波研究会, 2018 年 1 月

[11] 林弘通, 市橋隼人, 高柳真司, 松川真美, 「サブナノ秒ポンプ・プローブ分光計測手法の開発」, 第 61 回光波センシング技術研究会講演会, 2018 年 6 月

[12] 林弘通, 市橋隼人, 上野翔矢, 松川真美, 「SPR を用いたサブナノ秒ポンプ・プローブ法による熱弾性効果の観測」, 日本音響学会 2018 年秋季研究発表会, 2018 年 9 月

[13] 林弘通, 市橋隼人, 上野翔矢, 松川真美, 「サブナノ秒ポンプ・プローブ法による SPR センサの性能評価」, 第 39 回超音波エレクトロニクスの基礎と応用に関するシンポジウム（USE2018）, 2018 年 10 月

[14] 林弘通, 市橋隼人, 上野翔矢, 安井寛和, 松川真美, 「サブナノ秒ポンプ・プローブ法を用いた表面プラズモン共鳴センサの評価」, 電子情報通信学会 超音波研究会, 2019 年 1 月

[15] 林弘通, 市橋隼人, 上野翔矢, 牧野大輝, 松川真美,「光音響顕微測定に向けた表面プラズモン共鳴センサの評価」, 圧電材料・デバイスシンポジウム2019, 2019年1月